Design and characterization of multiscale hybrid scaffolds for endochondral ossification

vorgelegt von
M. Sc.
Martina Tortorici

an der Fakultät V – Verkehrs- und Maschinensysteme der
Technischen Universität Berlin
zur Erlangung des akademischen Grades

Doktor der Ingenieurwissenschaften
– Dr. -Ing. –

genehmigte Dissertation

Promotionsausschuss:

Vorsitzender: Prof. Dr.-Ing. Andreas Bardenhagen
Gutachter: Univ.-Prof. Dr.-Ing. Georg N. Duda
Gutachter: Univ.-Prof. Dr.-Ing. habil. Manfred W. Zehn

Tag der wissenschaftlichen Aussprache: 30. April 2021

Berlin 2021

Diese Arbeit wurde von März 2017 bis Dezember 2020 in den „Cellular Biomechanics and Biomaterials“ und „Computational Mechanobiology“ Gruppen des Julius Wolff Instituts unter der Betreuung von Prof. Dr. Georg N. Duda angefertigt.

Die Arbeiten entstanden innerhalb des Netzwerkes der Berlin-Brandenburg School for Regenerative Therapies (BSRT) bzw. des Berlin-Brandenburg Center for Regenerative Therapies (BCRT) und in aktiver Kollaboration mit dem Fraunhofer Institut für Laser Technologie (ILT) und Matricel GmbH. Das Bundesministerium für Bildung und Forschung (BMBF) hat das Projekt durch die Förderung 13XP5048D finanziert.

1. Gutachter: Univ.-Prof. Dr.-Ing. Georg N. Duda

2. Gutachter: Univ.-Prof. Dr.-Ing. habil. Manfred W. Zehn

To all the wonderful people that supported me in this endeavour

Abstract

Critical size defects in bone and osteochondral defects in articular cartilage do not heal without clinical intervention. Current clinical treatments of both defect types are associated with strong limitations, which could be addressed by the development of tissue engineering (TE) treatment strategies.

Collagen scaffolds with a highly aligned architecture have been previously shown to induce bone formation by endochondral ossification in large bone defects *in vivo*. The establishment of the endochondral ossification process has been proven to depend on the aligned architecture of the collagen scaffolds, without the need for the inclusion of additional biochemical factors. However, the direct clinical application of these collagen scaffolds is hindered by their extremely low stiffness (low kPa range), which determines the easy alteration of the aligned architecture by means of tissue forces and extracellular matrix deposition within the scaffold pores.

Here, the limitations of the collagen scaffolds with highly aligned architecture are addressed by incorporation of a stiffer synthetic support structure, generating multiscale hybrid scaffolds. The aim of the support structure is not limited to the improvement of the mechanical stiffness of the scaffold system at tissue level, but it extends also to the steering of the tissue regeneration process by means of different scaffold-dependent mechanical cues, which could be achieved by different types of support structures, e.g. a stiff and a compliant one. In fact, the development of bone through endochondral ossification happens by first establishing a cartilaginous template, which is then mineralized. Moreover, the formation of bone and cartilage has been associated to mechanical stimuli of lower and higher magnitude, respectively. Therefore, mechanical cues determined by the stiffness at tissue level of the hybrid scaffolds are intended to be used to guide tissue formation towards either bone or cartilage. The successful establishment of this approach would enable the use of controlled mechanics for applications beyond bone defect healing, e.g. in the treatment of osteochondral defects.

In this thesis, a stiff and a compliant support structure to be included in the hybrid scaffolds were designed. Thereafter, the production of the support structures by selective laser sintering from poly(ε-caprolactone) was optimized in terms of material choice and resulting support structure properties. Moreover, stiff and compliant support structure architectures with significant differences in stiffness and fatigue resistance in *in vivo*-like conditions were designed. Subsequently, stiff and compliant hybrid scaffolds were produced and characterized in terms of morphology of the collagen walls, mechanical properties, and *in vitro* cell-material interactions. Concurrently, the ideal mechanical and architectural properties of scaffolds for osteochondral defect regeneration were here investigated by means of a computational model.

Zusammenfassung

Die Heilung von großen Knochendefekten, sowie osteochondralen Defekten ist gegenwärtig stets auf eine klinische Intervention angewiesen. Allerdings weisen derzeitige Behandlungsmethoden von beiden Defekten erhebliche Limitationen auf. Die Entwicklung von neue Methoden basierend auf „Tissue Engineering“ (TE) könnten dazu beitragen, diese Limitationen auszugleichen.

Für kollagen-basierte Biomaterialien mit einer gerichteten Porenstruktur wurde kürzlich gezeigt, dass sie eine endochondrale Ossifikation anregen können. Die Implantation dieses Biomaterials in einen großen Knochendefekt im Femur der Ratte führte zu einer Knochenbildung, die rein auf die Architektur des Materials zurückzuführen ist und ohne die zusätzliche Behandlung mit biochemischen Faktoren auskommt. Der Nachteil dieser Biomaterialien ist allerdings ihre extrem geringe mechanische Stabilität resultierend aus einer niedrigen Steifigkeit. Diese Eigenschaft macht die direkte Anwendung dieser Scaffolds in großen Knochendefekten zunächst problematisch, da die gerichtete Porenstruktur durch die im Gewebe vorhandenen mechanischen Kräfte verloren gehen kann.

Ziel dieser Arbeit war es, diese Limitation des Kollagenscaffolds durch eine zusätzliche Inkorporation einer synthetischen Stützstruktur mit höherer Steifigkeit zu überwinden und dadurch einen Hybridscaffold mit multiskalaren Eigenschaften zu entwickeln. Die Stützstruktur sollte hierbei nicht nur allein die mechanische Stabilität des Scaffolds verbessern, sondern auch je nach mechanischem Stimuli entweder den Heilungsprozess nach Knochen- oder Knorpelbildung durch endochondrale Ossifikation abstoppen. Dies hat den Hintergrund, dass die Gewebeeigenschaften in Entwicklung von Knochen und Knorpelgewebe *in vivo* mit unterschiedlichen mechanischen Eigenschaften assoziiert sind. In diesem Projekt wurden die Zielgewebe-spezifischen mechanischen Stimuli durch unterschiedliche Designs, und damit auch unterschiedlichen Steifigkeiten (z.B. steif und weich), der Stützstrukturen erreicht. Wäre diese Methode erfolgreich, könnten die Hybdriscaffolds als Behandlung von Knochendefekten kritischer Größe, sowie osteochondraler Defekte benutzt werden.

In dieser Arbeit wurden je eine weiche und eine steife Stützstruktur für einen Hybridscaffold, die verschiedene Steifigkeit hatten und die *in vivo* Lasten tragen könnten, entwickelt. Danach waren steife und weiche Hybdridscaffolds hergestellt und ihren Eigenschaften (Kollagen Struktur, Steifigkeit, *in vitro* Zell-Materialen Interaktionen) gemessen worden. Außerdem wurde ein Computermodel etabliert, um die idealen mechanischen und strukturellen Eigenschaften eines Scaffolds für osteochondrale Defekte zu erforschen.

Table of contents

List of figures

List of tables

Abbreviations and variables

#

2D: two-dimensional
3D: three-dimensional
β-TCP: β-tricalcium phosphate
γ: octahedral shear strain
ΔL: displacement
ε: strain
µCT: micro-computed tomography
ν: Poisson's ratio
σ: stress

A

A: cross-section
ACI: autologous chondrocyte implantation
A_M: molten cross-section

B

BC: laser beam compensation
BD: laser beam diameter
BSA: bovine serum albumin

C

CAD: computer-aided design

D

d: migration distance
DAPI: 4',6-Diamidino-2-Phenylindole
DC: diffusion coefficent
D_C: computational diameter
DI: dispersity index
D_M: molten diameter
D_S: strut diameter
DMEM: Dulbecco's Modified Eagle medium

E

E: elastic modulus
E_C: computational elastic modulus
ECM: extra-cellular matrix
EtOx: ethylene oxide

F

FBS: fetal bovine serum
FDA: Food and Drug Administration
FE: finite element

G

G: shear modulus

K

k: stiffness
k_C: computational stiffness

L

L: height

M

MACI: matrix-assisted chondrocyte implantation
$\bar{M}_n$: number average molecular weight
MSCs: mesenchymal stromal cells
$\bar{M}_w$: weight average molecular weight

N

NDS: normal donkey serum
NEA: non-essential amminoacids

P

P: porosity
PA: polyamide
PCL: poly(ε-caprolactone)
PFA: paraformaldehyde
P_L: laser power
PLGA: polylactide-co-glycolide
PMMA: poly(methyl-metacrilate)
P/S: penicillin/streptomycin

R

RF: reaction force

S

S: mechanics-dependent differentiation stimulus
SEC: size-exclusion chromatography
SEM: scanning electron microscopy
SH: second harmonic
SLS: selective laser sintering

T

TBS: tris-buffered saline
TE: tissue engineering

V

V: volume
v: fluid velocity
V_S: solid volume

1 Introduction

1.1 Bone development

Bone is a mineralized connective tissue belonging to the musculoskeletal system [1].The purposes of bone in the body include locomotion, support and protection of soft tissues, reservoir of calcium and phosphate, and endocrine functions [1,2].

Mature bone tissue consists of an extra-cellular matrix (ECM) with both organic and inorganic phases and of a cellular component, which includes four cell phenotypes [1]: osteoblasts, bone lining cells, osteocytes, and osteoclasts. Osteoblasts, bone lining cells, and osteocytes derive from mesenchymal stromal cells (MSCs) and are involved in the formation of new bone tissue and in tissue homeostasis, while osteoclasts derive from mononuclear cells of the hematopoietic stem cell lineage and their function is to resorb existing bone tissue [1].

During development, bone is formed through two distinct processes [3]: intramembranous ossification and endochondral ossification. Intramembranous ossification consists in the direct differentiation of MSCs into osteoblasts and is the process by which flat bones, e.g. skull bones, form [3]. Long bones, e.g. the femur, form by endochondral ossification (Figure 1A), during which the deposition of new bone follows a previously established cartilaginous template [3]. Specifically, MSCs differentiate into chondrocytes, the characteristic cell phenotype of cartilage [4]. Chondrocytes produce cartilaginous ECM, forming the blueprint of the bone. Subsequently, chondrocytes in the tissue core increase in volume, becoming hypertrophic chondrocytes and promoting vascularization and mineralization. The previously deposited cartilaginous ECM act as a scaffold for osteoblasts and osteoclasts invasion, which eventually results in the formation of bone (Figure 1B).

Interestingly, both processes of bone formation have been observed also during bone healing, depending on the type of fracture [3]. Fractures with rigid fixation, i.e. low interfragmentary movements between bone extremities and small gap size, heal by intramembranous ossification, while fractures subjected to more movements between bone extremities heal by first forming a soft callus that is subsequently mineralized, similarly to the endochondral ossification process [5].

Normally, bone is continuously remodeled by an interplay of osteoclasts, osteoblasts, and osteocytes, a process that is fundamental for facture healing, tissue adaptation to mechanical loads, and calcium homeostasis [1]. Of particular interest is the response of bone to mechanical stimuli. In fact, osteocytes act as mechanosensors, directing bone remodeling in such a way as to adapt to mechanical loading [2]. During fracture healing, bone formation has been correlated to areas of low strain (< 9%) both in *in vivo* [6] and *ex vivo* [7] evaluations. On the contrary, regions subjected to higher strains of 15-25%

[7] and > 30% [6] resulted in a higher probability of cartilage and fibrocartilage formation, respectively. *In vitro* evidence indicates an influence of mechanical cues also on MSCs differentiation [8]. Specifically, MSCs subjected to a 10% compressive strain expressed osteogenic genes, while a higher compressive strain of 15% induced the expression of both osteogenic and chondrogenic genes [9]. The experimental observations linking mechanical stimuli to bone, cartilage, and fibrous tissue formation are supported also by computational models, in which tissue formation in bone healing is successfully described by mechanobiological rules [10,11]. For example, strain values and a hydrostatic pressure lower than 5% and 0.15 MPa, respectively, have been suggested to result in bone formation by intramembranous ossification, while strains of 5–15% and a hydrostatic pressure higher than 0.15 MPa were associated to bone formation by endochondral ossification [11].

Overall, the current body of evidence indicates mechanics as a key player in bone formation during healing, with the power of determining not only the modality of bone tissue deposition, i.e. by intramembranous ossification or by endochondral ossification, but also whether the healing itself will be successful or not [12]. Moreover, mature cartilage and bone form in areas of different strain, but these two tissues are closely interconnected in the developmental phase of bone tissue.

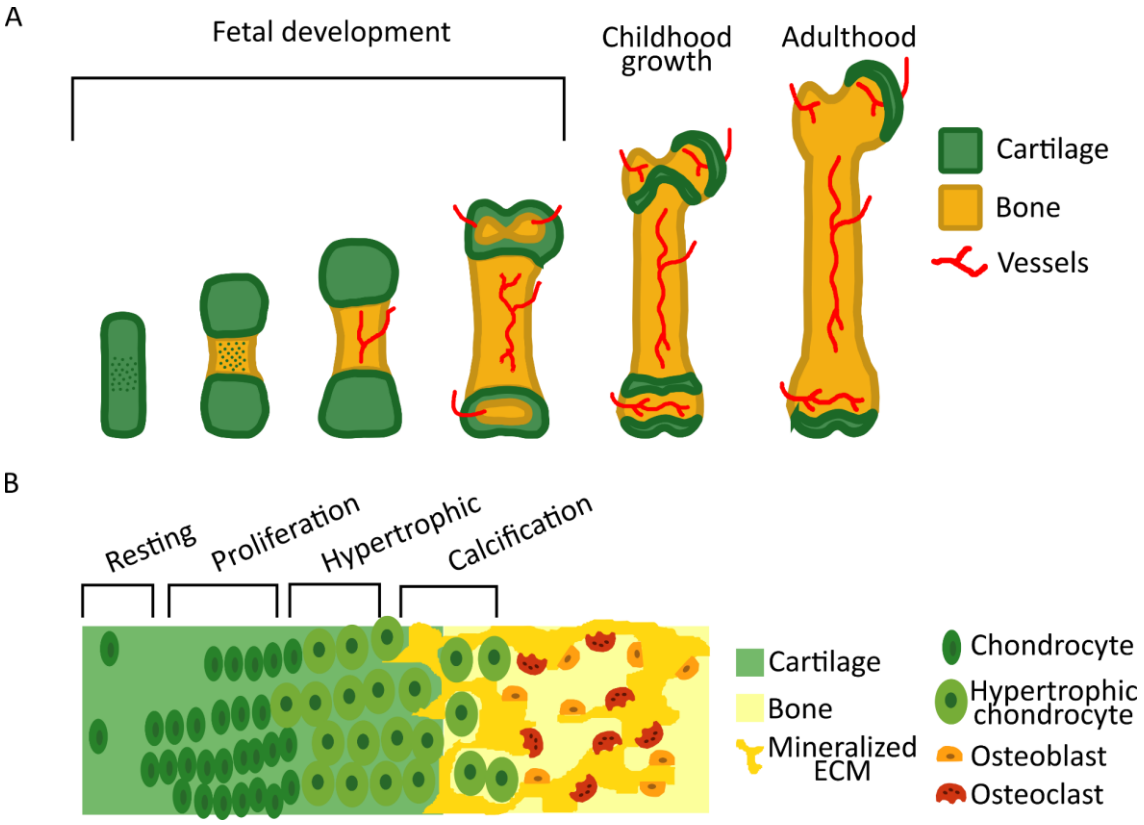

Figure 1: Schematic representation of the spatial-temporal aspects of the endochondral ossification process. A) Progression of endochondral ossification at tissue level [13]. The area in which the endochondral ossification process takes place is known as growth plate; B) progression of endochondral ossification at cellular level in the growth plate. The different zones of the process [13,14] are marked in the image.

1.2 Clinical challenges of bone and cartilage defect healing

Bone has a natural healing ability [3]. In fact, a fracture in the tissue can be spontaneously repaired without the formation of a disorganized scar, contrary to other biological tissues [5]. However, large bone defects may be unable to heal without clinical intervention and are thus defined as critical size bone defects [15].

Critical size bone defects might result from open fractures with bone loss, high-energy trauma, blast injuries, infections and resections of bone tumors [16]. Multiple factors influence whether a bone defect is of critical size, e.g. the size of the affected bone, the relative size of the defect, the presence of circumferential bone loss, the anatomical location, the soft tissue environment, and the age and comorbidities of the patient, making precise diagnosis methods still controversial [16].

The current gold standard treatment for critical size bone defects is autogenous bone grafting, which consists on the harvesting of a graft of the patient bone from a donor site and its implantation in the critical size defect [17]. Autogenous bone grafting has the advantages of being osteoinductive, osteoconductive, and osteogenetic [17], meaning that not only it allows bone cells to adhere, proliferate, and produce ECM on its surface and pores, but it also stimulates the formation of new bone by progenitor cell recruitment and biomolecular signaling [18]. However, autogenous bone grafting has also severe drawbacks, such as the limited available volume of grafting material, the risk of harvest-site complications, and the high rate of postoperative pain at the donor site [17].

Contrary to bone, cartilage has no natural regenerative ability [19]. Focal lesions of the cartilaginous tissue, called chondral defects [20], may result from trauma or illnesses and cause pain and impairment of joint functions [19]. If the lesion extends to the underlying subchondral bone, it is defined as osteochondral defect [20]. The natural repair response to chondral and osteochondral defects is the formation of fibrous tissue or fibrocartilage [4], whose inferior mechanical properties compared to cartilage do not allow a full re-establishment of the joint functions [21]. Moreover, once a lesion forms, a vicious feedback circle establishes, leading to the degeneration of the cartilage surrounding the defect [4] and eventually to a general state of disease of the whole joint, known as osteoarthritis [19]. Therefore, a timely and effective treatment of chondral and osteochondral defects is of particular importance.

Current treatments of osteochondral defects comprise a number of surgical options [20]. Some procedures, such as microfracture, which consists on the generation of small fractures in the bone underlying the defect, aim at exposing the damaged cartilage to the bone marrow to stimulate a spontaneous repair response [19]. A limitation of these approaches is that the repair tissue is very variable and of a fibrous nature [19]. Another strategy, known as mosaicplasty, consists on the implantation of autologous or allogenic osteochondral grafts at the injury site [20]. When autologous grafts are employed,

defects are generated at the donor site, triggering cartilage degeneration in another area of the joint [19]; on the other hand, the use of allogenic grafts is associated with the risks of disease transmission, immune reaction, and a slower remodeling [20]. Autologous chondrocyte implantation (ACI) and its variant, the matrix-assisted chondrocyte implantation (MACI), require the collection of a biopsy of cartilage tissue from the patient, from which autologous chondrocytes are isolated, expanded, and implanted in the osteochondral defect [20]. The disadvantages of ACI and MACI include the need for two surgeries, the long recovery times, and the generation of a lesion at the biopsy site [19,20]. Despite the variety of currently available treatment options, many of them are associated with significant drawbacks and the restoration of healthy articular surfaces remains a challenge [19,20].

Therefore, there is a clinical need for innovative and improved treatment strategies of both osteochondral and critical size bone defects: tissue engineering (TE) may answer this clinical need.

1.3 Biomaterial-based tissue engineering approaches

TE is a discipline that applies knowledge from different fields, such as engineering, medicine, and life science, to develop strategies for the restoration, preservation or improvement of body tissue functions [22]. This goal is pursued by a number of different approaches, which can be divided into two main categories [23]: *in vitro* and *in situ* strategies. *In vitro* TE uses biomaterials, cells, and chemical factors to produce functional tissue constructs prior to implantation in the body [23]. On the contrary, *in situ* TE aims at inducing healing directly at the implantation site by employing biomaterial- and/or biochemical-based cues [23]. Compared to *in vitro* TE, *in situ* TE is advantageous because it does not need to recapitulate the complex, and often not yet fully understood, microenvironment necessary to tissue development [24]. Furthermore, *in situ* TE approaches generally undergo an easier clinical translation from the regulatory point of view due to their comparatively lower complexity [24].

Although purely cell-based TE strategies are possible [25,26], in many cases biomaterials play a pivotal role in TE, especially in *in situ* approaches. Biomaterials can be used as temporary or permanent substitutes of a piece of tissue or organ, as delivery devices for cells or drugs, or as scaffolds that support and/or actively induce a specific tissue response [27]. In fact, biomaterials have been shown to influence cell and tissue behavior both *in vitro* and *in vivo* by means of their chemical, morphological, and mechanical properties [25]. Consequently, biomaterial-based *in situ* TE strategies have been suggested, amongst others [26,28,29], in the fields of bone TE [30] and cartilage TE [31].

Several of the currently investigated biomaterial-based *in situ* TE strategies exploit the incorporation of biochemical stimuli into cell-free scaffolds to induce and support the invasion of autogenous cells, i.e. cells of the host body, within the tissue lesion after

scaffold implantation [30,32]. However, there are also cases in which tissue regeneration is meant to be achieved purely by scaffold-derived cues, with the additional inclusion of neither cells nor biochemical factors [29,30]. An example can be found in collagen scaffolds with aligned architecture for the regeneration of critical size bone defects [33]. When implanted in large bone defect models in rat, the aligned architecture of these collagen scaffolds induced bone formation by endochondral ossification [33], representing a promising *in situ* developmental TE strategy for the treatment of critical size bone defects. Developmental TE is a branch of TE whose goal is to re-establish characteristic biological processes of the developmental stage that eventually lead to the production of mature tissue, rather than aiming at the immediate formation of already mature tissue as in classic TE [34]. By opting for a developmental bone TE approach for the healing of critical size bone defects, some of the problems associated with the formation of large pieces of mature bone, e.g. the need for a functional vascular system, are avoided [3]. Despite the encouraging *in vivo* defect healing achieved with the highly aligned collagen scaffolds, their direct clinical translation is hindered by their extremely low stiffness (elastic modulus < 10 kPa [33]). Such a low stiffness is detrimental for long term implant stability, as collagen scaffolds can be easily deformed by tissue forces and/or by ECM deposition within their pores [35]. As the aligned architecture of the collagen scaffolds triggers and guides endochondral ossification [33], a deformation-dependent loss of alignment might cause an early interruption of the biological process, thereby resulting in impaired healing of the critical size bone defect. Therefore, the need arises for a mechanical stabilization of the aligned collagen scaffolds that would not have detrimental effects on the favorable cell-scaffold interactions that were observed *in vivo* with its low stiffness.

A possible way to preserve the biologically favorable low stiffness at the cell level, while increasing scaffold stability by means of a higher stiffness at the tissue level, is the development of a multiscale hybrid scaffold by incorporation of a stiffer synthetic support structure within the aligned collagen scaffolds. In fact, hybrid scaffolds have already been suggested in literature as strategies to include in the same device the advantages of both natural and synthetic materials, i.e. the excellent biocompatibility and bioactivity of the former and the higher mechanical stability and versatility of the latter [24,36]. In bone TE, numerous hybrid scaffolds with multiscale properties have been developed by combining collagen with a stiffer material [37]. For example, the elastic modulus of a mineralized collagen–glycosaminoglycan scaffold was increased 6000 folds by the addition of a poly(ε-caprolactone) (PCL) frame without impairment of its osteogenic potential [38]. Similarly, the combination of a freeze-dried collagen scaffold with a 3D-printed β-tricalcium phosphate (β-TCP) structure resulted in a hybrid scaffold whose elastic modulus was three orders of magnitude higher than the one of the collagen, while cellular viability and osteogenic commitment significantly improved compared to the β-TCP structure alone [39]. Moreover, an apatite-collagen-PCL construct showed not only higher elastic modulus and cellular adhesion and

proliferation *in vitro*, but resulted also in more bone formation, better osteointegration and faster bone deposition rate *in vivo* compared to pure PCL scaffolds [40]. However, none of the described hybrid scaffolds employed a developmental TE strategy, but rather aimed at inducing bone formation by intramembranous ossification, thereby exposing the investigated approaches to the limitations to the production of large amounts of mature bone that were discussed above.

In the case of the aligned collagen scaffolds, the inclusion of a synthetic support structure would have the additional advantage of potentially expanding the application of the hybrid scaffolds to osteochondral defects, in addition to the originally-intended critical size bone defects, based on the mechanical properties of the hybrid scaffolds at tissue level. In fact, the previously discussed link between mechanics and bone and cartilage tissue formation could be exploited to stabilize the cartilaginous phase within the hybrid scaffolds during the collagen scaffold-induced endochondral ossification process. The ideal synthetic support structure to be included within the aligned collagen scaffold has the following characteristics:

- Biocompatible material, i.e. a material with the ability to perform its desired function in the absence of local or systemic toxic effects in the host tissue [41];
- Bioresorbable material, i.e. a material that degrades in the body, possibly with a resorption rate matching the growth rate of newly formed bone tissue [42], and whose degradation products are also biocompatible [41];
- High porosity, which not only is generally needed in bone TE strategies to enable nutrients and gas exchange and bone and vessel ingrowth [42,43], but is particularly relevant in the present application to reduce the volume of non-bioactive synthetic material compared to the volume of bioactive aligned collagen. Moreover, an open and interconnected porosity is generally advantageous in bone TE [42];
- Controlled architecture, which serves multiple purposes: first, it helps achieving a high porosity by enabling the choice of the minimum feature size of the support structure; second, it facilitates the production of support structures with open and interconnected porosity; third, it allows the precise spatial distribution of the synthetic material, minimizing possible hindrances of autogenous MSCs recruitment within the aligned collagen scaffolds from the bone marrow. In fact, this modality of cell recruitment has been shown to be pivotal for the successful establishment of the endochondral ossification process *in vivo* [33]; fourth, it enables the controlled tuning of the support structure mechanical properties by means of its architectural features;
- Fatigue resistance in *in vivo* environment, as support structures will be loaded cyclically in consequence of body movements and need to maintain their function as mechanical support until completion of the healing process.

All the aforementioned properties can be achieved by choosing selective laser sintering (SLS) as support structure production technique.

1.4 Selective laser sintering for the production of hybrid scaffolds

SLS is an additive manufacturing technique that enables the production of three-dimensional (3D) objects by selectively melting a substrate in powder form with a CO_2 laser in a layer-by-layer fashion [44,45]. The geometry of the object to be produced is originally given as a 3D computer-aided design (CAD) that is, then, sliced in two-dimensional (2D) layers, which define the scan areas of the laser beam [44].

SLS is particularly attractive for the production of TE scaffolds for three main reasons. First, raw material modifications are not necessary, as opposed to other additive manufacturing techniques that might need, for example, the use of potentially toxic binders [44]. Second, overhanging regions of objects can be reproduced without the introduction of an additional support material, because the unsintered powder in the building chamber naturally acts as support [44,45]. Third, a wide variety of 3D shapes can be successfully reproduced, even those derived from medical imaging methods [46].

One of the materials most commonly used in commercial applications of SLS is polyamide (PA) [44,46]. PA, or nylon, is a semi-crystalline polymer with a large processing temperature window, which makes it particularly suited for SLS [47]. Although PA is biocompatible [48], it is not degradable in the *in vivo* environment. These properties make PA suitable for medical applications such as non-resorbable sutures [49], but limit its use in TE. Nonetheless, a plethora of suitable materials for TE can be used as substrate for SLS, including polymers, ceramics, metals and composites [50]. One of these materials is poly(ε-caprolactone) (PCL) [45,46].

PCL is a biodegradable polyester that received approval for implantation by the Food and Drugs Administration (FDA) [51]. Importantly, the production of PCL scaffolds by SLS for applications in TE has already been suggested for the regeneration of both bone [52] and cartilage [53]. However, the use of PCL in SLS is, at this time, not as widespread as in the case of PA and examples of it are generally found in research rather than in commercial applications [46]. A consequence of the substantially experimental use of PCL in SLS is that ad-hoc SLS process parameters need to be established for specific applications, of which numerous examples can be found in literature [54–57]. Several SLS process parameters can be adjusted [44], such as laser power, laser beam diameter, scan speed, scan spacing, layer thickness, and part bed temperature. The sintering quality of PCL varies based on the choice of SLS process parameters [54]. Therefore, an ideal SLS process parameter set needs to be identified for the production of PCL support structures with optimal sintering quality.

By producing the support structure of the hybrid scaffolds via SLS from PCL, both the material-related requirements, i.e. biocompatibility and bioresorbability, and the

technique-related requirements, i.e. precise control over the resulting architecture and possibility to reproduce a wide variety of shapes, can be met. Due to the few restrictions in shape choice granted by SLS, high porosity and target mechanical properties for the support structures can be obtained by the careful selection of an appropriate design.

An appropriate support structure design is one that grants mechanical competence and fatigue resistance at the specific site of implantation, while at the same time having a high porosity and a material distribution that leaves ample room for the healing process. Concerning the mechanical requirements, it is expected that they differ for applications in critical size bone defects and in osteochondral defects. As previously discussed, numerous experimental and computational observations are available concerning the mechanical environment in fracture gaps or large defects during bone healing [12,58]. Although open questions still remain, e.g. on the most relevant mechanical parameters that influence the healing process or on the precise threshold magnitudes of the mechanical stimuli, the current body of evidence indicates that an environment subjected to low mechanical strains (indicatively <10–15%) is favorable to bone formation. This knowledge can be used to develop support structures of suitable stiffness for the healing of large bone defects. Fewer experimental and computational assessments focus on the study of mechanics during osteochondral defect healing [59,60]. Therefore, the mechanical environment within an osteochondral defect, and the consequent target mechanical properties for the support structure, were investigated by means of a computational model.

1.5 Computational models of osteochondral defects to predict the *in vivo* tissue healing

As previously discussed, there are indications that the formation of tissues in the musculoskeletal system, specifically bone, cartilage, and fibrous tissue (or fibrocartilage), is associated to mechanical cues of different magnitudes [6,7]. These experimental observations motivated the establishment of computational models, both in the context of bone [10,11] and osteochondral defect [59,60] healing, in which biomechanical rules determined tissue formation. For example, the healing of osteochondral defects in minipigs was studied by simulating tissue formation based on thresholds of minimum principal strain, obtaining a good computational representation of the *in vivo* healing process, as determined by comparison with histological sections [59]. In another study, tissue formation within an osteochondral defect was simulated based on a mechanical stimulus computed from octahedral shear strain and fluid velocity and also in this case typical patterns of tissue formation in osteochondral defect healing could be reproduced [60]. These results suggest that mechanical cues, besides biological ones, play a key role in determining the repair outcome of osteochondral defects, although a clear identification of the most relevant mechanical parameter for the process is still lacking.

The mechanics-dependent tissue formation could be exploited to improve osteochondral defect healing by means of scaffolds of appropriate stiffness, using them to establish the most favorable mechanical environment to support the ideal healing. In the case of osteochondral defects, the ideal healing consists on the re-establishment of both a cartilage layer of appropriate thickness at the articular surface and of a healthy subchondral bone. This concept has already been experimentally explored in *in vivo* studies, during which scaffolds of different stiffness were implanted in osteochondral defects and the differences in healing outcome were evaluated [61,62]. However, the investigated scaffolds in all the cited studies differed not only in mechanical properties, but also in architecture, making it particularly challenging to ascribe the observed differences purely to scaffold-dependent mechanical cues [61]. Computational models may overcome this experimental limitation, enabling the establishment of simulations in which architectural and mechanical influences of scaffolds can be clearly distinguished and identified.

The healing of osteochondral and chondral defects in dependency of scaffold mechanical properties has already been investigated in computational models of the knee joint featuring a simplified axisymmetric [63] and a patient-specific 3D [64] geometry, respectively. Both studies suggested the need for depth-dependent scaffold properties to achieve the ideal defect healing, with decreasing scaffold elastic modulus and increasing scaffold permeability from the articular surface to the defect base. However, both studies considered the scaffold as a uniform material, completely filling the defect without having distinct geometrical features. Such a scaffold representation may be appropriate to simulate hydrogels. However, many of the investigated scaffolds for osteochondral defect regeneration have non-negligible 3D architectures [20], which may influence the healing process by generating non-uniform load distributions or by limiting cellular access to certain areas. Therefore, there is the need for a computational model to study the mechanics-dependent healing of osteochondral defects in dependency of both mechanical and geometrical properties of scaffolds.

1.6 Thesis aim

In the previous paragraphs, the body of evidence showing a correlation between formation of bone and cartilage with mechanical stimuli of different magnitude was introduced. Moreover, an *in situ* developmental TE approach for the treatment of critical size bone defects, consisting of a collagen scaffold with aligned architecture inducing bone formation by endochondral ossification, was presented and its advantages in terms of bioactivity and disadvantages in terms of mechanical stiffness were discussed (Figure 2). The development of a hybrid scaffold composed of the collagen scaffold and a synthetic support structure was proposed as strategy to improve the mechanical stiffness of the collagen scaffold without hindering its favorable biological interactions.

The overall aim of the work presented here is to design, produce, and test the proposed hybrid scaffold and to establish the target properties for its employment in the treatment of both osteochondral and large bone defects by exploiting the dependency on mechanics of cartilage and bone tissue formation. It is hypothesized that hybrid scaffold-dependent mechanical cues could be employed to steer the endochondral ossification process promoted by the collagen scaffold, bringing the developmental biological process to its fulfillment, i.e. bone formation, or stabilizing it at the cartilaginous phase by generating a mechanical environment with lower or higher strain, respectively. The proposed concept will be explored by working on three main aspects.

First, a stiff and a compliant support structure to be incorporated in the hybrid scaffold will be developed. The process parameters of the chosen production technique for the support structures, i.e. SLS, will be adapted to the specific application and material, i.e. PCL. The architecture of the support structures will be engineered to fit the geometrical and mechanical constraints of the chosen *in vivo* model, i.e. large bone defects in rats, while fulfilling the requirements established for the hybrid scaffold, i.e. high porosity and optimized spatial distribution of the synthetic material. Moreover, architectures with a significant difference in stiffness, but similar porosity, will be developed for the stiff and compliant support structures and both will be optimized to resist without breakage repeated loading cycles in *in vivo*-like conditions by means of a bioreactor test.

Second, the stiff and compliant support structures will be incorporated into collagen scaffolds, generating the stiff and compliant hybrid scaffolds, respectively. The preservation of key features pertaining to both collagen scaffolds and support structures after hybrid scaffold production will be tested, and specifically: the stiffness and fatigue resistance of the support structures; and the aligned architecture and ease of cellular migration within the scaffold of the collagen scaffolds. Moreover, the improved stiffness of the hybrid scaffolds compared to the collagen scaffolds resulting from the inclusion of the support structure will be proven.

Third, the influence on tissue formation of mechanical properties and architectural features of a scaffold for osteochondral defect healing will be investigated by means of a computational model. The aim of the computational model is to derive indications on the mechanical and architectural target properties of hybrid scaffolds for the treatment of osteochondral defects.

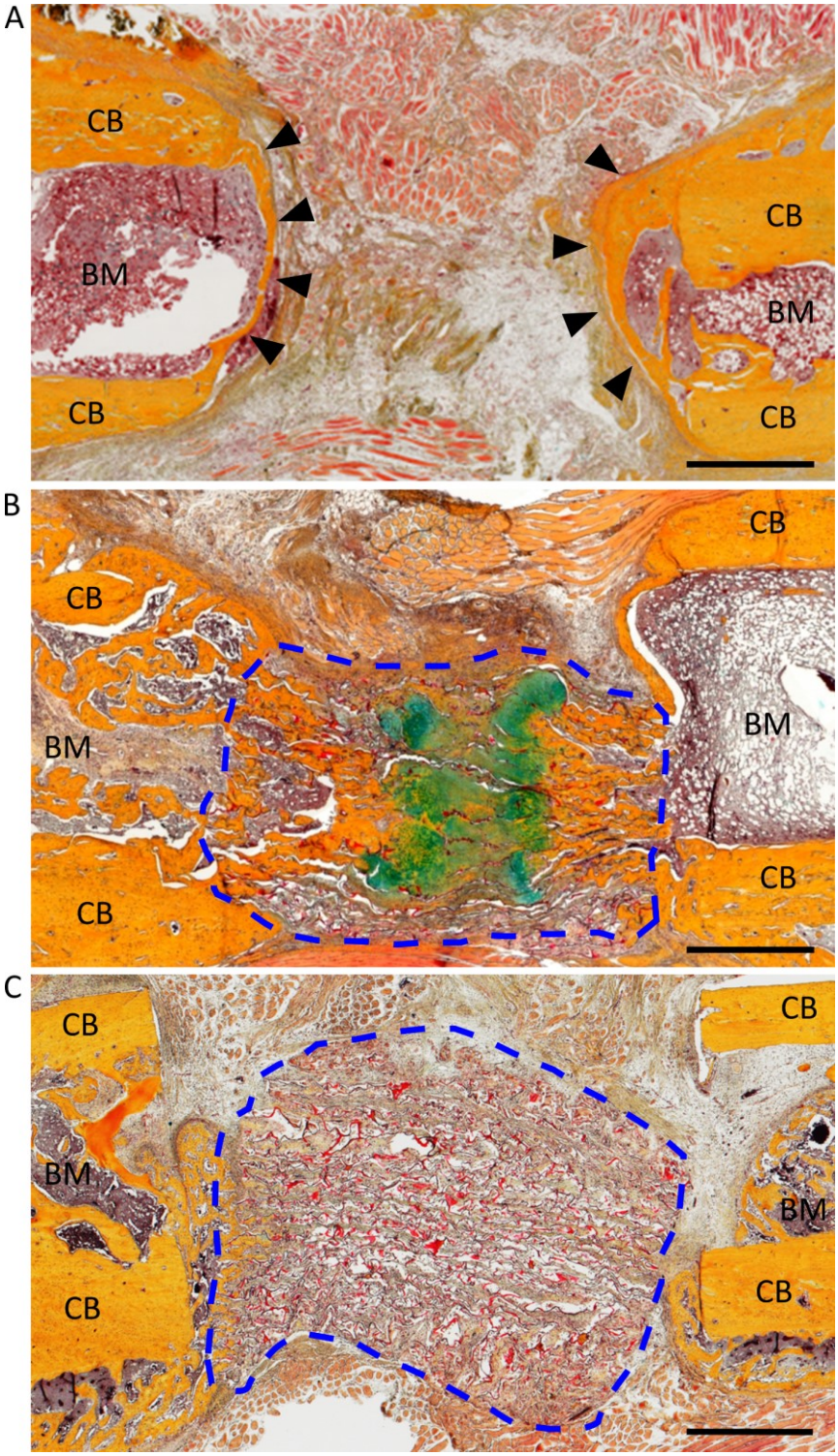

Figure 2: Representative histological images of large bone defect healing in rat. A) Healing of untreated large bone defect (6 weeks after surgery, reproduced from [33] under CC BY 4.0 [65] with the addition of arrows and legend). Bone grew to form a cap around the medullar cavities (black arrows) and not in the bridging direction; B) example of successful healing of large bone defect treated with collagen scaffold (6 weeks after surgery); C) example of unsuccessful bone ingrowth into the collagen scaffold (3 weeks after surgery). The collagen scaffold was displaced and deformed by the surrounding tissue forces. Scale bars are 1 mm. Movat pentachrome staining: bone and cartilage are stained in yellow and green, respectively. The blue dashed lines outline the collagen scaffolds. CB: intact cortical bone. BM: bone marrow space. Images courtesy of Dr. Ansgar Petersen (Julius Wolff Institute).

2 Methods

2.1 Production of materials

2.1.1 CAD of support structures

All CAD of support structures were built in SolidWorks (Dassault Système).

A first screening of possible support structure geometries was performed by building a CAD library, whose elements had a common basic shape and geometrical features that were systematically varied. The common basic shape consisted of a hollow cylinder with hexagonal cross section, having a height of 10 mm, a maximum width of 5 mm, a side length of 2.5 mm, and a wall thickness of 0.5 mm. The systematic feature variation was performed on the pore pattern designed on the sides of the hexagonal cylinders. Specifically, five main pore types were tested: equilateral hexagons, non-equilateral hexagons, hexagons with two 60° angles, irregular shapes, and shapes with a size gradient. Within each group of pore types, four types of reinforcing elements were tested: no reinforce, vertical reinforce, oblique reinforce, and combined vertical and oblique reinforce. The choice of the hexagonal cross-section was directed by the intended morphology of larger support structures for human use, which will be composed of a honeycomb structure of the single units here investigated.

From the CAD library, which featured a total of 51 designs, seven geometries were selected based on stiffness and morphology, as later described, to be produced by SLS from PA. The chosen designs were adapted for the subsequent mechanical testing by adding a 0.5 mm high hexagonal ring on the top and bottom surfaces, bringing the total height to 11 mm. The resulting designs were named CAD1 to CAD7.

Starting from the analysis of the mechanical properties of the CAD1-CAD7 designs, stiff and compliant support structure architectures were defined and improved based on an interplay of experimental and computational evaluations, which determined the features of the designs as described subsequently. The architectural features of the most relevant designs that were investigated are here summarized (Table 1).

Table 1: Architectural features of the most relevant investigated designs for stiff and compliant support structures.

Name	Type	Cross-section	Width (mm)	Height (mm)	Strut thickness (µm)
S_P	Stiff	Hexagonal	5.00	5.33	500
C_P	Compliant	Hexagonal	5.00	5.33	500
S_H	Stiff	Hexagonal	4.33	5.20	540
C_H	Compliant	Hexagonal	4.33	5.20	540
S_C	Stiff	Circular	3.70	5.20	540
C_C	Compliant	Circular	3.70	5.20	540

Preliminary stiff and compliant support structures were called S_P and C_P, respectively, and had height of 5.33 mm, a maximum width of 5 mm, a side length of 2.5 mm, a wall thickness of 0.5 mm, and strut thickness of 500 µm.

Stiff and compliant support structures with hexagonal cross-section and size adapted to fit the *in vivo* model, i.e. large bone defects in rats, were called S_H and C_H, respectively, and had a height of 5.2 mm, a maximum width of 4.33 mm, and a strut thickness of 540 µm. The required size was determined by building the cross-section of an average rat bone. Specifically, the maximum and minimum inner and outer femur diameters were measured from micro-computed tomographic (µCT) images of large bone defects in n = 10 rats (weight of 260–280 g). The cross-section of the average rat bone was built in SolidWorks and used to evaluate the placement and fitting of the support structure design. The height of the support structures for *in vivo* experiments was chosen based on the height of bone to be surgically excised (5 mm), with an addition of 0.2 mm to enable the press-fit placement of the scaffolds.

Stiff and compliant support structures with circular cross-sections were called S_C and C_C, respectively. Their inner and outer diameter were 2.6 and 3.7 mm, respectively. The height was 5.2 mm and the strut thickness was 540 µm.

2.1.2 Finite element (FE) analysis based on CAD models

The architecture-dependent mechanical behaviour of every CAD was first evaluated by FE analyses in compressive conditions. All FE analyses were performed in Abaqus (Dassault Système).

Each CAD-based model was meshed with tetrahedral elements with seed size of 0.1 mm. A clamp boundary condition was imposed to the bottom surface, while a 3% compressive displacement was applied to the top surface. Linear elastic material properties were used. CAD-based models to be produced from PA were assigned a material elastic modulus of 1700 MPa [48] and a Poisson's ratio of 0.3. As the elastic modulus of sintered PCL was unknown, the input value for the simulation of CAD-based models to be produced from PCL was determined by testing different values and selecting the one that yielded the support structure stiffness that best matched the experimental data, resulting in a material elastic modulus of 70 MPa and a Poisson's ratio of 0.3. The computational stiffness (k_C) of each design was measured with Equation 1:

$$k_C = \frac{RF}{\Delta L} \qquad \text{Equation 1}$$

Where RF is the reaction force and ΔL is the applied displacement. For an easier comparison with the mechanical properties of biological tissues, the support structures were considered to be uniform materials, whose computational elastic modulus (E_C) was calculated as indicated by Equation 2:

$$E_C = \frac{\sigma}{\varepsilon} = \frac{L}{A} \cdot k_C \qquad \text{Equation 2}$$

Where σ is the stress, ε is the strain, A is the cross-section, and L is the initial height.

FE analyses were employed also to assess the theoretical relationship between strut diameter and stiffness of the PCL support structures with S_P design. Specifically, the S_P

design was reproduced by six CAD-based models that had its same architecture, but computational strut diameter (D_C) of 310, 400, 500, 600, 700, and 800 µm. These six CAD-based models were tested in compression by FE analysis as previously described and their stiffness, approximated by E_C, was calculated with Equation 2.

2.1.3 Production of support structures

Commercial suppliers produced the PA support structures by SLS: specifically, Citim (Germany) for CAD1-CAD7 and BlueProduction (Germany) for S_P and C_P. Individual support structures were connected by transversal bridges, which were manually cut after production. Moreover, a protective cage was sintered together with the support structures to reduce the risk of damages during shipment.

PCL powders were purchased from Aqtis Medical BV (Netherlands) with nominal molecular weight of 60,000 or 100,000 g/mol and particle size distribution of 25–50 µm. Additionally, the powder with nominal molecular weight of 60,000 g/mol was purchased with a particle size distribution of 50–80 µm. The influence of the PCL powder on the sintering process was assessed by producing the same design (S_P) with each purchased powder and evaluating its mechanical properties as later described.

PCL support structures were produced via SLS by the Fraunhofer Institute for Laser Technology (ILT, Aachen, Germany) using a laboratory SLS machine equipped with an ionizer (SMC Deutschland GmbH) to avoid powder agglomeration. Initially, the optimal SLS process parameters were investigated by producing the same design (S_P) from the same PCL powder (nominal molecular weight of 60,000 g/mol and particle size distribution of 50–80 µm) with variations of laser power (P_L), laser beam diameter (*BD*), and laser beam compensation (*BC*), as indicated in Table 2. The meaning of P_L, *BD*, and *BC* within the SLS process is illustrated in Figure 3. The other processing parameters were kept constant as follows: 50 mm/s scan speed; 67° scan pattern rotation between layers; unidirectional scans; 20 µm hatch distance; 50 µm layer thickness.

Table 2: Values of SLS process parameters that were implemented. P_L: laser power; *BD*: laser beam diameter; *BC*: laser beam compensation.

P_L (W)	*BD* (µm)	*BC* (µm)
0.30	260	150
0.35	390	200
0.40		205
0.45		210
0.50		225
0.60		230
0.70		

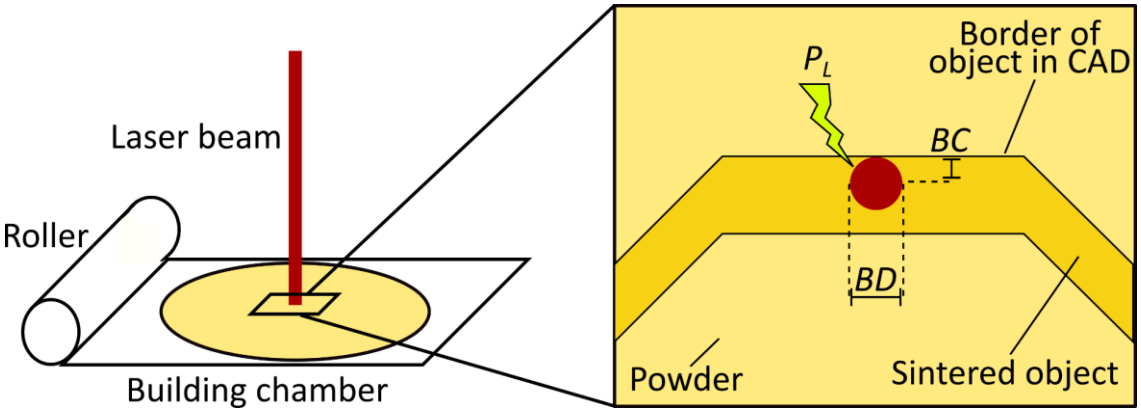

Figure 3: Schematic representation of selective laser sintering (SLS). The insert shows the SLS process parameters that were systematically varied: laser power (P_L), laser beam compensation (*BC*), and laser beam diameter (*BD*).

At least n = 3 sample/parameter set were tested. Results of the SLS process were assessed by mechanical and morphological evaluation of the produced support structures, as later described.

The following SLS process parameters were selected for the production of the stiff and compliant support structures to be included in the hybrid scaffolds, i.e. S_C and C_C, respectively: *BC* = 210 µm; *BD* = 260 µm; P_L = 0.35 W for the struts, P_L = 0.30 W at strut connections and P_L = 0.15 W for the top and bottom rings. Moreover, three layers were not sintered at the beginning of the overhanging regions of the architectures to guarantee a better design reproduction.

Two sterilization methods were tested for the support structures, namely gamma irradiation and ethylene oxide (EtOx). S_P support structures were produced with the following set of SLS process parameters: *BC* = 200 µm; *BD* = 260 µm; P_L = 0.40 W. Subsequently, n = 3 support structures each were sterilized by EtOx and gamma irradiation, while n = 3 were kept unsterile as reference. Sterilization was performed by HA2 Medizintechnik GmbH (Germany). Possible effects of sterilization on the support structures were evaluated by mechanical testing and molecular weight analysis, as later described.

2.1.4 Improvement of support structure design

A topology optimization software (TOSCA, Dassault Système) was applied to the preliminary stiff design (S_P) with the objective function set to strain minimization, i.e. stiffness maximization. The load and boundary conditions of the topology optimization analysis, as well as the PA material definition, were the same as in the previously described FE analysis. Additionally, a volume reduction of 30% was imposed. The topology optimization process identified regions of the design that were not contributing to the load bearing ability of the support structure. The S_P design was manually modified to reduce the extent of these regions.

Experimental observations identified the sharp edges of the pores of the S_P design as points of crack nucleation. Therefore, the design was modified by smoothening all sharp

edges. The modifications applied to the preliminary stiff design were implemented also in the compliant design.

Stiff and compliant support structure architectures were improved to sustain fatigue by design-test feedback loops. Support structure prototypes were dynamically tested in compression in a bioreactor system as later described. If a specific support structure architecture could not undergo a week of continuous mechanical stimulation without breaking, its design was modified. In this phase, the cross-section of the support structures was modified from a hexagonal to a circular one, generating the S_C and C_C stiff and compliant support structures, respectively.

2.1.5 Production of multiscale hybrid scaffolds

Multiscale hybrid scaffolds were produced by Matricel GmbH (Herzogenrath, Germany) by incorporating stiff and compliant support structures of the types S_C and C_C, respectively, in a collagen dispersion with 1.5 wt% collagen content. Support structures were kept upright by an ad-hoc silicon mold. Subsequently, the collagen dispersion underwent directional freezing and freeze-drying, generating the collagen scaffold with aligned walls [66]. Excess collagen surrounding the support structures was manually removed before collagen crosslinking. Finally, scaffolds underwent sterilization by EtOx (HA2 Medizintechnik GmbH). Sheets of collagen with aligned porosity were concomitantly produced in the same way. Collagen scaffolds to be used as controls were cut from the collagen sheets with biopsy punches (diameter 4 mm, Kai Europe GmbH).

2.2 Characterization of materials

2.2.1 Molecular weight analysis

Molecular weight analysis was performed on the PCL powder that was selected for support structure production (nominal molecular weight of 60,000 g/mol and particle size distribution of 50–80 µm) and on the support structures that underwent sterilization either by EtOx or by gamma irradiation, as well as on the unsterile control. The molecular weight distribution was measured by size exclusion chromatography (SEC, Agilent Technologies 1200 Series, USA) at the Politecnico di Torino (Italy) following a previously published protocol [67]. Briefly, PCL powder and support structures were dissolved with a concentration of 2 mg/ml in a solution of N,N-dimethylformamide (Chromasolv HPCL grade, CarloErba Reagents, Italy) and lithium bromide (Sigma Aldrich, Italy) at 0.1% w/v. The solution was filtered with a 0.45 µm poly(tetrafluoroethylene) syringe filter (Lab Logistic Group GmbH, USA) and analyzed at 55°C with a flow rate of 0.5 ml/min through two Waters Styragel columns (HR1 and HR4). Number average molecular weight ($\bar{M}_n$), weight average molecular weight ($\bar{M}_w$), and dispersity index ($DI = \bar{M}_w/\bar{M}_n$) were measured with the Agilent ChemStation software based on a

calibration curve of poly(methyl methacrylate) standards having $\overline{M}_n$ ranging from 4,000 to 200,000 g/mol.

2.2.2 Mechanical test

2.2.2.1 Unconfined static monoaxial compression test

Static mechanical tests in unconfined monoaxial compression were performed in a BOSE Test Bench (LM1 TestBench, TA Instrument ElectroForce System Group, USA). All designs of PCL support structures were tested in dry conditions, while multiscale hybrid scaffolds and PA support structures of type S_P and C_P were tested completely immersed in phosphate buffered saline (PBS, Gibco, Life Technologies Limited). PA support structures were tested in wet conditions because plasticization due to moisture sorption (i.e. the physical and chemical process of one substance becoming attached to another) in PA makes the polymer softer in a wet environment [68], an effect that preliminary tests did not reveal in PCL support structures (data not shown). Hybrid scaffolds were tested in wet conditions because collagen swells and softens as a consequence of water uptake. Tests were performed by applying a displacement and recording the reaction force with a 222.5 N load cell, except for circular compliant support structures (C_C) and the corresponding hybrid scaffolds, whose reaction force was recorded with a 9.8 N load cell. Collagen scaffolds were tested as reference in wet conditions and their reaction force was recorded with a 0.49 N load cell.

Samples were tested three times up to 3% compression, except C_C support structures and the corresponding hybrid scaffolds, which were tested three times up to 10% compression. In all cases, the displacement was applied with a speed of 0.016 mm/s and it was followed by a 30 s dwell. All test conditions are summarized in Table 3. Sample stiffness (k) was evaluated from the linear trait of the force-displacement curves. As for the computational evaluation, the support structures of type S_P and C_P were initially approximated to a uniform material, whose elastic modulus (E) was calculated by introducing k instead of k_C in Equation 2. This approximation was not employed for subsequent support structure architectures, for which k is reported. At least n = 3 samples per type were tested and results are given as average ± standard deviation.

Table 3: Test conditions in static unconstrained monoaxial compression. PA: polyamide. PCL: poly(ε-caprolactone).

Sample	**Material**	**Test condition**	**Load cell (N)**	**Applied displacement (%)**
CAD1-CAD7	PA	Dry	222.5	3
S_P, C_P	PA	Wet	222.5	3
S_P, C_P, S_H, C_H, S_C	PCL	Dry	222.5	3
C_C	PCL	Dry	9.8	10
Stiff hybrid scaffold	PCL and collagen	Wet	222.5	3
Compliant hybrid scaffold	PCL and collagen	Wet	9.8	10
Collagen scaffold	Collagen	Wet	0.49	20

2.2.2.2 Dynamic fatigue test

Dynamic mechanical tests in compression were performed in a bioreactor system that was described in details elsewhere [69] and that is schematically represented in Figure 4A. Briefly, the bioreactor featured a sample chamber, in which samples could be exposed to mechanical stimulation thanks to the movement of an upper holder. The movement of the lower holder could be used to correctly place the sample in contact with the upper holder. Samples were completely immersed in 10% expansion medium, which was composed of Dulbecco's modified Eagle's medium (DMEM, Sigma), 10% fetal bovine serum (FBS, Biochrom AG), 1% penicillin/streptomycin (P/S, Biochrom AG), and 1% non-essential amminoacids (NEA, Bio & Sell). A micro-pump granted medium circulation between the sample chamber and a reservoir, where gas exchange took place. The bioreactor system was kept at 37°C and 5% CO_2, simulating the *in vivo* environment.

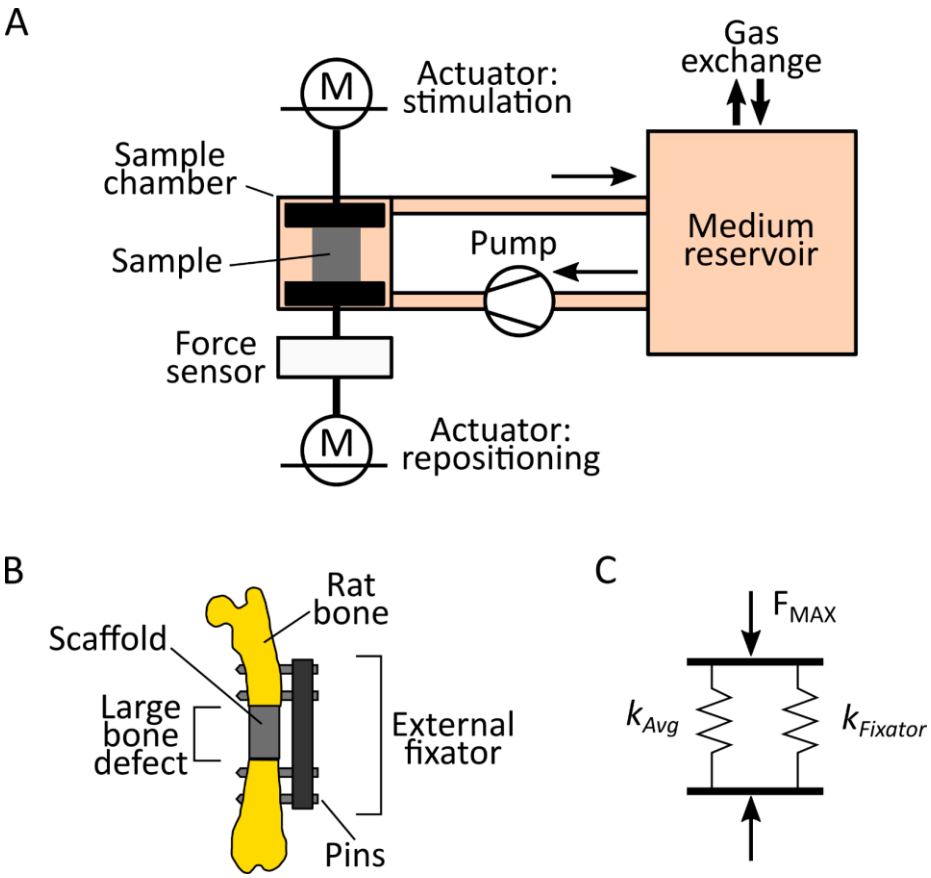

Figure 4: Schematic representation of dynamic fatigue test in the bioreactor simulating the *in vivo* environment. A) Bioreactor system; B) *in vivo* large bone defect model in rat; C) representation of *in vivo* experimental setup as a spring system. The external fixator and the scaffold are represented as two parallel springs of stiffness $k_{Fixator}$ and k_{Avg}, respectively, subjected to a force F_{MAX}.

For one week, samples were cyclically loaded in compression at a frequency of 2 Hz with a loading pattern simulating the one measured in rat large bone defects *in vivo*, amounting to a total of approximately 1,209,600 compression cycles. The number of cycles was chosen as a good compromise between the need to observe the materials subjected to a high number of repetitive loads and experimental times. The amplitude of the applied load was specifically calculated for each sample type to simulate the contribution of an external fixator with stiffness $k_{Fixator}$ = 13.5 N/mm, as in the *in vivo* situation (Figure 4B). The external fixator and the sample were considered as two parallel springs subjected to a force F_{MAX} = 550 g ≈ 5.4 N (Figure 4C), which was the maximum force experimentally recorded in large bone defects models in rat (unpublished data). The displacement (ΔL) of the sample-fixator system was calculated with Equation 3:

$$\Delta L = \frac{F_{MAX}}{k_{Fixator}+k_{Avg}} \qquad \text{Equation 3}$$

Where k_{Avg} is the average stiffness of a specific sample type measured by monoaxial compression tests. The portion of F_{MAX} acting on a specific sample type, and thereby the

force amplitude that was imposed during the cyclic loading in the bioreactor (F_{BR}), was calculated with Equation 4:

$$F_{BR} = \Delta L \cdot k_{Avg} \qquad \text{Equation 4}$$

Every 12 hours, a linear compression test was performed by applying a 0.15 mm compression with a speed of 0.015 mm/s. From the linear compression tests, *k* was measured as the slope of the linear trait of the force-displacement curves. If plastic deformation would take place in a sample, reducing its height, the lower holder would move up to restore the contact of the sample with the upper holder. The repositioning of the samples simulated the presence of the external fixator as well. Therefore, in case of breakage with complete loss of mechanical competence, each sample type would result in a maximum repositioning (Δh_{MAX}) as calculated with Equation 5:

$$\Delta h_{MAX} = \frac{F_{BR}}{k_{Fixator}} \qquad \text{Equation 5}$$

At least n = 5 samples per type were tested, except compliant hybrid scaffolds (n = 3), and results are given as average ± standard deviation.

2.2.3 Morphological evaluation

The porosity (*P*) of each CAD was evaluated as indicated by Equation 6:

$$P = 100 * \left(1 - \frac{V}{V_S}\right) \qquad \text{Equation 6}$$

Where *V* is the volume of the CAD and V_S is its solid volume, i.e. the volume the CAD would have if it had no porosity.

The morphology of the support structures was evaluated by measuring their height, width, strut diameter (D_S), and strut molten cross-sectional area (A_M).

Height and width were measured with a digital caliper (DigitCal, Tesa). The measurement of D_S was performed at the ILT from light microscope (SMZ1270, Nikon) images using the software NIS-Elements D 4.30.02. To measure A_M, support structures were first cut to ¾ of their height by embedment in TissueTek® (Sakura Finetek Europe B.V.) and subsequent trimming with a cryomicrotome (Leica CM3550 S). TissueTek® was removed by repeated washings in deionized water, then samples were gold-sputtered for 30 s at 8 Pa pressure and 30 mA electrical current. Subsequently, samples (n = 1 per type) were imaged with a scanning electron microscope (SEM, JCM-6000, Jeol) by secondary electron imaging in high vacuum. A_M was measured from SEM images using Fiji (NIH) [70] by manually contouring the solid areas in which individual PCL particles were not distinguishable. For each investigated sample, the cross-sectional area of 12 struts was measured. The molten diameter (D_M) was calculated from A_M as the diameter of a circular cross-section with Equation 7:

$$D_M = 2\sqrt{\frac{A_M}{\pi}}$$ Equation 7

Results of D_S, A_M, and D_M are given as average ± standard deviation.

Hybrid scaffolds were morphologically characterized in terms of alignment of the collagen walls. An accurate wall visualization was achieved by combining second harmonic (SH) imaging of fibrillar collagen type I with the immunofluorescent imaging of adsorbed FBS-derived fibronectin, as previously suggested elsewhere [71]. SH imaging is a technique that enables an excellent visualization of collagen type I by taking advantage of the aligned fibrillar structure of this protein [72]. Compliant and stiff hybrid scaffolds and collagen scaffolds to be used as controls were incubated overnight in a solution of FBS and P/S at 37°C. After one washing in PBS, samples were fixed by 5 hours incubation in 4% paraformaldehyde (PFA) and 1 hour immersion in a 25 mM solution of ammonium chloride (Merck KGaA) in PBS. Subsequently, samples were embedded in TissueTek® and cut at the cryomicrotome until reaching their middle. TissueTek® was removed by repeated washings in PBS, then samples were stained for fibronectin (ab23750, Abcam, for the staining protocol see Table A.2-1). Image stacks with a volume of 30 µm and a z step of 5 µm were recorded using a confocal microscope (Leica SP5 II, Leica Mikrosysteme Vetrieb GmbH) equipped with a x25 water immersion objective. SH imaging was performed with excitation at 910 nm and detection at 440–460 nm. For each sample, four images featuring the whole sample in plane and similar SH and fibronectin signals were extracted from the stack and used in the orientation analysis. Collagen walls were identified by combining the SH and fibronectin channels, then their orientation was evaluated with the OrientationJ plugin in Fiji [73]. The intensity values measured at each angle were normalized to the sum of all the values over 360°. For each scaffold type, n = 3 samples were analyzed and results are given as average ± standard deviation.

2.2.4 Cytocompatibility of PCL support structures

2.2.4.1 Cell culture

Primary human mesenchymal stromal cells (MSCs) were cultured in 10% MSCs expansion medium, which was composed of Dulbecco's modified Eagle's medium (1000 mg/l glucose, Sigma), 10% FBS, 1% P/S, and 1% L-glutamine (GlutaMAX, Invitrogen). Trypsinization (PAA Laboratories GmbH) was performed at 80% confluency. MSCs were used in passages 3 to 5.

2.2.4.2 Cytocompatibility assay

The cytocompatibility of the prototypes "A" to "F" (Table 9) of the preliminary stiff support structure (S_P) was assessed by using them to condition batches of 10% MSCs

expansion medium and subsequently using the conditioned medium in *in vitro* cell culture. The effect of the conditioned medium on cellular metabolic activity and proliferation was evaluated.

MSCs were seeded in 48-well plates with a 30% confluency. For each experimental time point (day 0, 3, and 6) and for each condition (control and “A” to “F”), n = 3 wells were seeded and subsequently conditioned. The day 0 time point was 24 hours after cell seeding. MSCs cultured in 10% expansion medium were used as control. Cell-seeded wells were surrounded by PBS-filled wells to reduce medium evaporation.

Batches of conditioned medium were prepared by immersing each prototype in 3 ml of 10% MSCs expansion medium 24 hours before the first employment of the conditioned medium in cell culture and by incubating the batches at 37°C and 5% CO_2. At the day 0 and 3 time points, 200 µl/well of conditioned medium were retrieved from the batches and used in cell culture. Subsequently, the same volume was refilled in the batches with fresh 10% MSCs expansion medium.

At day 0, 3, and 6, cellular metabolic activity and proliferation were assessed by AlamarBlue (#DAL 1100, Invitrogen) and CyQuant (#C7026, Thermo Fischer Scientific) assays, respectively, whose results in terms of fluorescence intensity values were measured with an Infinite M200 Pro plate reader (Tecan). Four independent repetitions of the cytocompatibility assay were performed.

For each plate, wells whose intensity values were lower than 50% of the average of the other two wells of the same condition were considered outliers and removed from the data set. Similarly, repetitions whose results were lower than 50% of the average of the other three repetitions were considered outliers and removed from the data set.

Results were normalized to day 0 and are reported as average fold change ± standard deviation.

2.2.5 Evaluation of cellular migration into hybrid scaffolds

2.2.5.1 Migration assay

Cell culture was performed as described in paragraph 2.2.4.1. MSCs migration into hybrid scaffolds was evaluated using cell pellets as cell sources. Cell pellets of 0.5×10^6 cells were prepared by pipetting 500 µl of a 1000 cell/µl suspension in 15-ml Falcon tubes and by filling up the volume to 1 ml with 10% MSCs expansion medium (Figure 5A). Falcons were centrifuged at 1300 rpm for 1 minute, then incubated overnight at 37°C and 5% CO_2 with the lid not completely sealed to enable gas exchange.

Samples were placed vertically in a 24-well plate. Ad-hoc silicon holders were used to avoid sample displacement. Wells were filled with 10% MSCs expansion medium until the level of the top sample surface. Cell pellets were retrieved using a 1-ml tip with

trimmed edge (Figure 5B) and placed in the middle of the top surface of the samples (Figure 5C). Samples were incubated at 37°C and 5% CO_2 for 3 hours to enable cell adhesion to the materials. Subsequently, samples were transferred to a 12-well plate with 2 ml of 10% MSCs expansion medium. Importantly, samples were placed laying horizontally to reduce the influence of gravity on the migration process (Figure 5D). Cell culture was carried on for 4 days without medium exchange.

At least n = 6 samples per scaffold types were tested in at least two independent experiments. Collagen scaffolds were also tested as controls.

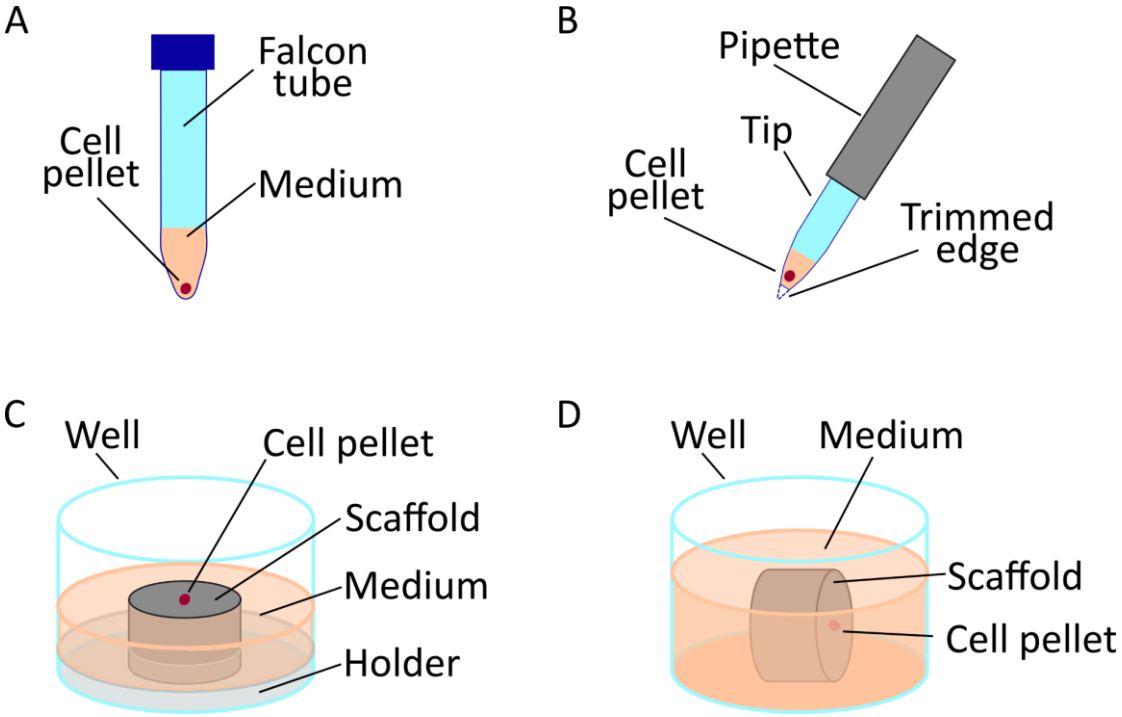

Figure 5: Schematic representation of migration assay. A) Cell pellet formation in falcon tube; B) Cell pellet retrieval with trimmed-edge tip; C) cell pellet placement on top of a scaffold during adhesion phase (3 hours); D) scaffold placement during *in vitro* cell culture (4 days).

2.2.5.2 Sample processing and staining

Fixation was performed by 5 hours incubation in 4% PFA, followed by 1 hour incubation in a 25 mM solution of ammonium chloride in PBS. Subsequently, samples were placed in a 5% solution of sucrose/gelatin and incubated at 37°C for 5 hours. Then, samples were transferred to a 12-well plate in a number of 1 to 3 samples per well. All samples were equally spaced, with the cell-seeded surface towards the center of the well and the bottom surface in contact with the well side. Wells were filled with sucrose/gelatin solution in such a way as to completely cover the samples, but avoiding floating. Well plates were, then, incubated at 4°C for 1 hour to solidify the sucrose/gelatin solution. Cubes of solid sucrose/gelatin containing the samples were cut from the wells with a scalpel, leaving 3-4 mm of extra material on the cell-seeded side. A 4-5 mm long piece of suture material was stuck in the extra material, in such a way as to point the center

of the cell pellet. The sucrose/gelatin cubes were embedded in TissueTek® and cut at the cryomicrotome until reaching the suture material, i.e. the middle of the sample. TissueTek and sucrose/gelatin were removed by repeated washings in PBS. Then, samples were stained for cell nuclei (DAPI, #D3571, Thermo Fisher) and F-actin (Phalloidin Alexa 488, #A12379, Thermo Fisher) following the protocol in Table A.3-1 and imaged at the confocal microscope, recording image stacks with a volume of 75 µm and a z step spacing of 5 µm.

2.2.5.3 Evaluation of cell migration distance

Cellular migration distance was evaluated from the maximum projection of four consecutive images of the stacks recorded with the confocal microscope. The selected images featured the sample completely in plane and similar staining intensity. The analysis was performed with an ad-hoc Fiji macro. The analysis steps were performed on the cell nuclei channel. The cell pellet was manually outlined and excluded from the analysis region. A threshold was applied to identify the cell nuclei. As it was not possible to completely exclude the collagen-derived noise simply by thresholding, the cell nuclei mask that was automatically generated by Fiji was manually modified to reduce the collagen-dependent signals. Then, the coordinates of the cell nuclei were recorded and their distance from the cell pellet outline was measured, obtaining the cellular migration distance (d). Results are given as the average of the median d ± standard deviation.

Significance levels were tested by a two-sided Mann-Whitney-U statistical test performed in Origin 2019b (OriginLab Corporation). Values of $p > 0.05$ were considered non-significant (n.s.).

2.3 Computational model of osteochondral defect healing

To investigate the influence of the mechanical and architectural properties of scaffolds on the healing process of osteochondral defects, a computational model was established. The healing of an osteochondral defect in a knee joint model with axisymmetric geometry was simulated by defining a biomechanical stimulus based on strain and fluid velocity in the defect. Such biomechanical stimulus was, then, used to determine cellular behavior, as later described. Consequently to cellular activities, the tissue composition in the osteochondral defect varied, thereby altering the strain and fluid velocity distributions. The analysis of strain and fluid velocity and the corresponding simulation of cellular activities were iteratively repeated until healing of the simulated osteochondral defect. Scaffolds with systematically-varied mechanical and architectural properties were modelled in the osteochondral defect and their influence on the healing process was evaluated.

2.3.1 FE model of osteochondral defect

An axisymmetric FE model of a femoral condyle was built in Abaqus following a previously published method [60]. Briefly, the femoral condyle was modelled as a compressed sphere with a radius of 20 mm, lying on a tibia plateau represented by a rigid wire (Figure 6A). The model featured cancellous bone, subchondral bone, cartilage, an osteochondral defect initially filled with granulation tissue, and a meniscus. All materials were modelled as isotropic and poroelastic (Table 4), with the exception of cartilage and meniscus. Due to its large deformation, cartilage was modelled as isotropic and hyperelastic with neo-Hookean strain energy potential and the following material parameters: C_{10} = 2.14 MPa and D_1 = 0.399 MPa. The meniscus was modelled as transversely isotropic and poroelastic, with the following material parameters: $E_1 = E_2$ = 0.5 MPa; E_3 = 100 MPa; v_{12} = 0.5; $v_{13} = v_{23}$ = 0.0015; G_{12} = 0.167 MPa; $G_{13} = G_{23}$ = 0.05 MPa. The variables E, v, and G indicate the elastic modulus, Poisson's ratio, and shear modulus, respectively. The indexes 1, 2, and 3 indicate the radial, axial, and circumferential directions, respectively. For all poroelastic materials, the specific weight of wetting liquid was 9.74×10^{-6} N/mm^3 and the bulk modulus of fluid was 2300 MPa [74].

Table 4: Poroelastic material properties of tissues.

Tissues	**Elasticity** [60]		**Permeability** [60]		**Porous bulk moduli** [74]
	Elastic Modulus (MPa)	**Poisson Ratio**	**Permeability (mm/s)**	**Void Ratio**	**Bulk Modulus of Grains (MPa)**
Cancellous Bone	6000	0.3	3.63×10^{-8}	4	13920
Subchondral Bone	17000	0.3	9.74×10^{-11}	0.042	13920
Granulation Tissue	0.2	0.167	9.74×10^{-8}	4	2300
Poroelastic Cartilage	10	0.167	4.87×10^{-8}	4	3700
Fibrous Tissue	2	0.167	9.74×10^{-8}	4	2300

The defect region was meshed with 1600 elements type CAX8RP and seed size of 0.125 mm. The seed size increased with distance from the defect region, reaching a maximum of 0.8 mm in the meniscus and in the proximal-peripheral side of the femoral

condyle (Figure 6A). A clamp boundary condition was applied to the reference point of the tibial plateau, which was located at the axis of symmetry. Interaction properties with frictionless tangential behavior and "hard contact" in the normal direction were defined between femoral condyle and tibial plateau, femoral condyle and meniscus, and meniscus and tibial plateau. Initial conditions of 0 MPa pore pressure and 1 mm^3/mm^3 saturation were defined for the whole model.

A 1 s compressive loading step was applied to the model, followed by a 0.5 s consolidation step. During the loading step, a 0.637 MPa pressure was applied on the proximal surface of the cancellous bone. During the consolidation step, a pore pressure of 0 MPa was applied to the free cartilage edges.

At the end of the simulation, the octahedral shear strain (γ) and fluid velocity (v) in the defect region were used to calculate the strain-dependent cellular behavior as later described.

Two additional FE models of knee femoral condyles were built featuring a scaffold in the defect. These models differed from the model with empty osteochondral defect only in regards to the material properties in the defect. Two different scaffold geometries were investigated: a scaffold composed of three vertical struts (Figure 6C); and a grid-like scaffold (Figure 6E).

It was assumed that the scaffold material would have a porosity (P) of 50%. Therefore, the elastic modulus of the scaffold struts (E_{Struts}) at the first iteration of the model was calculated as the weighted average of the elastic modulus of scaffold material ($E_{Scaffold}$) and granulation tissue (E_{Gran}), as indicated by Equation 8:

$$E_{Struts} = \frac{1}{100}\left[P \cdot E_{Gran} + (100 - P) \cdot E_{Scaffold}\right] \quad \text{Equation 8}$$

Poisson's ratio, permeability and bulk modulus of grain of scaffold struts were similarly calculated. The material properties at subsequent iterations were calculated as later described.

Three $E_{Scaffold}$ of 0.1, 10, and 1000 MPa were tested for the three vertical struts scaffold. Moreover, a biphasic scaffold with elastic modulus of 1000 MPa and 10 MPa in the proximal and distal halves, respectively, was studied (Figure 6D). The grid-like scaffold had an $E_{Scaffold}$ of 1000 MPa. All other material properties of the scaffolds were kept constant as follows: permeability of 3.63×10^{-8} mm/s, void ratio of 4, bulk modulus of grain of 0 MPa, and Poisson's ratio of 0.3.

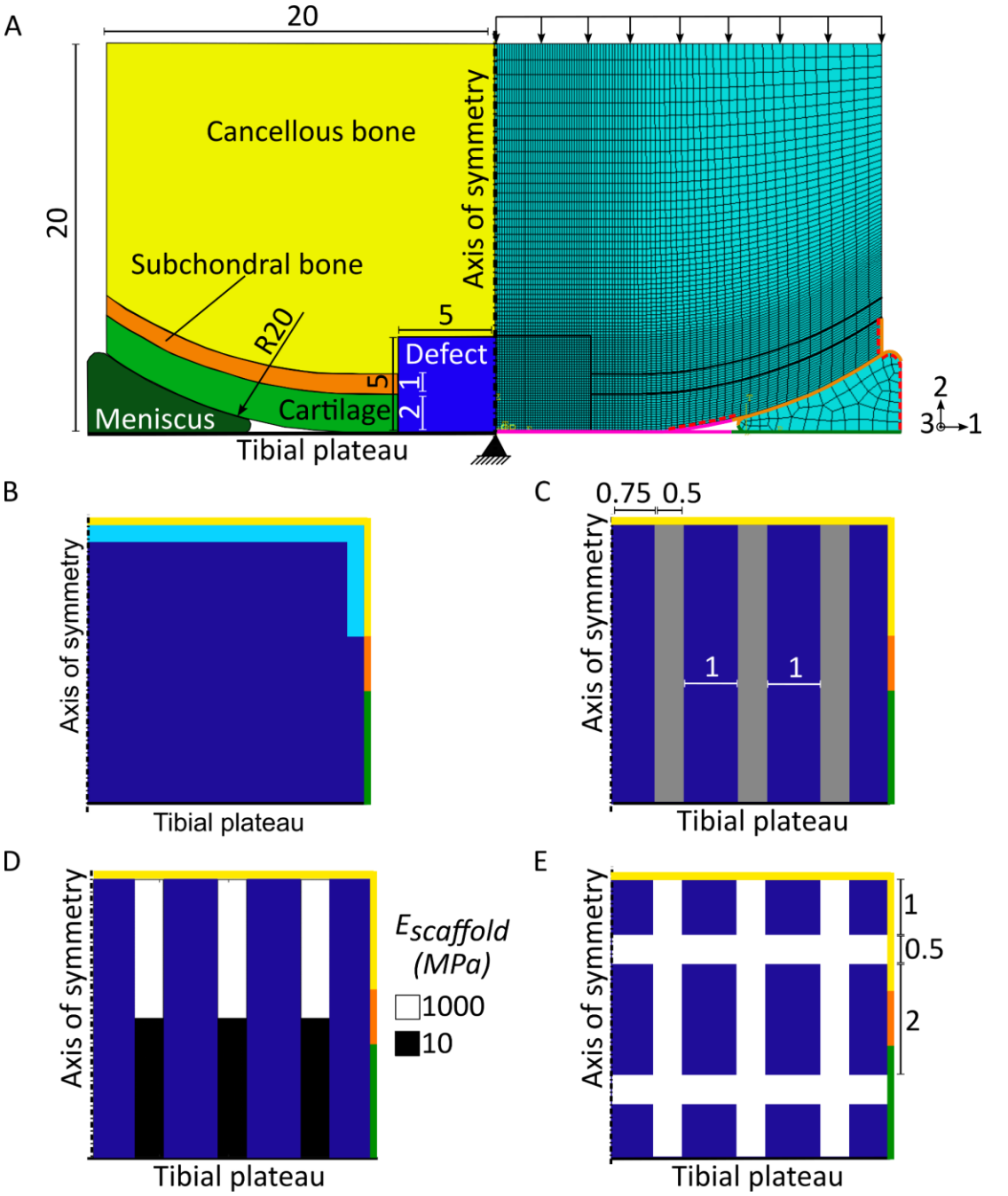

Figure 6: Computational model of osteochondral defect. A) Representation of the axisymmetric FE model of femoral condyle showing tissues (left) and mesh (right). The surfaces of the femoral condyle-tibia, femoral condyle-meniscus, and meniscus-tibia interactions are highlighted in magenta, orange, and green, respectively. The black triangle and the black arrows indicate the clamp boundary condition and the applied pressure, respectively. The free cartilage edges are marked by the red dashed lines. The 1, 2, and 3 axes in the coordinate system correspond to the radial, axial, and circumferential directions, respectively; B), C), D), and E) details of the osteochondral defect showing the MSCs-filled elements (cyan) at day 1, the vertical strut scaffold, the biphasic scaffold, and the grid-like scaffold, respectively. The blue areas correspond to the distribution of granulation tissue at day 1. The colors of the borders code for the neighboring tissues: yellow, orange, and green stand for cancellous bone, subchondral bone, and cartilage. Black dash-dot lines and black solid lines always indicate the axis of symmetry and the tibial plateau, respectively. All values are in mm if not specifically stated otherwise. Images A), C)-E) were reproduced from [75] under CC BY 4.0 [65].

2.3.2 Model of cellular behavior

Cellular behavior in the defect was modelled in Matlab (MathWorks). The defect was represented by a 40 x 40 elements matrix, in which each element corresponded to the element in the same position in the FE mesh. A maximum number of N_{MAX} = 100 cells/element was allowed. When a scaffold was implemented, elements belonging to scaffold struts could be populated by cells due to the material porosity, but they could host a maximum of $N_{MAX}^{Struts} = N_{MAX} * P$ cells. Four cell phenotypes were modelled: MSCs, osteoblasts, chondrocytes, and fibroblasts. Four cellular activities were simulated: MSCs differentiation, MSCs migration, mitosis, and apoptosis.

Cellular mitosis/apoptosis and MSCs differentiation were considered to be mechanics-dependent, as previously suggested elsewhere [74]. Based on the results of the FE analysis of the femoral condyle, a mechanics-dependent stimulus (*S*) was calculated as indicated by Equation 9:

$$S = \frac{\gamma}{a} + \frac{v}{b} \qquad \text{Equation 9}$$

Where γ was the octahedral shear stain, *v* was the fluid velocity, and *a* = 3.75% and *b* = 3 × 10^{-3} mm/s were empirically derived constants [60]. The mechanics-dependent cellular behavior was described by defining thresholds of *S*, as indicated in Table 5.

Table 5: Thresholds of *S* describing the mechanics-dependent cellular behavior [60].

$0 \leq S < 0.01$	**$0.01 \leq S < 1$**	**$1 \leq S < 3$**	**$S \geq 3$**
Bone resorption	Bone formation	Cartilage formation	Fibrous tissue formation

MSCs differentiation was modelled by transforming 5% of the MSCs in a specific element into the cell phenotype corresponding to the tissue whose formation was favored by the *S* value in the element. Bone resorption was modelled by a 10% reduction in the number of osteoblasts in regions where the mechanical stimulus was not favorable to bone formation.

MSCs mitosis was independent of *S* and had a constant 15% rate. Mitosis and apoptosis of the other cell phenotypes were *S*-dependent. If an element was subjected to an *S* value fostering the formation of a specific tissue, cells of the corresponding phenotype would increase of 5% in number, while all other cell phenotypes would reduce their number of 15%.

MSCs migration was independent of *S* and modelled as a passive diffusion process. Each element had a diffusion coefficient (*DC*) calculated as the weighted average of the coefficients of the tissues (Table 6) that were found in the element, as indicated by Equation 10:

$$DC = \frac{1}{N_{MAX}}\left[\left(N_{MAX} - \sum_{k=1}^{n_t} N_k\right) \cdot DC_{Gran} + \sum_{k=1}^{n_t} DC_k \cdot N_k\right] \qquad \text{Equation 10}$$

Where n_t was the number of species and N was the space fraction occupied by the cells of a specific phenotype or by the scaffold (when implemented), which had the property indicated by Equation 11:

$$\frac{1}{N_{MAX}}\sum_{k=1}^{n_t} N_k = 1 \qquad \text{Equation 11}$$

For the empty osteochondral defect, n_t was equal to 4, corresponding to granulation tissue, cartilage, fibrous tissue, and bone; when a scaffold was implemented, n_t was equal to 5. Space not yet populated by cells or occupied by MSCs was assigned the properties of granulation tissue.

Table 6: Diffusion coefficients of tissues [60] and scaffold.

Tissue	**Abbreviation**	**Diffusion coefficient (mm²/day)**
Granulation	DC_{Gran}	0.80
Cartilage	DC_{Cart}	0.05
Fibrous	DC_{Fibro}	0.10
Bone	DC_{Bone}	0.01
Scaffold	$DC_{Scaffold}$	0.01

An FE model was built in Abaqus to calculate MSCs diffusion. The model represented only the defect, which was meshed with 1600 elements type DC2D4. Each element was assigned a diffusivity value as calculated with Equation 10. The MSCs content of each element was set as initial condition.

Tissues were assumed to be produced by the cells of the corresponding phenotypes proportionally to their number. Therefore, material properties in the defect were updated consequently to the calculations of cellular activities. Elastic modulus, Poisson's ratio, permeability, and bulk modulus of grain of each element were calculated as the weighted averages of the tissues found in them, as indicated by Equation 10. Specifically, tissue properties of cancellous bone, poroelastic cartilage, and fibrous tissue (see Table 4) were assigned to the space fraction occupied by osteoblasts, chondrocytes, and fibroblasts, respectively. Space fractions empty of cells or populated by MSCs were assigned the tissue properties of granulation tissue.

The updated material properties of the defect were implemented in a new FE analysis of the femoral condyle model. The process was iteratively repeated until healing of the osteochondral defect, which was reached at iteration 50. In this model, one iteration was defined as the FE analysis of the knee femoral condyle plus the calculation of the

corresponding cellular activities. One iteration roughly corresponded to one day of the *in vivo* healing process.

At day 0, the defect was empty of cells, with the exception of the elements neighboring the cancellous bone, which were filled with MSCs (Figure 6B). This setup modelled the experimental observation that the progenitor cells involved in the healing of osteochondral defects derive from the bone marrow [76]. Every day, these same elements were replenished with MSCs, simulating a continuous cell supply from the medullar niche.

3 Results

3.1 Selection of design for the support structures

A first screening of possible support structure architectures was performed by building a CAD library with 51 possible designs having the same basic shape, i.e. a hollow hexagonal cylinder, and different strut configurations (Figure 7). Each design was tested in compression by means of a FE analysis based on the CAD, from which the computational architecture-dependent stiffness (k_C) of the design was evaluated. The designs were simplified as uniform materials and their computational elastic properties, modelled as moduli (E_C), were calculated from k_C. Within the CAD library, E_C ranged from as low as 37 MPa to as high as 343 MPa. Moreover, the porosity (P) of each design was calculated, with results spanning from 72% to 85%.

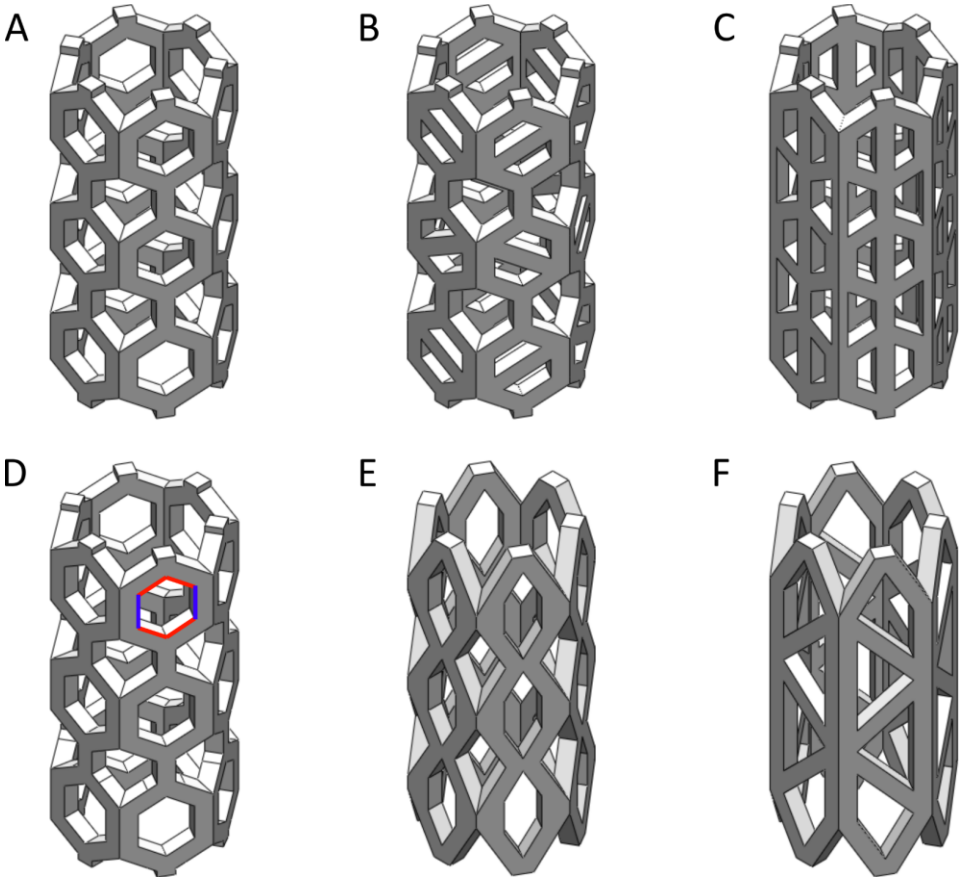

Figure 7: Examples of designs from the CAD library. A) Pore pattern of equilateral hexagons; B) pore pattern of equilateral hexagons with diagonal reinforces; C) pore pattern of equilateral hexagons with vertical reinforces; D) pore pattern of non-equilateral hexagons. The sides of different lengths are highlighted in red and blue; E) pore pattern of hexagons with 60° angles; F) pore pattern of irregular shapes.

From the CAD library, seven designs, which were named CAD1 to CAD7, were chosen to be produced by selective laser sintering (SLS) from polyamide (PA). Selection criteria were based on a porosity higher than 80% and stiffness values going from low to high,

sampling the wide range of calculated E_C. Prior to production, the seven designs were adapted in view of the subsequent mechanical testing by the introduction of hexagonal rings on the top and bottom surfaces, whose aim was the even distribution of axial compressive loads to the structure (Figure 8A). P and E_C were re-evaluated for the adapted designs, observing minor reductions in porosity (Table 7). Nonetheless, all designs maintained high porosities (≥77%). The strain distribution resulting from FE analyses at 3% compression showed that the vertical elements of the architectures were subjected to compressive strains of approximately 10%, while the oblique elements were almost unstrained (Figure 8C). Peaks of compressive strain up to 40% were measured locally at the sharp corners of the architectures.

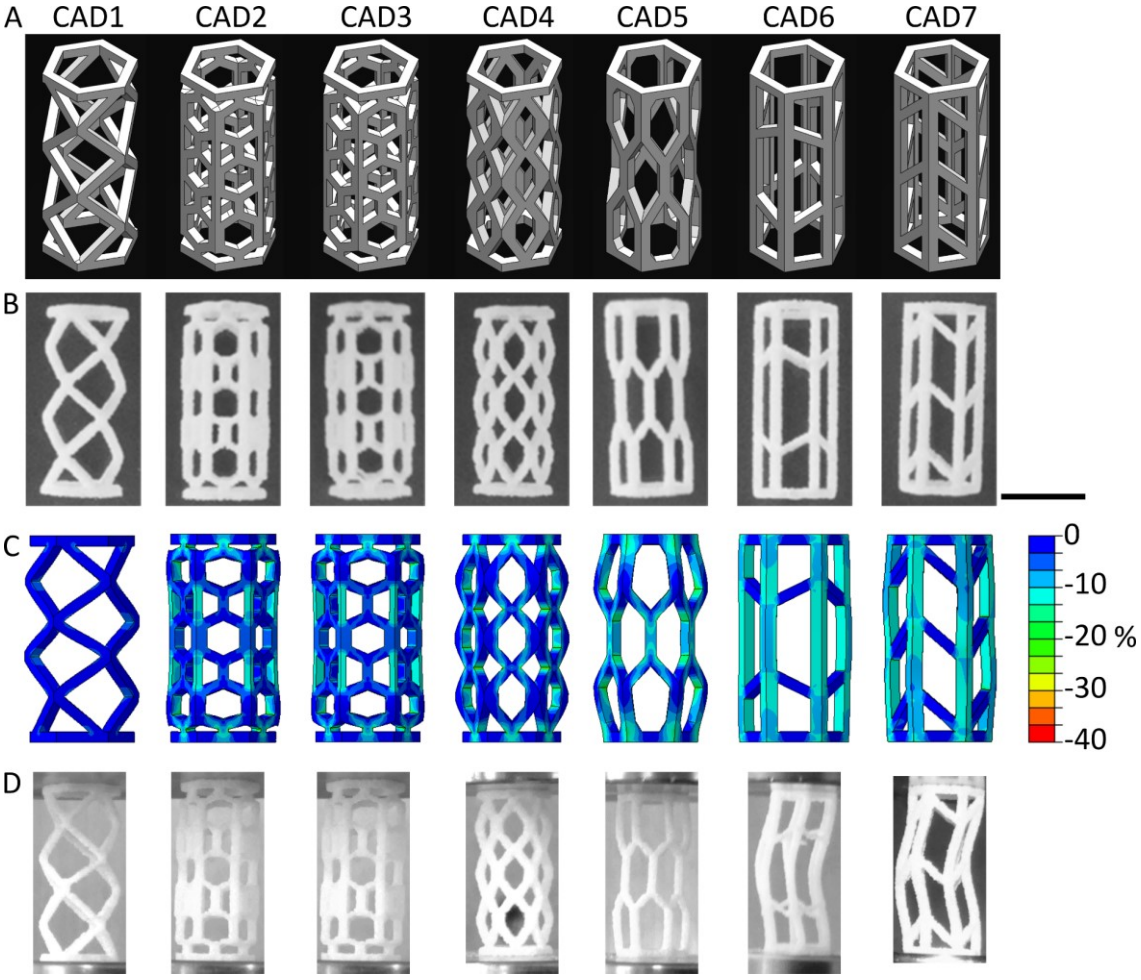

Figure 8: Preliminary study for the selection of architectures for the stiff and compliant support structures. A) CADs that were chosen for production, called CAD1 to CAD7; B) pictures of CAD1 to CAD7 after production by SLS from PA. The scale bar is 5 mm; C) distribution of the minimum principal strain in CAD1 to CAD7 resulting from CAD-based FE analyses at 3% compression; D) pictures of CAD1 to CAD7 at 3% compression during mechanical testing.

All selected designs were successfully produced by SLS from PA (Figure 8B) and their stiffness (k) was measured by means of monoaxial compression tests. Each design was simplified as a uniform material, whose elastic modulus (E) was calculated from k (Table

7). For all investigated designs, E was lower than E_C, going from a minimum of 0.8% of the simulated value for CAD1 to a maximum of 3.0% for CAD6 and CAD7.

Table 7: Mechanical and morphological properties of the preliminary design produced by SLS from PA. P: porosity; E_C: computational elastic modulus; E: experimental elastic modulus.

Design	***P* %**	***E*$_C$ (MPa)**	***E* (MPa)**	***E* as % of *E*$_C$**
CAD1	85	34	0.26 ± 0.04	0.8%
CAD2	78	408	7.30 ± 0.53	1.8%
CAD3	78	438	8.06 ± 0.29	1.8%
CAD4	77	456	4.95 ± 1.15	1.1%
CAD5	82	548	6.40 ± 0.87	1.2%
CAD6	81	775	23.19 ± 0.60	3.0%
CAD7	79	803	24.23 ± 3.11	3.0%

Structures with struts oriented predominantly in the axial direction, such as CAD6 and CAD7, resulted in the highest E, but showed signs of buckling already at 3% compression (Figure 8D). CAD2, CAD3, and CAD5 had non-uniform strain distributions, in some cases with formation of cracks (Figure 8D), while CAD1 and CAD4 resulted in uniform deformations without observable crack nucleation. Thus, CAD1 and CAD4 were selected as preliminary architectures of compliant and stiff support structures, respectively.

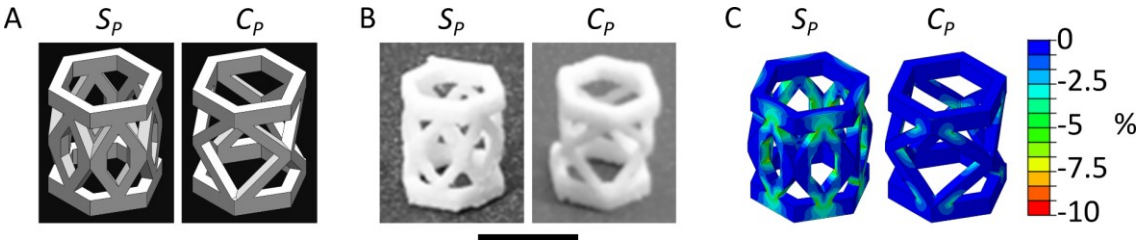

Figure 9: Preliminary stiff and compliant support structures. A), B), and C) CADs, pictures, and distributions of minimum principal strain, respectively, of preliminary stiff (S_P) and compliant (C_P) support structures. The scale bar is 5 mm.

For a better handling during the subsequent *in vitro* experiments, CAD1 and CAD4 were adapted in size by reducing their height from 11 to 5.33 mm, generating the C_P and S_P architectures, respectively (Figure 9A). FE analyses in compression revealed that strain distributions in S_P and C_P were similar to the ones observed in CAD4 and CAD1, respectively (Figure 9C). However, the peaks of compressive strains in the sharp corners reached a lower value of 10%. S_P and C_P were produced by SLS from PA (Figure 9B) and tested in compression in wet environment, measuring E values of 13.0 ± 0.9 MPa and 1.8 ± 0.2 MPa, respectively.

3.2 Influence of PCL powder properties on the sintering process

The preliminary stiff support structure architecture S_P was employed as reference architecture during the set up of the SLS process with PCL as substrate. Such establishment begun by selecting the material to be employed for support structure production amongst the following three PCL powders: nominal number average molecular weight ($\overline{M}_n$) of 60,000 g/mol and size of 25–50 µm; nominal $\overline{M}_n$ of 100,000 g/mol and size of 25–50 µm; nominal $\overline{M}_n$ of 60,000 g/mol and size of 50–80 µm. S_P was produced by SLS from each of the three PCL powders and the *E* of the resulting support structures, again simplified as uniform materials, was measured by means of monoaxial compression tests.

The PCL powder with the highest nominal $\overline{M}_n$ of 100,000 g/mol and size of 25–50 µm resulted in the S_P with the lowest compressive *E* of 5.6 ± 1.2 MPa (Figure 10A). The two PCL powders with nominal $\overline{M}_n$ of 60,000 g/mol and size of either 25–50 µm or 50–80 µm yielded S_P with comparable *E* of 11.3 ± 0.5 MPa and 11.0 ± 0.8 MPa, respectively (Figure 10A).

During the SLS process, the three investigated PCL powders behaved differently depending on their size, but independently of their nominal $\overline{M}_n$. In fact, particles with size of 50–80 µm were evenly spread in the building chamber by a roller equipped with an ionizer (Figure 10B). On the contrary, particles with size of 25–50 µm formed aggregates that were randomly dropped onto the building chamber (Figure 10C).

Based on the better powder behavior and the comparatively high *E* of the resulting S_P support structures, the PCL powder with nominal $\overline{M}_n$ of 60,000 g/mol and size of 50–80 µm was selected for the production of the support structures in all subsequent experiments.

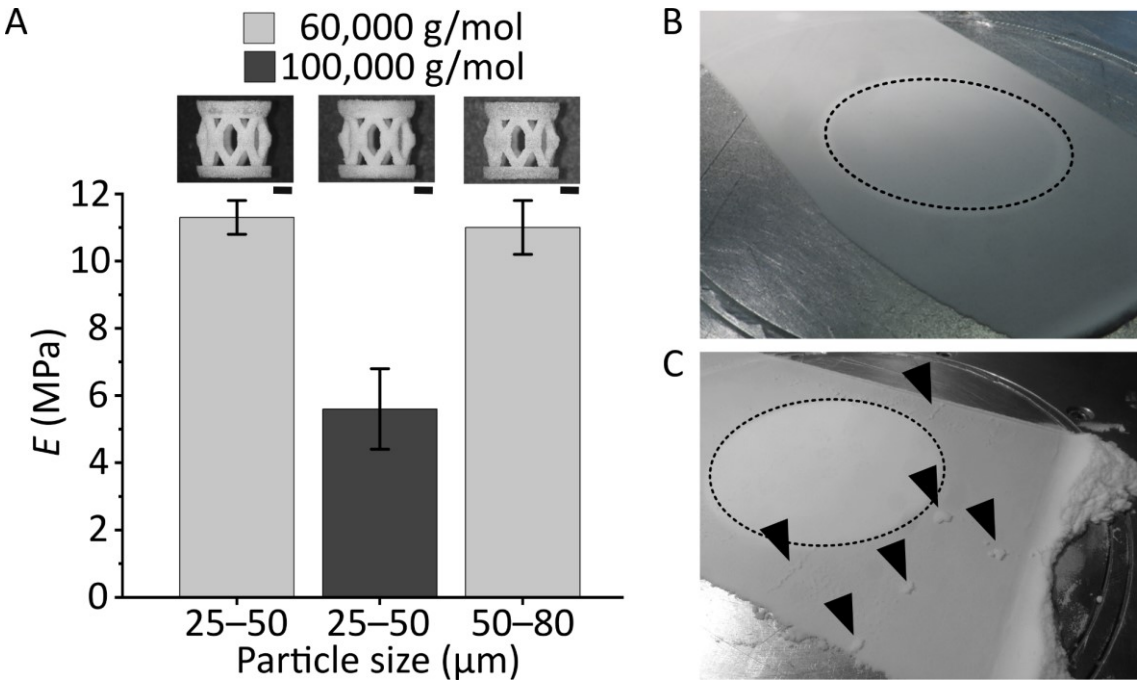

Figure 10: Influence of PCL particles on the SLS process. A) Elastic modulus of preliminary stiff (S_P) support structures produced with the investigated PCL particles. Inserts show the support structures produced from each particle type. Scale bars are 1200 µm; B) and C) powder deposition in the building chamber with PCL particles having size of 50–80 and 25–50 µm, respectively. The dashed circles mark the building chamber (diameter 70 mm). The black arrows point at powder aggregates. Adapted from [77] with right as author.

3.3 Influence of the sterilization method on support structure properties

Two sterilization methods, i.e. ethylene oxide (EtOx) and gamma irradiation, were tested on S_P structures and their influence on the mechanical and material properties of the support structures was evaluated by measuring the resulting E and $\overline{M}_n$ and by comparing it to unsterile structures. The $\overline{M}_n$ of the unsintered PCL powder was also measured as reference. Also in this case, the support structures were simplified as uniform materials in the mechanical evaluation.

Unsterile S_P structures had E of 20.9 ± 1.9 MPa (Table 8). The EtOx- and gamma-sterilized structures had a comparable E of 18.6 ± 3.0 MPa and 18.1 ± 1.2 MPa, respectively (Table 8).

The molecular weight measurement revealed that unsintered PCL powder, unsterile S_P, and EtOx-sterilized S_P had similar $\overline{M}_n$, with values of 57,600 g/mol, 55,000 g/mol, and 57,700 g/mol, respectively, and equal dispersity indexes of 1.8 (Table 8). On the contrary, gamma-sterilized S_P had a lower $\overline{M}_n$ of 37,700 g/mol and a higher dispersity index of 2.2 (Table 8).

Considering the absence of negative influences on both mechanical and material properties, EtOx was considered as a suitable sterilization method for the PCL support structures.

Table 8: Influence of the sterilization method on the material and mechanical properties of preliminary stiff (S_P) support structures. $\bar{M}_n$: number average molecular weight; *DI*: dispersity index; *E*: elastic modulus.

Sample	$\bar{M}_n$ **(g/mol)**	***DI***	***E* (MPa)**
PCL powder	57,600	1.8	-
S_P **– unsterile**	55,000	1.8	20.9 ± 1.9
S_P **– EtOx**	57,700	1.8	18.1 ± 1.2
S_P **– gamma**	37,700	2.2	18.6 ± 3.0

3.4 Influence of SLS process parameters on support structure morphological and mechanical properties

The ideal SLS process parameters to produce PCL support structures with accurate reproduction of the original CAD and with the highest possible SLS-dependent mechanical competence were sought by producing S_P structures with systematic variations of laser power (P_L), laser beam compensation (*BC*) and laser beam diameter (*BD*) (Table 2). The influence of the different sets of SLS process parameters on the mechanical and morphological properties of S_P support structures, simplified as uniform materials for the mechanical characterization, was evaluated by measuring their compressive *E* and strut diameter (D_S), respectively.

Results showed that, depending on the set of SLS process parameters, the same S_P design could have *E* ranging from as low as 1.76 ± 0.05 MPa to as high as 36.06 ± 3.24 MPa (Figure 12A). Similarly, D_S spanned from minimum values of 409 ± 30 µm to maximum values of 772 ± 7 µm (Figure 11), although the strut diameter of the S_P design was invariably 500 µm.

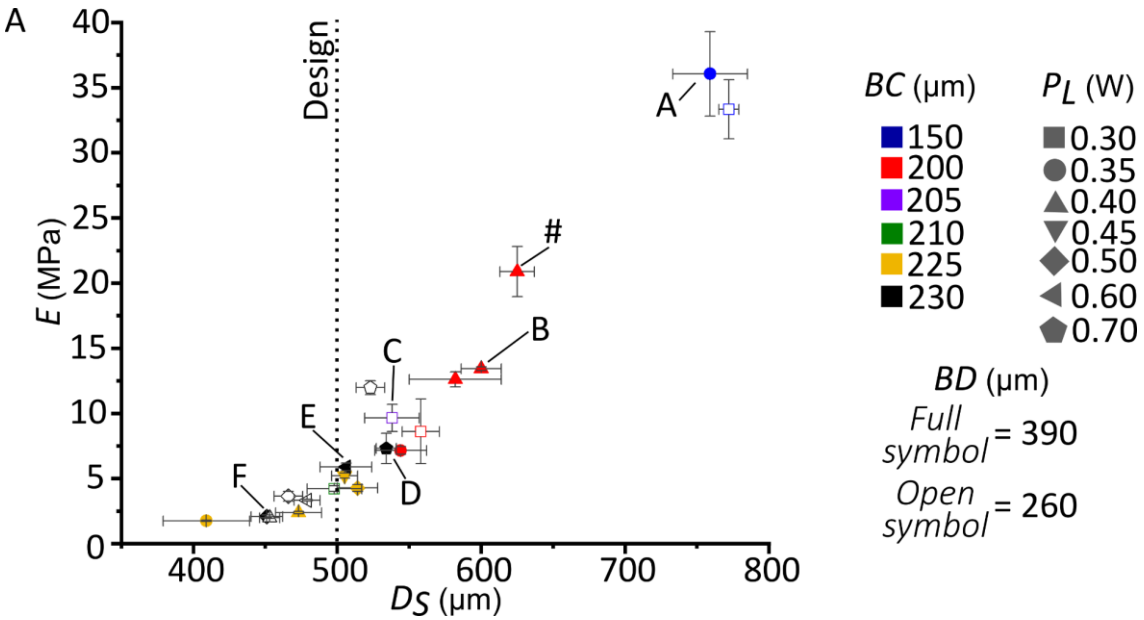

Figure 11: Elastic modulus (E) of preliminary stiff support structure (S_P) in dependency of the strut diameter (D_S) resulting from different sets of SLS process parameters. Colors, shapes, and full/open symbols indicate different laser beam compensation (BC), laser power (P_L) and laser beam diameter (BD), respectively. The dotted line shows the design strut diameter. Prototypes "A" to "F" are marked in the plot and were further analysed. The # symbol marks the support structures used as unsterile control in the sterilization test. For each set of SLS process parameters, at least n = 3 samples were tested. Results are given as average ± standard deviation. Adapted from [77] with right as author.

A general trend was observed, in which similar mechanical properties were measured in S_P structures produced with different sets of SLS process parameters as long as the resulting D_S were comparable. In some cases, however, structures with same D_S resulted in different E (see "C" and "D" in Figure 11). This observation prompted a more in depth morphological analysis, which was performed on six selected support structures, named prototypes "A" to "F" (Figure 12B). These six prototypes were all produced with different sets of SLS process parameters and covered well the broad ranges of E and D_S that had been measured (Table 9). The six prototypes were cut to ¾ of their height (Figure 12A) and the cross section of their struts was evaluated by scanning electron microscopy (SEM) and subsequent measurement of the molten cross-sectional area (A_M) (Figure 12C). Although all prototypes were produced from the same CAD with strut cross section of 0.39 mm^2 (highlighted in Figure 12A), the measured A_M ranged from a minimum of 0.01 ± 0.009 mm^2 for prototype "F" to a maximum of 0.32 ± 0.03 mm^2 for prototype "A" (Table 9). The diameter of the molten cross-section (D_M) was calculated from A_M, resulting in minimum and maximum values of 129 ± 11 µm and 639 ± 30 µm for prototypes "F" and "A", respectively (Table 9).

Table 9: SLS process parameters and measured properties of prototypes "A" to "F": laser power (P_L), laser beam compensation (*BC*), laser beam diameter (*BD*), elastic modulus (*E*), strut diameter (D_S), molten cross-sectional area (A_M), and molten diameter (D_M).

	Prototype A	**Prototype B**	**Prototype C**	**Prototype D**	**Prototype E**	**Prototype F**
***P_L* (W)**	0.35	0.40	0.30	0.70	0.60	0.40
***BC* (µm)**	150	200	205	230	230	230
***BD* (µm)**	390	260	390	390	390	260
***E* (MPa)**	36.1 ± 3.2	13.4 ± 0.1	9.7 ± 1.0	7.3 ± 1.2	5.9 ± 0.3	2.0 ± 0.1
***D_S* (µm)**	759 ± 26	600 ± 14	538 ± 19	534 ± 7	506 ± 18	453 ± 7
***A_M* (mm^2)**	0.32 ± 0.03	0.14 ± 0.02	0.13 ± 0.01	0.08 ± 0.02	0.05 ± 0.02	0.01 ± 0.009
***D_M* (µm)**	639 ± 30	425 ± 21	401 ± 16	317 ± 20	260 ± 28	129 ± 11

The theoretical dependency of the elastic modulus on the strut diameter of the S_P support structure was studied by performing FE analyses in compression based on six CADs having the same architecture of S_P, but computational strut diameter (D_C) of 310, 400, 500, 600, 700, and 800 µm. In the computational setting, D_M and D_S coincided. The theoretical relationship between the computational elastic modulus (E_C) and D_C was found to be the quadratic polynomial in Equation 12:

$$E_C = 7.2 \cdot 10^{-5} \cdot D_C^2 \qquad \text{Equation 12}$$

The theoretical relationship expressed by Equation 12 well described the experimentally observed relationship between *E* and D_M with the additional introduction of a factor *K*, which compensated for the unknown material elastic modulus in the computational evaluation, as indicated by Equation 13 (solid black line in Figure 12D):

$$\begin{cases} E = K \cdot 7.2 \cdot 10^{-5} \cdot D_M^2 \\ K = 1.05 \end{cases} \qquad \text{Equation 13}$$

On the contrary, the experimental relationship between *E* and D_S could not be described by the theoretical Equation 12 and was, instead, expressed by the quadratic polynomial in Equation 14 (solid red line in Figure 12D):

$$E = -2.6 - 4.1 \cdot 10^{-2} \cdot D_S + 1.1 \cdot 10^{-4} \cdot D_S^2 \qquad \text{Equation 14}$$

The ratio D_M/D_S was calculated and expressed as a function of D_M, including six extrapolated data points to show the behavior of the data at high D_M values (Figure 12E). The extrapolation of data points was performed by observing that Equation 13 and Equation 14 had an approximately constant distance of 100 µm above a threshold

diameter value of 600 µm (Figure 12D). The resulting data set was described by Equation 15 (solid black line in Figure 12E):

$$\frac{D_M}{D_S} = \frac{D_M}{D_M+100} - \frac{0.165}{1+9.7\cdot10^{-9}\cdot D_M^3} \qquad \text{Equation 15}$$

At high values of D_M, Equation 15 showed an asymptotic behavior towards the ideal D_M/D_S value of 1, while below a threshold defined at D_M = 550 µm, the ratio became disproportionally small, with unfavorable effects on the mechanical competence of the support structures.

Based on these results, the support structure design was modified in such a way as to have improved SLS-derived mechanical properties by means of an increase in strut diameter.

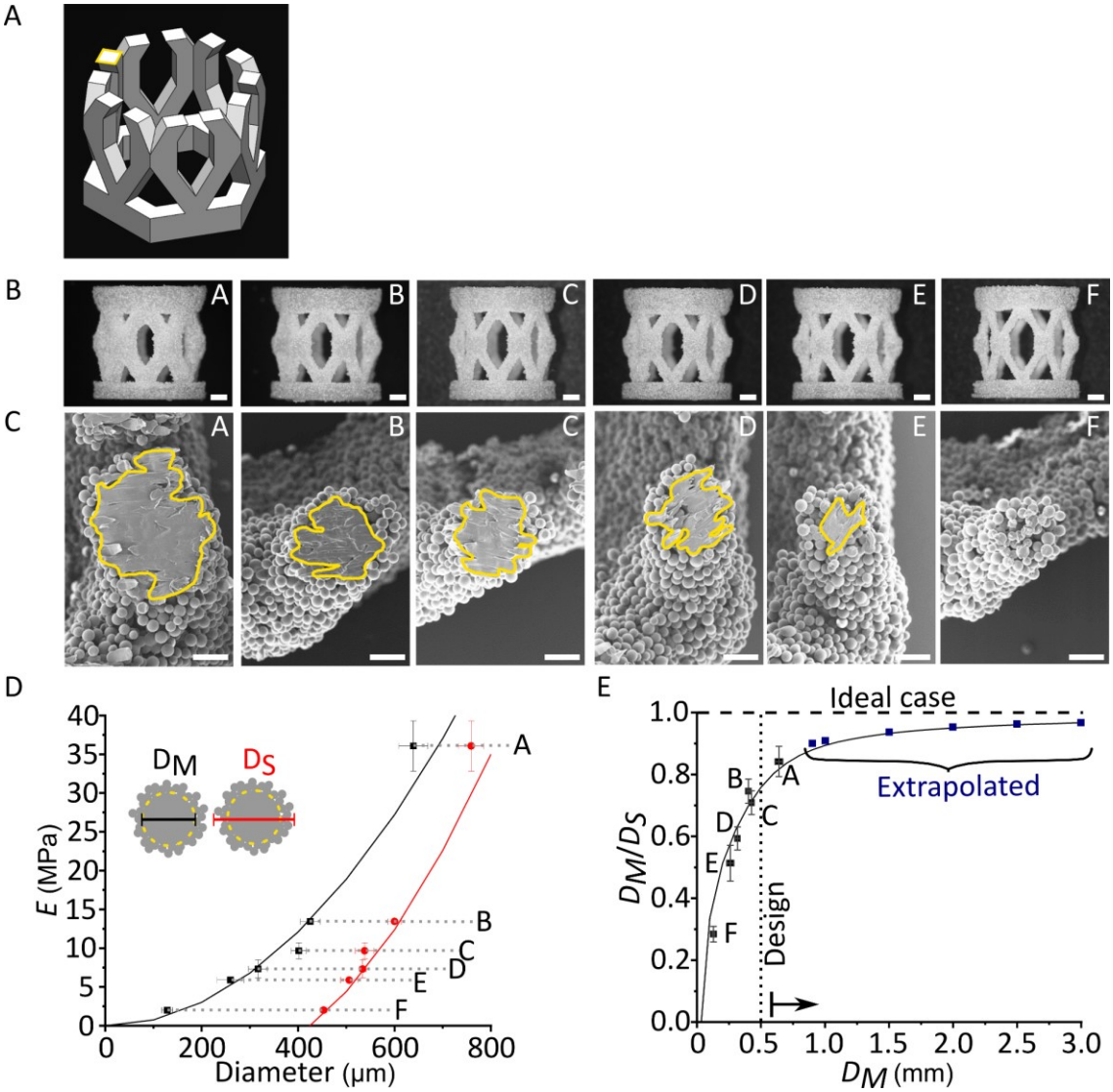

Figure 12: Influence of SLS process parameters on mechanical and morphological properties of preliminary stiff support structure (S_P). A) Schematic representation of S_P cut for cross-section evaluation. The design molten cross-sectional area (A_M) is highlighted in yellow; B) pictures of the prototypes selected for morphological analysis. Scale bars are 800 µm; C) representative SEM images of strut cross-section of the selected prototypes. The yellow lines mark A_M. Scale bars are 200 µm. For each prototype, 12 struts were measured; D) comparison of E in dependency of strut diameter (D_S) and molten diameter (D_M) of the selected prototypes; E) D_M/D_S ratio in dependency of D_M. Six data points were extrapolated and are marked in blue. The dotted and dashed lines indicate the design D_M and the ideal D_M/D_S ratio, respectively. The arrow shows the minimum favorable D_M. Results are given as average ± standard deviation. A), B), D), and E) adapted from [77] with right as author.

3.5 Cytocompatibility of PCL support structures

The cytocompatibility of sintered PCL was tested by *in vitro* cell culture of MSCs exposed to expansion medium conditioned with the prototypes “A” to “F” (Table 9). At three experimental time points (day 0, 3, and 6), cellular metabolic activity and proliferation were measured.

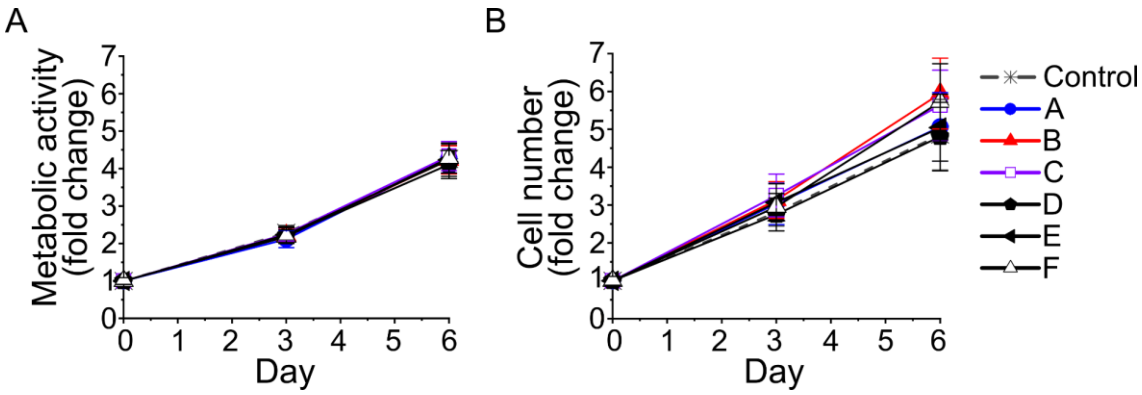

Figure 13: Cytocompatibility of PCL support structures with preliminary stiff design (S_P). MSCs were exposed to medium conditioned with prototypes "A" to "F". Cell cultured in 10% expansion medium were used as control. A) Cellular metabolic activity; B) cell number. Data were obtained in n = 4 independent experiments. Results were normalized to day 0 and are reported as average fold change ± standard deviation.

Results showed that the behavior of MSCs exposed to conditioned medium of all prototypes was consistent with the behavior of the control MSCs in both metabolic activity (Figure 13A) and cell proliferation (Figure 13B). In fact, metabolic activity increased 2.2 folds at day 3 and 4.2 folds at day 6 for all tested conditions (Figure 13A). Moreover, cell number increased of approximately 3 folds at day 3 (Figure 13B). Data were more scattered at day 6, with a minimum and maximum cell number increase of 4.8 ± 0.9 folds for prototype "D" and 5.9 ± 0.9 folds for prototype "B", respectively. Nonetheless, the behavior of all tested conditions was consistent with the control, whose cell number showed an increase of 4.9 ± 0.9 folds at day 6.

3.6 Design improvement of support structure

The design of the stiff support structure S_P, having a strut diameter of 500 µm and a porosity of 77.2%, was improved by combining experimental observations with a topology optimization approach.

First, the S_P design was given in input to a topology optimization software with objective function set to strain minimization, i.e. stiffness maximization. The material on the side of the pore on each face of the design was identified as non-contributing to the load bearing ability of the support structure. Thus, it was removed from its original location and redistributed on the struts, increasing the strut diameter.

Then, the sharp edges of the design were smoothened, as the sharp corners of the pores were identified as crack nucleation points during the experimental compression tests. The material was again redistributed to increase the strut diameter. By means of this redistribution process, it was possible to increase the strut diameter from 500 µm to 540 µm, while at the same time maintaining an unaltered high porosity of 77%.

Finally, the size of the support structure was adapted to the size of the rat large bone defect in the *in vivo* model, resulting in the stiff S_H design with height of 5.20 mm and

maximum width of 4.33 mm (Figure 14A left). The strut diameter and porosity of the S_H design were 540 µm and 71.1%, respectively. The knowledge acquired during the improvement of the stiff support structure design was applied to the compliant support structure, generating the C_H design with height of 5.20 mm, maximum width of 4.33 mm, strut diameter of 540 µm, porosity of 78.4%, and smooth edges (Figure 14A right). The mechanical characterization of S_H and C_H resulted in a significantly different stiffness (k) of 33.8 ± 0.3 N/mm and 4.3 ± 0.3 N/mm, respectively (Figure 14C).

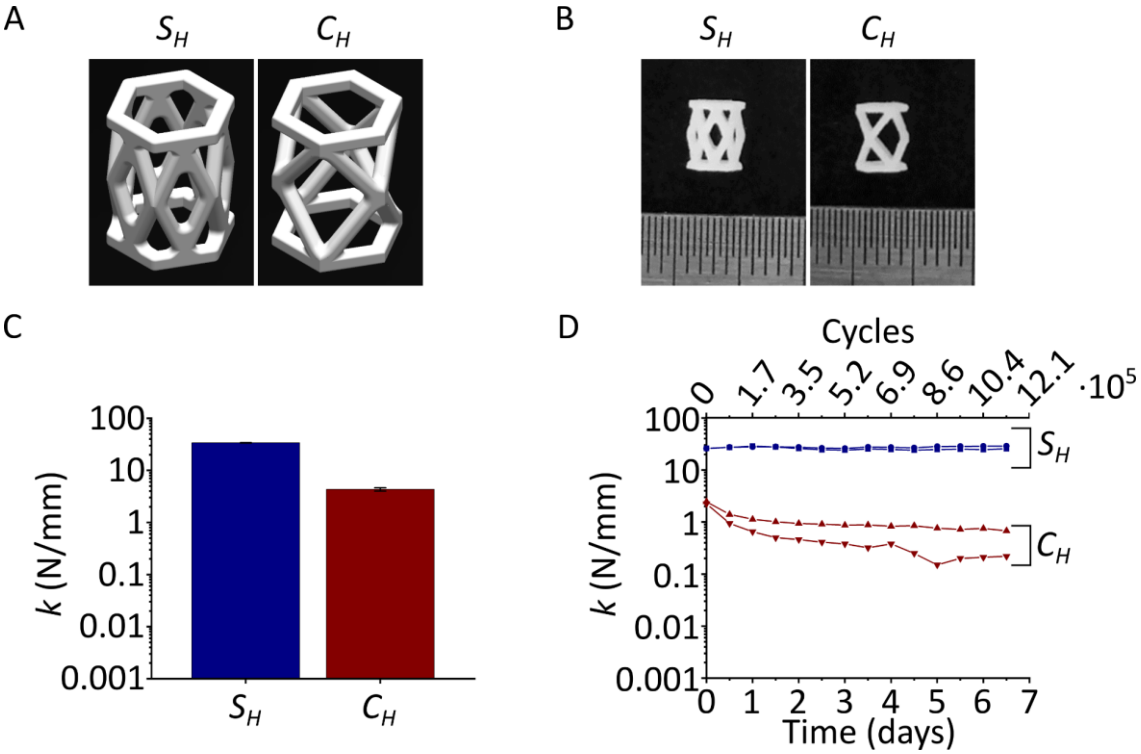

Figure 14: Stiff and compliant support structures with hexagonal cross-section (S_H and C_H, respectively). A) CADs; B) pictures of stiff and compliant support structures produced by SLS from PCL; C) stiffness (k) of stiff and compliant support structures (n = 3). Results are given as average ± standard deviation; D) fatigue resistance of stiff and compliant support structures (n = 2).

The fatigue resistance of the S_H and C_H support structures was tested by cyclic compression tests in *in vivo*-like conditions performed in a bioreactor. The support structures underwent 1,209,600 compressive cycles over a period of 1 week. Preliminary experiments revealed a failure in C_H after less than 1 day of mechanical stimulation (Figure 14D), i.e. after less than 172,800 compression cycles. The reason for the early failures was identified in the large lateral displacement happening at the corners of the hexagonal cross-section of the C_H support structure. Although S_H support structures were stable for the whole duration of the dynamic experiment (Figure 14D), they were equally subjected to a large lateral displacement at the corners of the hexagonal cross-section. Therefore, both the stiff and the compliant support structures were re-designed to have a circular cross-section with the aim of reducing the lateral displacement and thereby improving the stability in dynamic loading conditions. The

stiff and compliant support structures of type S_C and C_C, respectively, were so designed (Figure 15A).

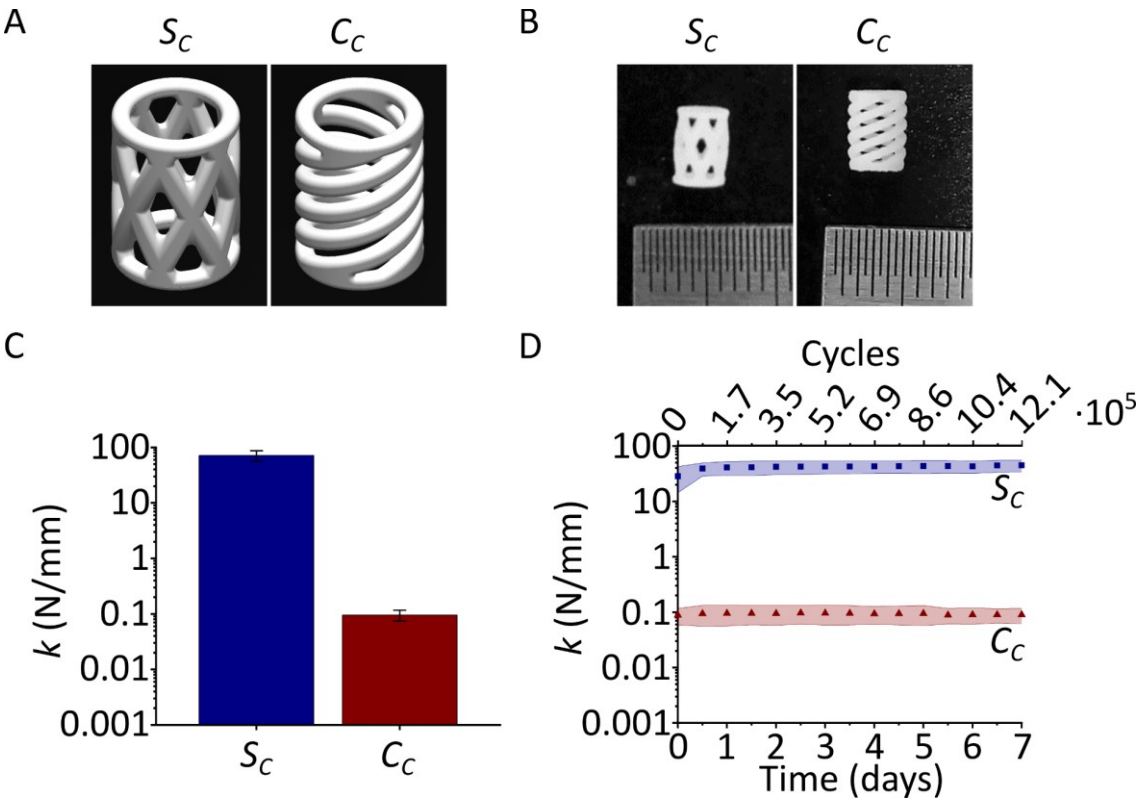

Figure 15: Stiff and compliant support structures with circular cross-section (S_C and C_C, respectively). A) CADs; B) pictures of stiff and compliant support structures produced by SLS from PCL; C) stiffness (k) of stiff (n = 19) and compliant (n = 6) support structures; D) fatigue resistance of stiff and compliant support structures (n = 8). Results are given as average ± standard deviation.

Both S_C and C_C had a strut diameter of 540 µm and a similar porosity of 66.6% and 68.6%, respectively. The stiff support structure S_C had a k of 71.7 ± 15.3 N/mm (Figure 15C). The compliant support structure C_C had a k of 0.10 ± 0.02 N/mm (Figure 15C). During the fatigue resistance test, both S_C and C_C were stable over 1,209,600 compressive cycles in *in vivo*-like conditions (Figure 15D).

3.7 Analysis of collagen scaffold pore morphology in hybrid scaffolds

Multiscale hybrid scaffolds were produced by including the circular stiff and compliant support structures (S_C and C_C, respectively) into a collagen scaffold produced from a 1.5 wt-% collagen dispersion (Figure 16A). To evaluate the retention of the aligned collagen architecture typical of the collagen scaffolds, the collagen walls of the scaffolds were visualized by combining second harmonic (SH) imaging, which showed fibrillar collagen type I, to confocal images of an anti-fibronectin fluorescent staining, which showed the fibronectin that was previously let adsorb on the walls (Figure 16B, C, and D). Then, the images were used for an orientation analysis.

Results showed that the collagen scaffolds had walls predominantly aligned in the axial direction (Figure 16E), having a peak in the axial direction (90°) with normalized value of 0.017 ± 0.003, which was 21 ± 6 folds higher than the one in the transversal direction (0° and 180°). Stiff and compliant hybrid scaffolds had a similar material alignment (Figure 16E). Specifically, the stiff hybrid scaffold had a peak at 90° with normalized value of 0.015 ± 0.001, which was 24 ± 3 folds higher than the values at 0° and 180°. The collagen walls of the compliant hybrid scaffold had a slightly wider distribution of orientation, having a peak at 90° with a lower normalized value of 0.011 ± 0.002, which was 14 ± 4 folds higher than the normalized values in the transversal direction. Nonetheless, a clear collagen wall orientation predominantly in the axial (90°) direction was maintained also in the compliant hybrid scaffold.

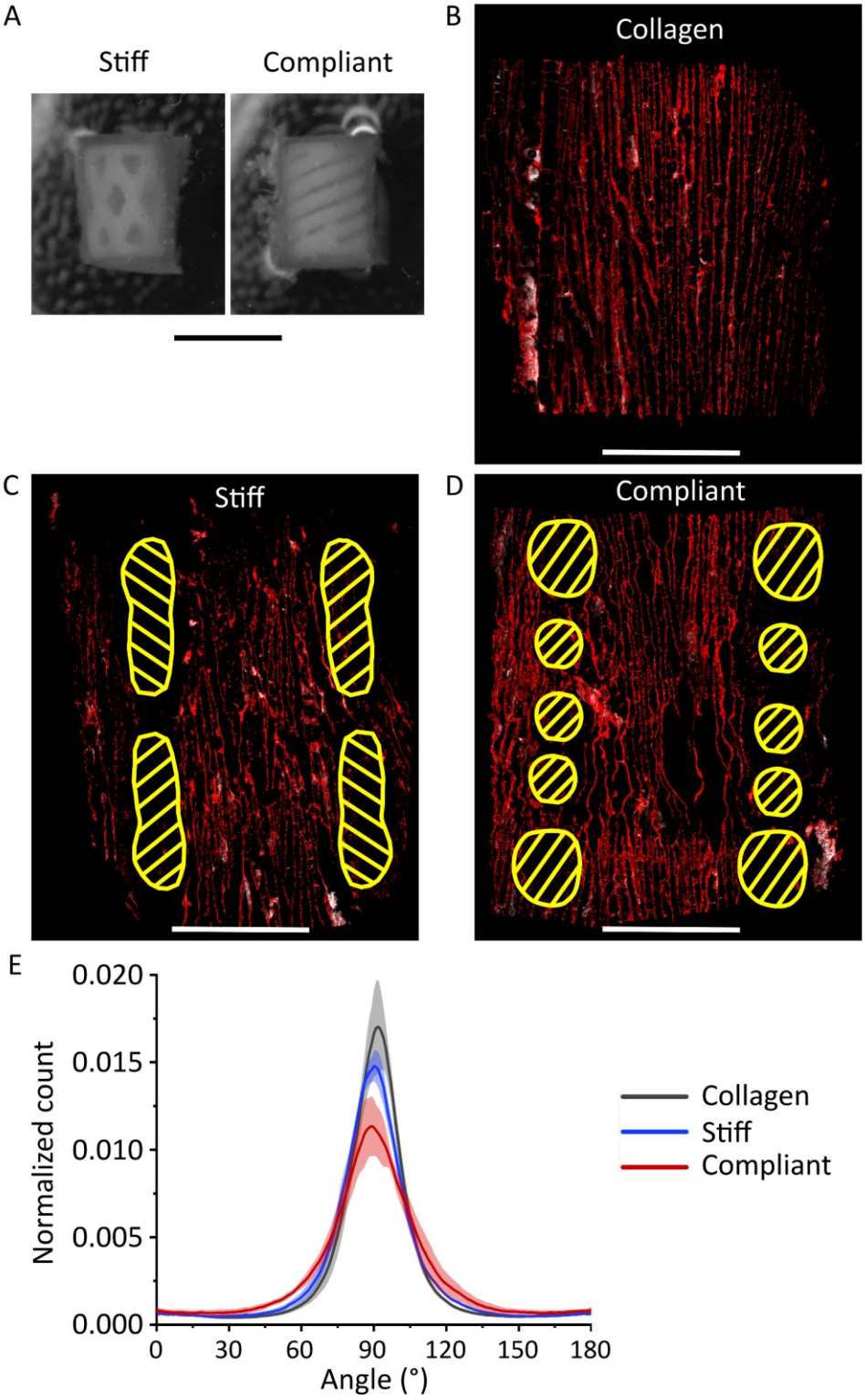

Figure 16: Morphology of collagen walls in stiff and compliant hybrid scaffolds. A) Pictures of stiff and compliant hybrid scaffolds. The scale bar is 5 mm; B), C), and D) representative images (maximum projections) of collagen wall morphology in collagen scaffold, stiff hybrid scaffold, and compliant hybrid scaffold, respectively. Fibrillar collagen type I and adsorbed fibronectin are visualized in white and red, respectively. Yellow striped areas mark the support structures. The scale bar is 2 mm; E) results of the orientation analysis (n = 3). Intensity values on the y-axis were normalized to the sum of all values measured over 360°. Results are given as average ± standard deviation.

3.8 Mechanical properties of multiscale hybrid scaffolds

The *k* of stiff and compliant hybrid scaffolds was evaluated by monoaxial compression tests and compared to the one of collagen scaffolds and the support structures alone, i.e. S_C and C_C (Figure 17A). Stiff hybrid scaffolds had a *k* of 75 ± 20 N/mm, which matched well the *k* of 72 ± 15 N/mm previously measured for the S_C support structures. The *k* of compliant hybrid scaffolds was 0.18 ± 0.03 N/mm, which was slightly higher than the *k* of 0.10 ± 0.02 N/mm of the C_C support structures. Both stiff and compliant hybrid scaffolds had a higher *k* than the collagen scaffolds, whose value was measured to be 0.068 ± 0.004 N/mm.

The fatigue resistance in *in vivo*-like conditions of stiff and compliant hybrid scaffolds was evaluated by means of dynamic compression tests in the bioreactor. Results showed that both scaffolds maintained the fatigue resistance that was engineered for the corresponding support structures (Figure 17B). In fact, the *k* values of stiff and compliant hybrid scaffolds recorded over 7 days of mechanical stimulation were almost undistinguishable from the *k* values previously measured for S_C and C_C support structures, respectively. At the beginning of the dynamic compression test, the *k* of stiff and compliant hybrid scaffolds was 26 ± 12 N/mm and 0.07 ± 0.04 N/mm, respectively. By the end of day 1, i.e. after 172,800 compression cycles, *k* reached a value of 36 ± 8 N/mm and 0.08 ± 0.02 N/mm for stiff and compliant hybrid scaffolds, respectively. Between day 1 and the end of the period of mechanical stimulation at day 7 (corresponding to 1,209,600 compression cycles), *k* showed a small increasing trend in both stiff and compliant hybrid scaffolds, reaching final values of 42 ± 9 N/mm and 0.10 ± 0.01 N/mm, respectively. However, *k* values at day 1 and 7 were within the variability for both stiff and compliant hybrid scaffolds and both scaffolds could be considered mechanically stable over the investigated period of time.

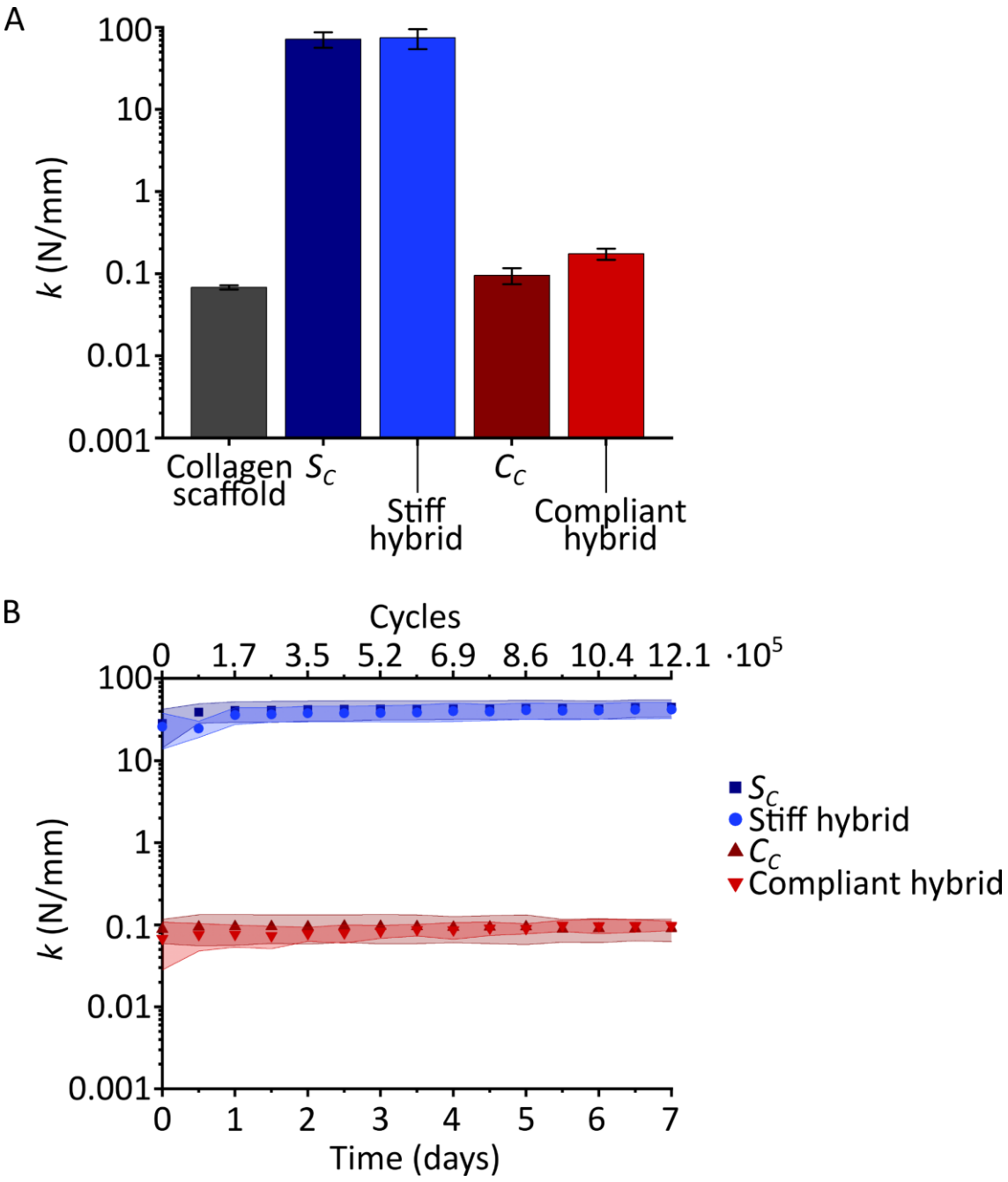

Figure 17: Mechanical characterization of stiff and compliant hybrid scaffolds. A) Stiffness (*k*) of stiff (n = 10) and compliant (n = 6) hybrid scaffolds. Values of *k* for collagens scaffolds (n = 3), stiff support structure (S_C), and compliant support structure (C_C) are included for comparison; B) fatigue resistance of stiff (n = 6) and compliant (n = 3) hybrid scaffolds. The fatigue behavior of S_C and C_C is included for comparison.

3.9 Cellular migration in multiscale hybrid scaffolds

Cellular migration into collagen scaffolds, stiff hybrid scaffold, and compliant hybrid scaffold was tested over 4 days of *in vitro* cell culture with human primary mesenchymal stromal cells (MSCs). To do so, a novel migration assay, which featured a 3D cell pellet as cell source, was developed (Figure 18A, B, and C).

The outcome of the novel migration assay was evaluated by comparing the average median migration distance (*d*) between scaffolds (Figure 18D). Collagen scaffolds resulted in a *d* of 161 ± 40 µm. In stiff and compliant hybrid scaffolds, *d* had slightly higher values of 201 ± 53 µm and 195 ± 46 µm, respectively. However, these higher values were within the variability of the measurement.

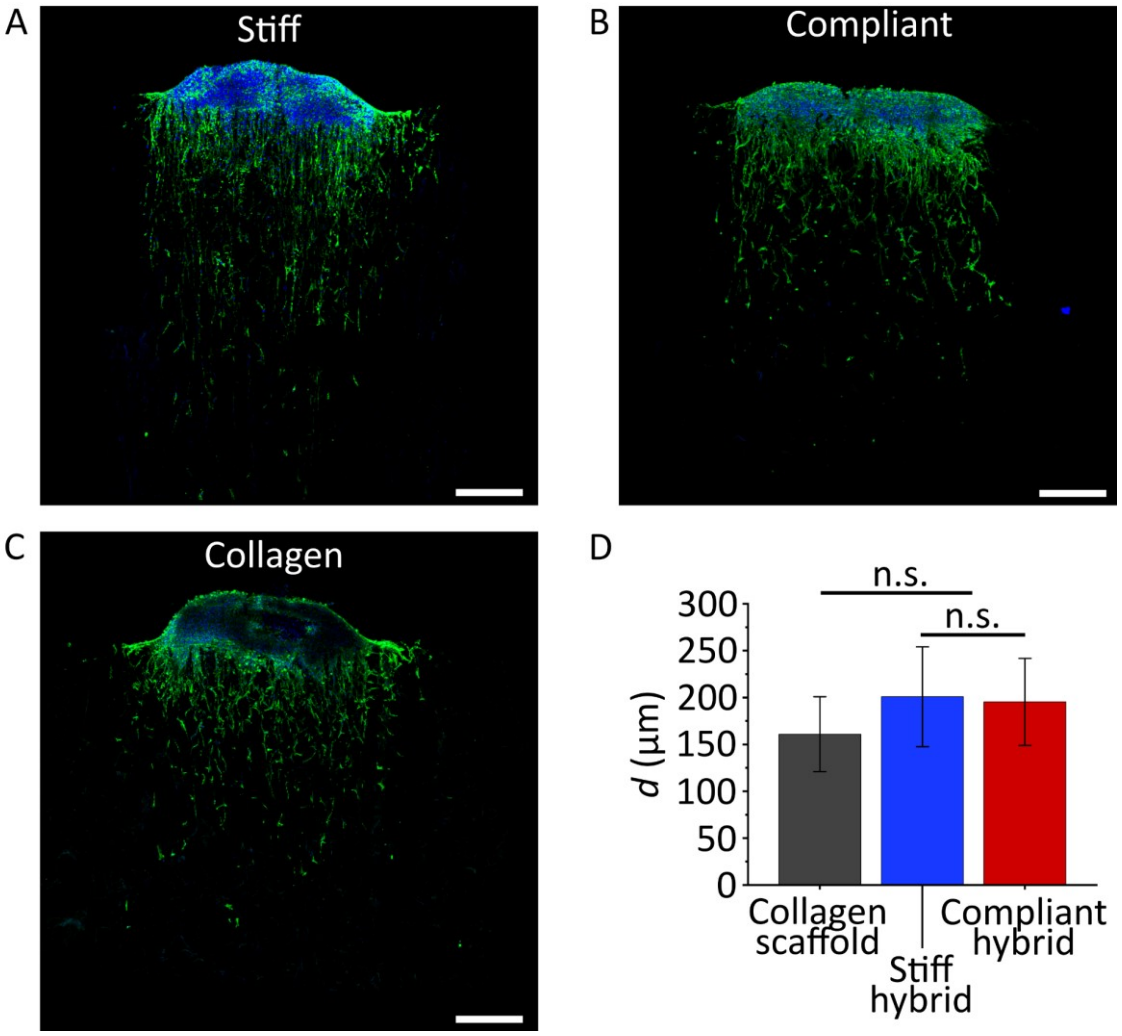

Figure 18: Cellular migration into stiff and compliant hybrid scaffolds. A), B), and C) Representative images (maximum projections) of migration assay in stiff hybrid scaffold, compliant hybrid scaffold, and collagen scaffold, respectively. Cell nuclei and F-actin are visualized in blue and green, respectively. Scale bars are 500 µm; D) quantification of the average median migration distance (*d*) in stiff (n = 6) and compliant (n = 7) hybrid scaffolds. Collagen scaffolds (n = 12) were tested as reference. Results are given as average ± standard deviation. Differences amongst groups were non-significant (n.s.).

3.10 Computational evaluation of osteochondral defect healing

An axisymmetric computational model representing a knee femoral condyle featuring an osteochondral defect was developed to study the mechanics-dependent healing of the defect in absence and in presence of scaffolds. Results were analysed in terms of the distribution and magnitude of octahedral shear strain (γ) and mechanics-dependent

differentiation stimulus (*S*), which determined the types and distribution of formed tissues (granulation tissue, cartilage, bone, fibrous tissue).

3.10.1 Healing of empty osteochondral defect

In the empty osteochondral defect, the distribution and magnitude of γ varied throughout the healing process. In fact, a high peak of γ (50%) was observed at the subchondral bone-cartilage-defect interface at early time points, but it later smoothened and disappeared (Figure 19A). Very low (<1%) and high (∼20%) values of γ were observed at the proximal base of the defect and at the articular surface, respectively (Figure 19A).

The prediction of tissue formation based on *S* indicated that the mechanical environment would have favoured the formation of cartilage in the defect at early time points, with limited areas of bone resorption and bone formation in the proximal-central and proximal-lateral regions of the defect, respectively (Figure 19B left). Moreover, fibrous tissue was predicted to grow at the subchondral bone-cartilage-defect interface (Figure 19B left). With the progression of the healing process, the prediction of tissue formation based on *S* changed drastically (Figure 19B middle and right). In fact, the formation of a thick layer of fibrous tissue was predicted at the articular surface. In the proximal-lateral region of the defect, bone was predicted to grow until the healthy subchondral bone-cartilage interface, but in the proximal-central area bone resorption was observed, with the formation of a cyst. Very low amounts of cartilage were predicted to form in the middle region of the defect.

Cellular invasion of the defect progressed from proximal to distal regions, accordingly to the MSCs source in the bone marrow (Figure 19C). By day 20 of the healing process, the defect was fully populated by cells (Figure 19C, D, E, and F). The distribution of osteoblasts, chondrocytes, and fibroblasts by the end of the healing process matched the distribution of bone, cartilage, and fibrous tissue predicted by *S*, respectively (compare Figure 19D, E, and F right to Figure 19B right). For this reason, tissue distributions at day 50 as calculated with the prediction of tissue formation based on *S* were considered the healing outcome in all subsequent evaluations.

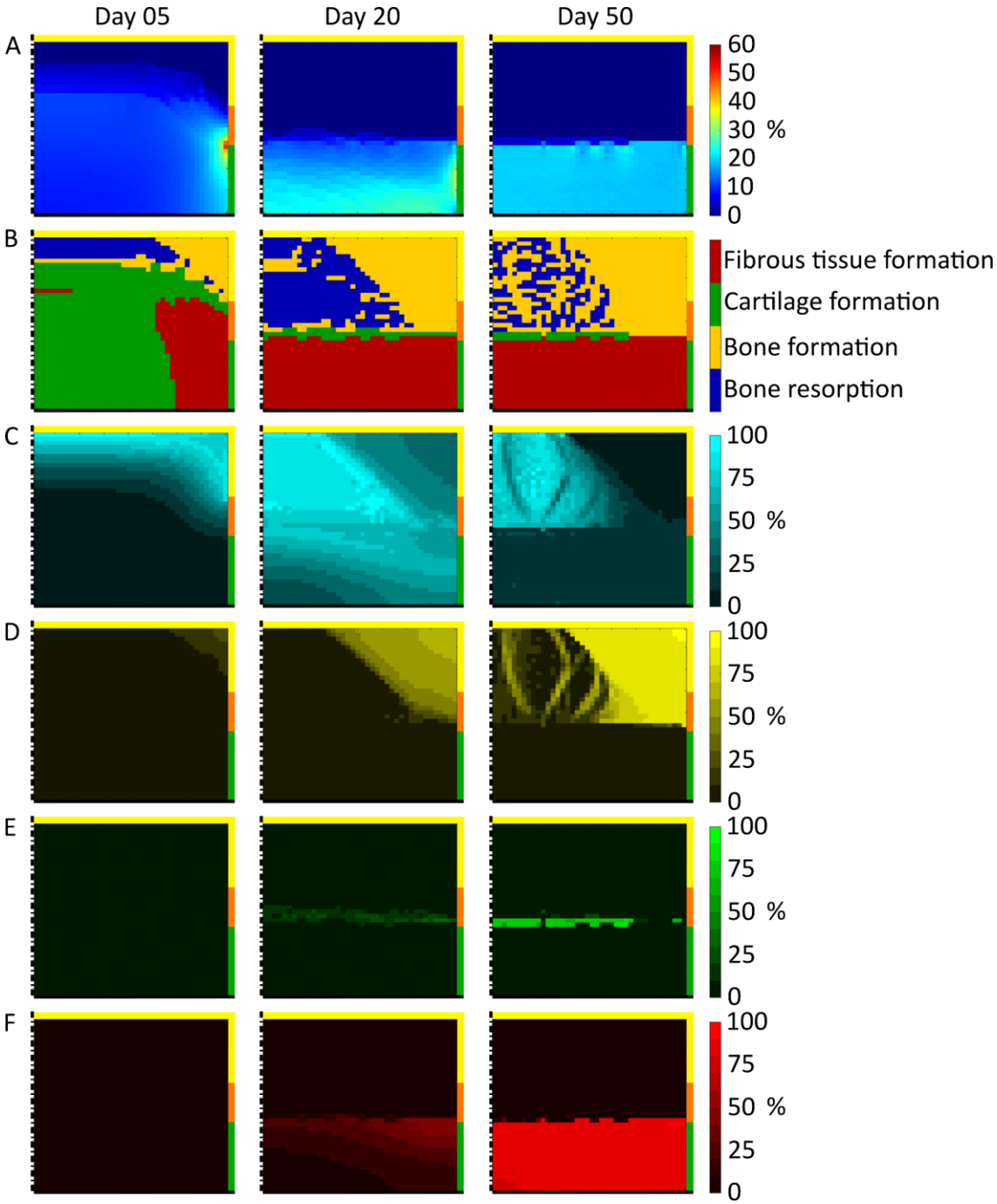

Figure 19: *In silico* healing of empty osteochondral defect. A) Distribution of octahedral shear strain (γ); B) prediction of tissue formation based on the mechanical stimulus (*S*); C), D), E), and F) quantities and distributions of MSCs, osteoblasts, chondrocytes, and fibroblasts, respectively. The colors of the borders code the neighboring tissues in the FE model of the knee: yellow, orange, and green stand for cancellous bone, subchondral bone, and cartilage, respectively. The axis of symmetry and the articular surface are indicated by the black dash-dot line and the black solid line, respectively. Reproduced from [75] under CC BY 4.0 [65].

3.10.2 Healing of osteochondral defect with scaffold

The influence of scaffold mechanical properties on the mechanics-dependent healing of osteochondral defects was investigated by implementing a scaffold composed of three

vertical elements in the defect and by systematically varying its material elastic modulus with the following values: 0.1 MPa (low stiffness scaffold); 10 MPa (intermediate stiffness scaffold); and 1000 MPa (high stiffness scaffold). Moreover, a scaffold with biphasic mechanical properties was tested, having a 1000 MPa and 10 MPa material elastic modulus in the proximal and distal halves, respectively. Additionally, the influence of scaffold architecture on the healing process was evaluated by implementing a grid-like scaffold featuring both vertical and horizontal elements and a material elastic modulus of 1000 MPa.

The low stiffness scaffold generated strains that were similar to those found in the empty defect both in magnitude and distribution throughout the healing process (compare Figure 20A to Figure 19A). Consequently, the prediction of tissue formation based on *S* was also comparable to the one obtained from the empty osteochondral defect (compare Figure 20B to Figure 19B), with fibrous tissue forming at the articular surface, cartilage forming in the middle of the defect, bone resorption in the proximal-central area, and bone formation in the proximal-lateral area.

The medium stiffness scaffold had a significant influence on the strain in the defect. In fact, a region of high γ (up to 60% at day 5, between 17% and 40% at later time points) was consistently found in the region neighboring healthy tissues throughout the repair process (Figure 20C), in which fibrous tissue was predicted to form (Figure 20D). At day 50, γ had low values (<1%) at the proximal base of the defect and higher values (10-15%) at the articular interface (Figure 20C). Based on *S*, a fragmented layer of cartilage was predicted to form at the proximal base of the defect, while non-extensive bone formation was predicted to occur at the proximal-lateral corner (Figure 20D).

When the high stiffness scaffold was implemented, the values of γ were generally low (<10%) in the whole defect and throughout the healing process (Figure 20E). Higher γ values of 20% were observed only at the interface with healthy cartilage and subchondral bone, while very low γ values (<1%) were found at the proximal base of the defect. The prediction of tissue formation based on *S* indicated an extensive growth of cartilage in the whole defect, with the exception of the proximal base and the subchondral bone-cartilage defect interface, where bone and fibrous tissue formed, respectively (Figure 20F). The implementation of the high stiffness scaffold resulted in a remarkable absence of bone resorption.

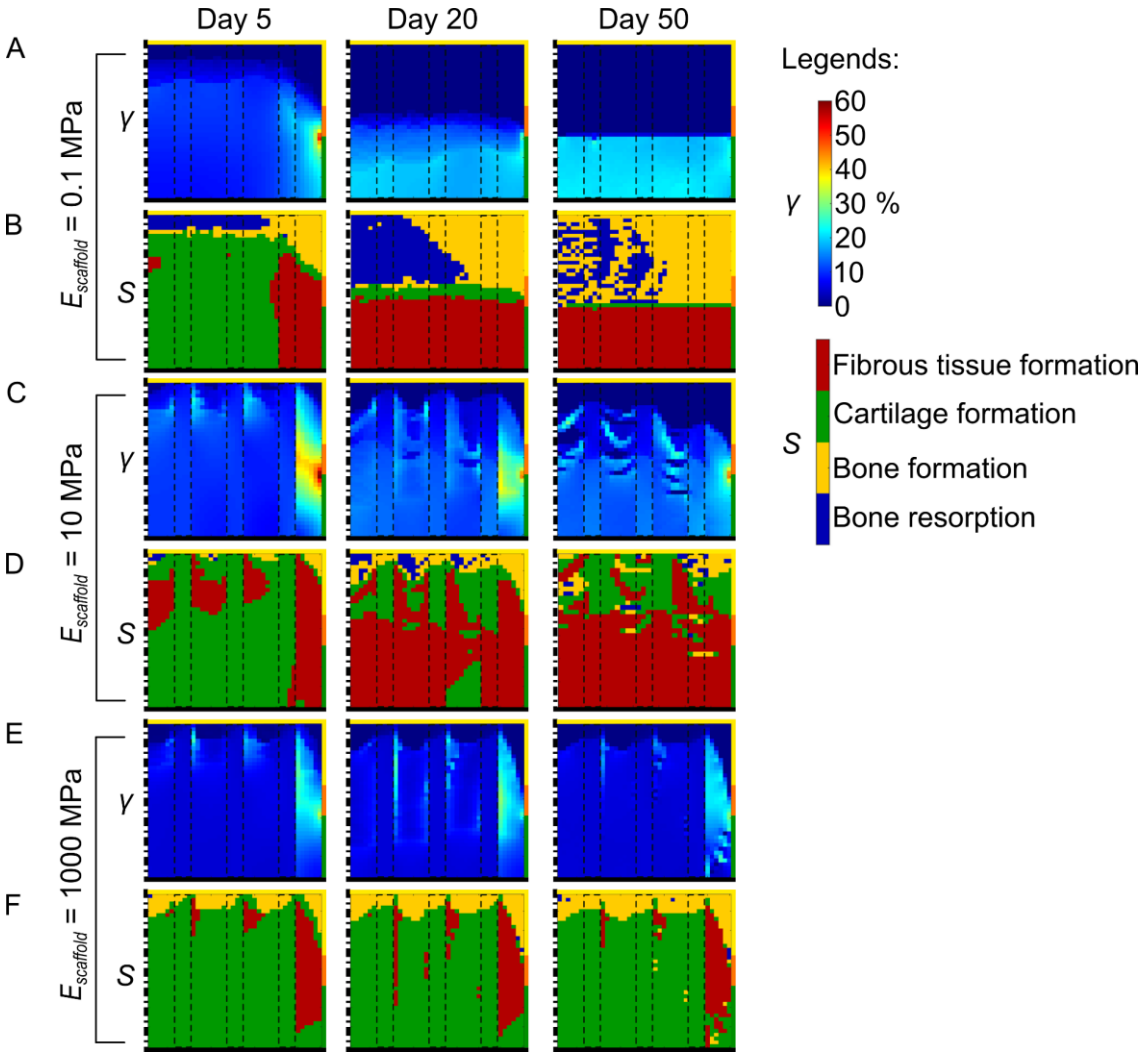

Figure 20: *In silico* healing of osteochondral defect with monophasic scaffolds. A), C), and E) Distribution of octahedral shear strain (γ) with low stiffness, medium stiffness, and high stiffness scaffolds, respectively; B), D), and F) prediction of tissue formation based on the mechanical stimulus (*S*) with low stiffness, medium stiffness, and high stiffness scaffolds, respectively. The colors of the borders code the neighboring tissues in the FE model of the knee: yellow, orange, and green stand for cancellous bone, subchondral bone, and cartilage, respectively. The axis of symmetry and the articular surface are indicated by the black dash-dot line and the black solid line, respectively. Black dashed lines outline the scaffold struts. Reproduced from [75] under CC BY 4.0 [65].

The biphasic scaffold generated a mechanical environment analogous to the one observed in the empty osteochondral defect, with low (<1%) and high (~20%) γ values in the proximal and distal regions of the defect, respectively (Figure 21A). Consequently, the prediction of tissue formation based on *S* was similar as well, with fibrous tissue formation, bone formation, and bone resorption at the articular interface, proximal-lateral area, and proximal-central area, respectively (Figure 21B).

The implementation of the grid-like scaffold resulted in generally low values (<5%) of γ in the whole defect throughout the repair process (Figure 21C). Exceptions were the subchondral bone-cartilage-defect interface, where γ had high values reaching a peak

of 60%, and the horizontal scaffold struts, where γ was lower than 1%. The prediction of tissue formation based on *S* indicated the extensive formation of cartilage in the defect, with bone formation at the proximal base and ectopically within the distal horizontal strut, and fibrous tissue formation at the interface with the surrounding healthy tissues (Figure 21D).

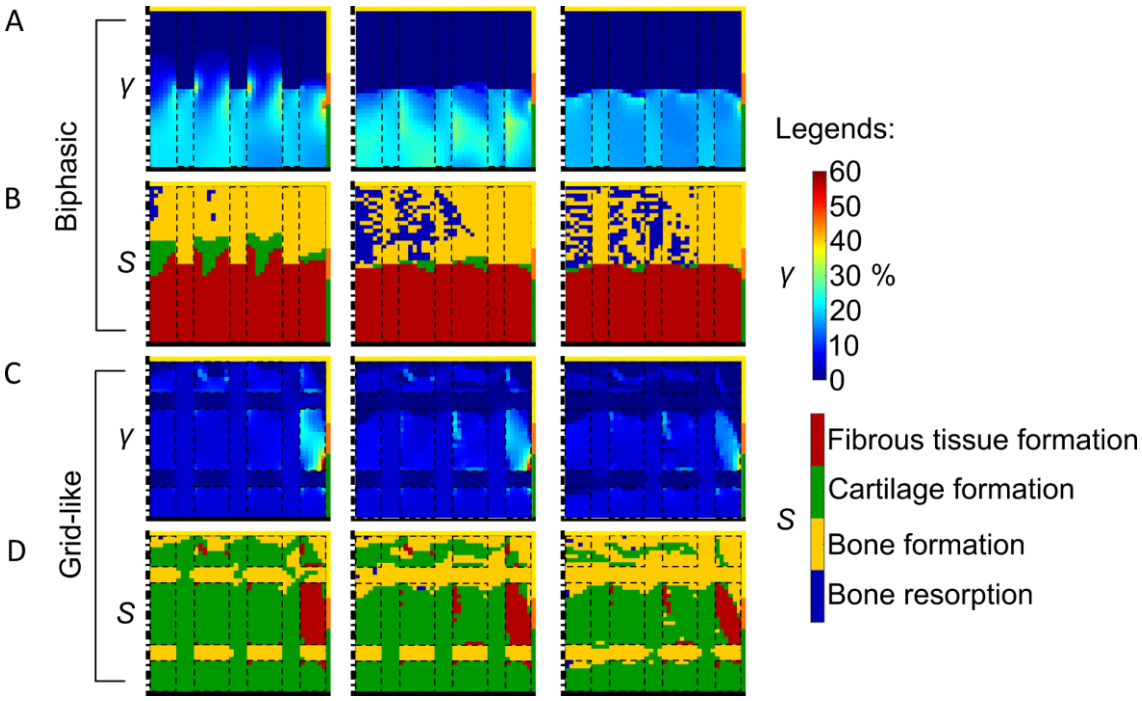

Figure 21: *In silico* healing of osteochondral defect with biphasic and grid-like scaffolds. A) and C) Distribution of octahedral shear strain (γ) with biphasic and grid-like scaffolds, respectively; B) and D) prediction of tissue formation based on the mechanical stimulus (*S*) with biphasic and grid-like scaffolds, respectively. The colors of the borders code the neighboring tissues in the FE model of the knee: yellow, orange, and green stand for cancellous bone, subchondral bone, and cartilage, respectively. The axis of symmetry and the articular surface are indicated by the black dash-dot line and the black solid line, respectively. Black dashed lines outline the scaffold struts. Reproduced from [75] under CC BY 4.0 [65].

4 Discussion

Hybrid scaffolds with multiscale mechanical properties were developed by including synthetic support structures into collagen scaffolds having a highly aligned architecture, which have been shown to induce bone formation by endochondral ossification *in vivo* [33]. The purpose of the support structure in the hybrid scaffolds was both to provide mechanical support at the tissue level and to enable the controlled tuning of the scaffold-dependent mechanical environment. The aim was to use the mechanical properties of the hybrid scaffolds to steer the endochondral ossification process to form either bone or cartilage, thereby representing a potential treatment strategy for critical size bone defects or osteochondral defects, respectively. A stiff and a compliant support structure were developed to prove the concept by *in vivo* experiments in large bone defects in rats, which will be performed in a concomitant project at the Julius Wolff Institute. At the same time, the targeted mechanical and architectural properties of scaffolds to support the healing of osteochondral defects were explored by means of computational models.

4.1 Development of stiff and compliant support structures

The synthetic support structure to be included in the hybrid scaffold needed to be biocompatible, bioresorbable, and highly porous. Moreover, the possibility to precisely control its architecture was of advantage for two main reasons. First, it enabled the choice of a distribution of synthetic material that impaired as little as possible the bioactive properties of the collagen scaffold, which provided structural guidance for cells and ECM during the healing process. Second, it allowed the tuning of the mechanical properties of the support structure by means of its architecture.

Additive manufacturing techniques grant high versatility in the production of 3D objects with controlled and reproducible geometries and, consequently, they are attractive production methods for TE scaffolds [78]. Amongst all the addictive manufacturing techniques, selective laser sintering (SLS) is particularly suitable to produce the support structure to be included in the hybrid scaffold because it does not require potentially toxic modifications of the raw materials and it enables the reproduction of architectures with overhanging regions without the need for an additional temporary substrate to serve as support [44]. Moreover, one of the materials that can be processed by SLS is PCL [46], which is an FDA-approved biodegradable polymer [51]. Thus, the production of support structures by SLS from PCL complies with both material- and technique-related requirements. However, the use of PCL in SLS is still mostly confined to research [46], which results in the need for an ad-hoc adaptation of the SLS process parameters to each specific application, as seen in numerous cases in literature [54–57]. For this reason, a proof of manufacturability by SLS of preliminary support structure designs was

here performed by producing them from PA, for which the SLS process is so well-established that it is commonly used also in commercial applications [44,46].

An initial screening of possible support structure designs was performed by building a CAD library and by evaluating the morphologies and architecture-dependent mechanical properties of each design in terms of porosity and stiffness. Specifically, the architecture-dependent stiffness was measured by performing FE analyses in compression based on the CADs, from which the computational stiffness was evaluated. For an easier comparison with the mechanical properties of biological tissues, whose elastic modulus is frequently reported in literature (e.g. for bone [42,79,80] and cartilage [80–82]), each design was approximated to a uniform material. The computational elastic modulus of these uniform materials was calculated from their computational stiffness. Such an approximation is commonly used in the development of scaffolds for TE and numerous examples of it can be found in literature, e.g. in bone [33,83,84] and osteochondral TE [61,62,85,86]. Based on porosity and computational elastic modulus, seven designs, named CAD1 to CAD7 (Figure 9A), were selected from the CAD library to be produced by SLS from PA.

CAD1 to CAD7 were all hollow hexagonal cylinders, a geometry that not only left ample room to the biological regeneration process to be induced by the collagen scaffold, but also enabled the easy design of bigger scaffolds by combining multiple units in a honeycomb fashion. However, CAD1 to CAD7 differed in architecture (Figure 8A), which resulted in different morphological and mechanical properties. For example, all designs had a porosity higher than 75%, but ranging from a minimum of 77% for CAD4 to a maximum of 85% for CAD1 (Table 7). Similarly, the computational elastic modulus varied from a minimum of 34 MPa for CAD1 to a maximum of 803 MPa for CAD7 (Table 7). Therefore, all investigated CADs had a significantly higher computational elastic modulus than the experimental elastic modulus of 8.5 kPa reported for the collagen scaffolds [33]. Moreover, the stiffness range covered by the CADs matched well that of the biological tissues of interest. In fact, the elastic modulus of cartilage has been reported to be of 10s of MPa [82] and that of cancellous bone to range from 100 to 2000 MPa [42] (although values can reach up to 15 GPa, depending on the measurement method [87]). Cortical bone, however, has a significantly higher elastic modulus in the GPa range [42,79,80].

All investigated CADs were successfully produced by SLS from PA (Figure 8B), thereby proving the manufacturability of each design with the chosen technique. However, the elastic modulus of the designs measured from monoaxial compression tests was consistently lower than the computational elastic modulus (Table 7), with values ranging from 0.26 ± 0.04 MPa for CAD1 to 24 ± 3 MPa for CAD7. The discrepancy could derive both from inaccuracies in the FE analyses and from a sub-optimal sintering during production. In the case of the FE analyses, a material elastic modulus of 1700 MPa was assigned to the designs, which was the value reported by the commercial supplier for

the tensional elastic modulus of sintered PA [48]. However, the compressive elastic modulus of sintered PA was unknown and could be expected to differ from the tensional one, as the behavior of polymers in tension or in compression may vary [88]. This presumably led to a sub-optimal setup of the FE analysis and thereby to non-accurate results. Concerning the sintering process, all designs had a minimum feature size of 500 µm, which was slightly lower than the suggested resolution limit of 700 µm of the commercial SLS process [48] and could have resulted in a sub-optimal sintering that negatively influenced the mechanical properties of the designs. This issue was expected to be overcome by the ad-hoc adjustment of the SLS process parameters for PCL.

Although the FE analyses indicated that all designs would deform uniformly (Figure 8C), experimental observations during the monoaxial compression tests revealed that this was not the case for CAD2, CAD3, and CAD5 (Figure 8D). Moreover, CAD6 and CAD7, whose struts were oriented predominantly in the axial direction, underwent buckling already at a low compression of 3% (Figure 8D). The discrepancy could derive from the simplifications applied in the computational models, where the designs had smooth surfaces and linear elastic material properties, while in the experimental setting the designs had rough surfaces (derived from the SLS process [48]) and viscoelastic and viscoplastic components in the behavior of the material. Nonetheless, two designs with both computational and experimental uniform deformation and a high difference in elastic modulus were identified, i.e. CAD1 and CAD4, and selected as compliant and stiff designs of support structures, respectively. The size of the designs was adapted for an easier *in vitro* handling, generating the preliminary stiff and compliant support structures, named S_P and C_P, respectively (Figure 9A). The S_P and C_P support structures were produced by SLS from PA (Figure 9B) and tested in compression. Even with the adapted size, S_P and C_P maintained the high difference in stiffness, with S_P having an elastic modulus 7.2 ± 0.9 folds higher than C_P.

The S_P structure was used as reference in the adjustment of the SLS process parameters for PCL. First, a suitable PCL powder was sought by testing three PCL powders having nominal number average molecular weight ($\overline{M}_n$) of either 60,000 g/mol or 100,000 g/mol and size of either 25–50 µm or 50–80 µm. Then, the sterilization method resulting in the fewest alterations of the mechanical and material properties of the PCL support structures was chosen between gamma irradiation and ethylene oxide (EtOx). Finally, the influence of SLS process parameters on the mechanical and morphological properties of S_P was investigated by systematic variations of laser power, laser beam compensation, and laser beam diameter during production and subsequent measurements of elastic modulus by monoaxial compression tests and strut diameter from light microscope pictures.

Concerning the PCL powders, S_P support structures produced from the two PCL powders with a nominal $\overline{M}_n$ of 60,000 g/mol had an elastic modulus almost 2 folds higher than the ones produced from the powder with $\overline{M}_n$ of 100,000 g/mol (Figure 10A). Although

semi-crystalline polymers, such as PCL [51], tend to be more ductile and stronger at higher molecular weights [88], a higher molecular weight also causes a higher viscosity of the molten polymer [86]. As a higher melt viscosity results in a lower sintering rate [89,90], this effect might have caused the powder with the higher $\overline{M}_n$ to result in structures with lower elastic modulus. Another contribution to the phenomenon might derive from the crystallinity of PCL, which decreases with increasing molecular weight, thereby lowering the resulting elastic modulus [91]. Although the particle size of the PCL powders did not have an influence on the mechanical properties of S_P (Figure 10A), it resulted in very different powder behaviors during the SLS process. In fact, PCL particles with size of 50–80 µm were evenly spread in the building chamber by a roller that was purposely equipped with an ionizer (Figure 10B), whereas PCL particles with size of 25–50 µm formed agglomerates despite the presence of the ionizer (Figure 10C). This behavior was consistent whit literature, where particles with a size smaller than 45 µm were reported to be unsuitable for SLS due to the high electrostatic forces that cause particle aggregation [44]. Thus, the PCL powder with size of 50–80 µm had a better flowability, defined as the ability of the powder to flow in a desired manner in a specific piece of equipment [92]. Considering both the good flowability and the comparatively high elastic modulus of the resulting sintered structures, the PCL powder with nominal $\overline{M}_n$ of 60,000 g/mol and particle size of 50–80 µm was chosen for support structure production and was employed in all subsequent experiments.

In regards of sterilization, the influence of EtOx and gamma irradiation on the stiffness and molecular weight of the sintered support structures was evaluated by means of monoaxial compression tests and size exclusion chromatography (SEC), respectively. In fact, sterilization is pivotal in the production of TE devices for implantation [42]. At the same time, it should be ensured that the properties that were engineered for the support structures would not be drastically altered during the sterilization process. The elastic modulus of unsterile, gamma-sterilized, and EtOx-sterilized S_P support structures were found to be comparable (Table 8). Moreover, the $\overline{M}_n$ and dispersity indexes of unsterile and EtOx-sterilized supports were found to be similar to each other and to the unsintered PCL powder (Table 8), proving the absence of negative influences on PCL molecular weight not only of the EtOx sterilization, but also of the sintering process itself. On the contrary, gamma-sterilized S_P structures showed a noteworthy decrease of 35% in $\overline{M}_n$ (Table 8), which is significant in respect of the 10% error that characterizes the SEC analysis [93]. Moreover, gamma-sterilized structures had a higher dispersity index of 2.2 compared to the other investigated samples, which had a dispersity index of 1.8 (Table 8). In literature, the sterilization of PCL by gamma irradiation yielded a variety of different results, ranging from a reduction in tensile stiffness [94], to no differences in tensile mechanical behavior [95], and even to an improvement in tensile yield points [96]. Despite the variable influence on PCL mechanical properties, all cited studies consistently reported an impact of gamma irradiation on PCL molecular weight, comparably to the results obtained here. Although no alterations of the elastic modulus

of S_P were observed here in consequence of gamma sterilization, the reduced $\bar{M}_n$ might result in variations in the degradation of the support structures, thereby influencing the long term stability of the hybrid scaffolds. In fact, PCL undergoes a molecular weight-dependent degradation *in vivo* [97]: first, hydrolysis cleaves long polymeric chains [51]; then, cells take up PCL fragments smaller than 3000 g/mol [98]. Neither the stiffness nor the molecular weight of the PCL support structures were altered by EtOx sterilization. Moreover, EtOx sterilization has been previously employed on collagen scaffolds [33]. Therefore, EtOx was selected as sterilization method of the hybrid scaffolds.

SLS process parameters were found to significantly influence the mechanical and morphological properties of S_P structures. In fact, the resulting strut diameters ranged from being 0.8 to 1.6 folds of the design strut diameter of 500 µm, while the maximum value of elastic modulus was 18.9 folds higher than the minimum one (Figure 11). A certain degree of variability was observed amongst separate sintering processes, meaning that structures produced with the same set of SLS process parameters, but during sintering processes performed at different times, could result in different properties of the produced S_P (see upright red triangles with full shape in Figure 11). A maximum variation of 40% and 7% in elastic modulus and strut diameter, respectively, were observed. Such a variability is considered characteristics of the SLS process and its origins have been identified in both material-related [47] and process-related [47,99] features. Despite the intrinsic variability of the SLS technique, significant observations could be performed. In fact, small strut diameters generally corresponded to low elastic moduli, while large strut diameters were associated to high elastic moduli (Figure 11). However, this general trend could not fully explain the differences in elastic modulus that were measured in S_P structures having similar strut diameter, such as points “C” and “D” in Figure 11.

To investigate more in depth the dependency of the stiffness on the strut diameter, six prototypes produced with different sets of SLS process parameters and covering the wide range of measured elastic moduli and strut diameters (Table 9) were selected for morphological analysis. The six prototypes, named prototype “A” to “F” (Figure 12B), were cut to ¾ of their height, as schematically shown in Figure 12A, and imaged by scanning electron microscopy (SEM). The molten cross-sectional area of each strut was evaluated from the SEM images (Figure 12C) and used to calculate the molten diameter. Additionally, the theoretical dependency of the stiffness on the strut diameter for S_P was derived by means of computational simulations, resulting in the quadratic polynomial expressed by Equation 12. The results of the morphological analysis indicated not only that the molten diameter could explain the differences in elastic modulus observed in prototypes with similar strut diameters (e.g. points “C” and “D” in Figure 12D), but also that the dependency of the elastic modulus on the molten diameter reflected the theoretical one (Equation 13), while the dependency of the elastic modulus on the strut diameter did not (Equation 14). Interestingly, at high

diameter values, the difference between molten diameter and strut diameter was almost constant at 100 µm (Figure 12D), corresponding to a layer of not fully molten particles with a thickness of 50 µm (i.e. roughly the diameter of one particle). Moreover, the molten diameter/strut diameter ratio at high molten diameter values tended towards the ideal value of 1 (Figure 12E). On the contrary, the molten diameter/strut diameter ratio was disproportionally smaller for low molten diameter values (Figure 12E).

The cytocompatibility of the prototypes "A" to "F" (Table 9) was tested by *in vitro* cell culture of primary human mesenchymal stromal cells (MSCs) exposed to medium conditioned with the six prototypes. The effect of the conditioned medium were evaluated by measuring cellular metabolic activity and number and by comparing them to control cells, which were cultured in regular cell culture conditions (10% expansion medium). Over six days of cell culture, cellular metabolic activity increased 4.2 folds for all tested conditions (Figure 13A). Such increase was ascribed to the concomitant cellular proliferation, which resulted in a cell number increase of approximately 5 folds at day 6 (Figure 13B). No differences in behavior were observed between control MSCs and MSCs cultured in conditioned media, thereby proving the *in vitro* cytocompatibility of all tested prototypes of PCL support structures. The cytocompatibility of PCL scaffolds produced by SLS has previously been shown over 3 days of *in vitro* cell culture with osteoblasts [100]. Here, it was additionally proven that PCL remains cytocompatible when processed by SLS over a wide range of SLS process parameters (see Table 9).

Altogether, the morphological analysis indicated that the molten diameter values better predict the mechanical competence of the S_P structures compared to the strut diameter. Additionally, the strut diameter and the associated molten diameter do not vary proportionally, resulting in a particularly unfavorable SLS-derived mechanical competence of the S_P structures at low diameter values. In this case, the SLS-derived mechanical competence of the sintered object is defined as the mechanical properties resulting from the implementation of the SLS technique, where a sub-optimal sintering of the powders might result in defects that negatively influence the overall mechanical performance of the piece. While an improvement in the SLS-derived mechanical competence could be achieved simply by increasing the strut diameter of the design, such a solution would conflict with the requirement of high porosity defined for the support structures. Thus, a design strut diameter representing a compromise between the contradicting needs for high porosity and for mechanical stability was defined at approximately 550–590 µm. To increase the design strut diameter of the S_P support structure without altering its high porosity of 77.2%, possible design improvements were evaluated by topology optimization. The design of scaffolds by topology optimization has been already employed in TE, e.g. generating bone TE scaffolds with isotropic mechanical properties and porosity [101], or scaffolds with tailored mechanical and transport properties [102]. Here, topology optimization was employed

to identify sub-optimal features of the design, which were not substantially contributing to its load bearing ability. These sub-optimal features were, then, removed by manual modifications of the design. Other sub-optimal features of the S_P design, such as sharp edges that constituted crack-nucleation points, were recognized during the experimental mechanical testing and similarly removed. The volume of material first found in these sub-optimal features was redistributed on the struts, increasing the design strut diameter from 500 to 540 µm, but maintaining a porosity of 77%. Moreover, the size of the support structure was altered to optimally fit the geometrical constraints of the *in vivo* large bone defect model, resulting in the S_H support structure design with a porosity of 71.1% (Figure 14A left). The features that were optimized for the stiff support structure were also applied to the compliant one, generating the C_H support structure design with a porosity of 78.4% (Figure 14A right). As the morphological analysis of the S_P support structures previously determined that the extent of the strut molten core depended on the set of SLS process parameters and that it was predictive of the SLS-derived mechanical competence of the support structures, the ideal set of SLS process parameters for S_H and C_H designs (and all the subsequent designs) was determined by evaluation of the molten core directly during the sintering process. Additionally, no concerns on the cytocompatibility of the material were associated to the choice of SLS process parameters, as previously proven by the cytocompatibility test. Thus, S_H and C_H support structures with optimized SLS-derived mechanical competence were produced from PCL (Figure 14B).

The stiffness of the S_H support structures was 7.9 ± 0.6 folds higher than the one of the C_H support structures (Figure 14C). This significant difference in stiffness was achieved only by architectural variations of the support structures, while employing the same material and production technique for both. Examples of differences in stiffness achieved by differences in morphology in scaffolds made from the same material can be found literature, e.g. in scaffolds for osteochondral defect healing [61,62]. However, in the cited examples, the differences in morphology were obtained by variations of porosity, with scaffolds having a higher porosity resulting in a lower stiffness, as opposed to the controlled architectural variation in scaffolds with similar porosity here proposed. If scaffolds differ in porosity as well as in stiffness, the evaluation of purely mechanics-dependent influences on healing is impaired [61], thereby rendering this approach unsuitable to generate the stiff and compliant support structures for the *in vivo* evaluation of the hybrid scaffolds.

When implanted *in vivo*, scaffolds generally undergo cyclic loading. Moreover, the *in vivo* environment is wet and at a body temperature of 37°C. The mechanical performance of polymers may vary depending on the temperature at which they are tested, specifically in relation to their glass transition temperature [88]. The glass transition temperature of semi-crystalline polymers is the temperature at which the amorphous part of the polymer becomes more motile, thereby giving to the whole

polymer a rubber-like behavior [103]. Above the melting temperature, also the polymeric chains in the crystalline regions become motile and the polymer can be molded and shaped [103]. Such an observation is particularly relevant for PCL, whose glass transition temperature and melting temperature are -60°C and 59–64°C (depending on the molecular weight), respectively [51]. Moreover, the fatigue life of polymers generally decreases as temperature increases [88]. Therefore, it could be expected to observe differences in the mechanical performance of the support structures if tested at room temperature or at body temperature. Additionally, the hybrid scaffolds need to maintain their mechanical stability in large bone defects at least until a bony bridge is established across the defect. Therefore, it was pivotal to assess the mechanical performance of the support structures under cyclic loading in an environment simulating as closely as possible the one found *in vivo*. A bioreactor [69] was employed to test the fatigue resistance of the support structures under cyclic loading in wet environment at 37°C and 5% CO_2 using the same loading pattern found in the large bone defect model intended to be used in the concomitant *in vivo* experiments (i.e. rat). The cyclic loading was continuously applied for one week, which would correspond to a longer period in the *in vivo* setting, as the animals would have rest times in which the large bone defect would be unloaded. However, a precise estimation of the corresponding survival time in the *in vivo* setting was not attempted, as the extent of the time periods of bone unloading is difficult to predict. A preliminary test of S_H and C_H support structures in the bioreactor showed that C_H support structures failed after less than one day of mechanical stimulation (Figure 14D). The reason for the early failures was identified in the large lateral displacement to which the corners of the hexagonal cylinder were subjected. Although to a lower extent and seemingly without impairment of the fatigue resistance (Figure 14D), also S_H support structures experienced the large lateral displacement. The support structure design intended for human use will be composed of a honeycomb of the repetitive units here represented by the individual support structures. When included in the honeycomb assembly, each unit would receive an additional support by the neighboring ones, which would reduce the lateral displacement as observed here. If such a reduction in displacement would be sufficient to avoid early fatigue failures of the large support structure is a matter that needs further experimental evaluation. However, it appeared clear that the lack of this lateral support was a critical issue for the application of the support structure with hexagonal cross-sections to the large bone defect model in rats. Therefore, stiff and compliant support structures with a reduced lateral displacement were designed by switching the shape of their cross-section from a hexagon to a circle. Multiple support structure architectures were evaluated in design–test feedback loops, in which the designs were updated based on the results obtained in the fatigue resistance tests. This process led to the definition of the stiff and compliant support structure designs named S_C and C_C, respectively (Figure 15A). A high and comparable porosity of 66.6% and 68.6% was maintained in the S_C and C_C support structure designs, respectively. Both designs

were successfully produced by SLS from PCL (Figure 15B) and were proven to maintain a significant architecture-dependent difference in stiffness, with the S_C support structure being 700 folds stiffer than the C_C support structure (Figure 15C). When implanted *in vivo* combined to the external fixator of stiffness 13.5 N/mm, the stiff and compliant support structures would result in a total stiffness of 85.5 N/mm and 13.6 N/mm, respectively. Thus, the stiff scaffold–external fixator system would be approximately 6 folds stiffer than the compliant one. The modification of the support structure design succeeded in improving their fatigue resistance in *in vivo*-like conditions, as both S_C and C_C did not result in any breakage and maintained their stiffness unaltered over one week of continuous mechanical stimulation (Figure 15D), corresponding to 1,209,600 loading cycles.

In conclusion, stiff and compliant support structures were developed beginning from the establishment of the most suitable parameters of the production technique until the fulfillment of application-specific requirements. First, the most appropriate PCL powder for SLS in terms of molecular weight and particle size was selected amongst the available ones and the possibility of support structure sterilization with little impact on its material and mechanical properties was assessed. Then, a method to produce support structures with both good SLS-dependent mechanical properties and high porosity was established. Additionally, PCL was shown to retain its cytocompatibility when processed by SLS over a wide range of SLS process parameters. Finally, an interplay of computational and experimental observations was employed to define a stiff and compliant support structure with key features for the *in vivo* application, and specifically: 1) a high porosity (>65%) to reduce the volume of synthetic material compared to the volume of bioactive collagen in the hybrid scaffold; 2) a significant difference in stiffness to evaluate the strain-dependent tissue formation in large bone defects *in vivo*; and 3) fatigue resistance in *in vivo*-like conditions. These support structures were used to produce stiff and compliant hybrid scaffolds, as later described.

4.2 Characterization of stiff and compliant multiscale hybrid scaffolds

Stiff and compliant hybrid scaffolds were produced by including the stiff and compliant support structures, respectively, in the collagen scaffold (Figure 16A). Specifically, the support structures were immersed in a collagen dispersion, which then underwent directional freezing, freeze-drying, and collagen crosslinking [66]. Thus, the production process embedded the support structures in the collagen scaffold with aligned collagen walls by means of physical interlocking. Given the nature of the production process of the hybrid scaffolds, the maintenance of key features of the individual components of the hybrid scaffolds, i.e. the support structures and the collagen scaffolds, needed to be assessed.

The physical presence of the support structures in the collagen dispersion presented the risk of disrupting the directional growth of the ice crystals during the directional freezing

process. This directional growth of the ice crystal determines the final aligned architecture of the collagen walls in the collagen scaffold [66], which in turn is the trigger and the guidance of the endochondral ossification process *in vivo* [33]. Therefore, the maintenance of the aligned architecture of the collagen walls is pivotal to the successful performance of the hybrid scaffolds *in vivo*. The morphology of the collagen walls in the stiff and compliant hybrid scaffolds was assessed by orientation analysis and compared to the one of the collagen scaffolds. Scaffolds were first immersed in fetal bovine serum (FBS) to cause the fibronectin in the serum to adsorb on the collagen walls. Then, the adsorbed fibronectin was visualized by immunohistochemical staining and subsequent immunofluorescent imaging and combined with second harmonic (SH) imaging of the collagen walls. The two imaging methods complement each other, as SH imaging enables the visualization of fibrillar collagen type I [72] within the walls and the adsorbed fibronectin clearly outlines the two surfaces of the collagen walls (Figure 16B, C, and D). Collagen scaffolds were found to have collagen walls predominantly aligned in the axial direction (90°), with a small portion of material in the transversal direction (0° and 180°) (Figure 16E). These results describe a material configuration in which long axial collagen walls are connected by very short transversal collagen bridges and are consistent with previous characterization of the collagen scaffolds [71]. Slightly lower peaks at 90° were measured in the stiff and compliant hybrid scaffolds compared to collagen scaffolds (Figure 16E), indicating a marginally broader distribution of collagen wall orientations. Nonetheless, the results of the orientation analysis revealed no impairment of the collagen wall alignment due to the inclusion of the support structures in the hybrid scaffolds. Consequently, it can be expected that the architecture-dependent *in vivo* endochondral ossification process will be triggered and guided also by the stiff and compliant hybrid scaffolds. It remains to be assessed whether the different stiffness at tissue level of the hybrid scaffolds compared to the collagen scaffolds will have an influence on the establishment of the biological process *in vivo*.

One of the chemicals used to produce the collagen dispersion is acetone, which is a known solvent of PCL [51] and thereby could potentially alter the support structures. Moreover, the growth of ice crystals during the directional freezing process could potentially damage the support structures by generating cracks in the material. Therefore, the mechanical properties of the hybrid scaffolds were tested and compared to the ones of the support structures to exclude any negative influence of the production process on mechanical behavior. Moreover, the stiffness of the hybrid scaffolds was compared to the one of the collagen scaffolds to evaluate whether the inclusion of the support structures achieved the goal of increasing the mechanical competence of the scaffolds at tissue level. Monoaxial compression tests revealed that indeed both stiff and compliant hybrid scaffolds had a higher stiffness than collagen scaffolds, showing an increase of 1102 ± 301 and 2.7 ± 0.5 folds, respectively (Figure 17A). Moreover, no impairment of the stiffness that was engineered for the stiff and compliant support structures was observed in the corresponding hybrid scaffolds after

the production process (Figure 17A). Interestingly, the compliant hybrid scaffold had a stiffness that was 1.8 ± 0.5 folds higher than the one of the compliant support structure. This effect was ascribed to the contribution of collagen densification in between the struts of the support structure during compression, which was not negligible at the order of magnitude of the stiffness of the compliant support structure (10^{-1} N/mm). Nonetheless, no negative influence of the hybrid scaffold production process was observed and the significant difference in stiffness that was engineered between the stiff and compliant support structures was maintained in the hybrid scaffolds. Additionally, the development of hybrid scaffolds succeeded in generating scaffolds with a higher mechanical competence than the collagen scaffolds. Stiff and compliant hybrid scaffolds were tested in the bioreactor to ascertain the absence of possible negative influences of the production process also on their fatigue resistance in *in vivo*-like conditions. Collagen scaffolds were not tested in this case, as their resistance to repeated loading cycles has already been proven [35]. No breakages were recorded for both stiff and compliant hybrid scaffolds and their behavior over one week of continuous mechanical stimulation precisely matched the one observed in the corresponding support structures (Figure 17B). The mechanical characterization of the hybrid scaffolds suggests that there will be no scaffold-dependent hindrances in the observation of strain-dependent differences in tissue formation in large bone defects *in vivo*. Moreover, both stiff and compliant hybrid scaffolds have high chances of maintaining their mechanical stability throughout the healing process. As *in vitro* tests, albeit mimicking multiple aspects of the *in vivo* environment, always represent a simplification compared to the biological situation, the actual stability of the hybrid scaffolds in their intended application remains to be proven.

Finally, the successful establishment of the *in vivo* endochondral ossification process within collagen scaffolds was ascribed, amongst other factors, to the ability of the scaffold to prevalently recruit mesenchymal stromal cells (MSCs) from the bone marrow (i.e. along the aligned porosity of the collagen walls) [33]. Therefore, the preservation of the ease of MSCs migration within hybrid scaffolds was tested by means of an *in vitro* migration assay. The *in vitro* cellular migration within collagen scaffolds has been previously tested by placing the scaffolds onto a confluent 2D cell layer, from which cells could detach to populate the scaffolds during an attachment period [33]. Subsequently, collagen scaffolds were cultured *in vitro* laying sideways to reduce the influence of gravity and, at the end of the evaluation, the distance of the cells from the seeding surface was calculated as cellular migration distance [33]. This migration assay was deemed sub-optimal to evaluate the hybrid scaffolds, as a successful outcome strongly depended on a good contact between scaffold surface and cell-seeded plane, as it was observed in concomitant experiments on different biomaterials (ongoing study at the Julius Wolff Institute). Since the excess collagen surrounding the support structures in the hybrid scaffolds was manually cut, occasional surface irregularities were expected in the hybrid scaffolds, which would negatively influence the results of the migration

assay. Therefore, a novel *in vitro* migration assay was developed to overcome the limitations of the previous one and, at the same time, to model more closely the *in vivo* environment. In fact, the cell source of the novel migration assay was a 3D cell pellet placed directly upon the scaffolds. This setup not only eliminated the issue of surface congruency between scaffolds and cell source, but also mimicked the continuous cell supply from the bone marrow expected in the *in vivo* setting. Also in the novel migration assay, after an initial period of pellet attachment, scaffolds were cultured sideways to reduce the influence of gravity. MSCs migration within stiff and compliant hybrid scaffolds and collagen scaffolds, used as reference, was tested with the novel *in vitro* migration assay over a period of 4 days (Figure 18A, B, and C, respectively). Cellular migration was evaluated as the distance between cells in the scaffolds and the cell pellet. The results of the migration assay showed that the inclusion of the support structures in the hybrid scaffolds did not have any negative influence on MSCs migration within the stiff and compliant hybrid scaffolds compared to the collagen scaffolds (Figure 18D). On the contrary, MSCs migrating within stiff and compliant hybrid scaffolds showed a tendency to migrate further than within hybrid scaffolds, although the results are within the variability of the measurement and are not significantly different. Altogether, stiff and compliant hybrid scaffolds are expected to perform comparably amongst themselves and similarly to the collagen scaffolds in terms of *in vivo* cell recruitment.

In conclusion, stiff and compliant hybrid scaffolds were successfully produced with the intended improvement in mechanical stiffness compared to collagen scaffolds. Moreover, the morphological, mechanical, and biological characterizations of the stiff and compliant hybrid scaffolds proved that the production process did not alter key features pertaining to both the support structures and the collagen scaffolds, and specifically: 1) the mechanical behavior of the support structures in terms of stiffness and fatigue resistance, which will provide mechanical stability at the tissue level throughout the healing process; 2) the aligned collagen walls of the collagen scaffold, which will cause the establishment of the endochondral ossification process *in vivo*; and 3) the ease of cellular migration within the collagen scaffold, which will provide the cellular phenotypes needed for tissue deposition during healing. Stiff and compliant hybrid scaffolds will be implanted in large bone defects in rats to prove or disprove the hypothesis that tissue formation by endochondral ossification can be steered by scaffold-dependent mechanical cues. If the hypothesis will be confirmed, hybrid scaffolds with optimized mechanical and morphological properties could be used to treat both critical size bone defects and osteochondral defects. Therefore, the target mechanical and architectural properties of a scaffold for osteochondral defect healing were investigated by means of computational models.

4.3 Computational evaluation of scaffold influence on osteochondral defect healing

The mechanics-dependent healing of an osteochondral defect and the influence that scaffolds might have on it by means of their mechanical and architectural properties were investigated by computational modelling.

First, an already established model of osteochondral defect healing [60] was further developed to reproduce the typical healing outcome of empty defects. Generally, the healing outcome in this case is the formation of fibrous tissue or fibrocartilage at the articular surface [104,105]. Moreover, the formation of cysts below empty osteochondral defects has been observed in clinical practice [106]. Studies on animal models of empty osteochondral defects similarly reported the growth of fibrous tissue at the articular surface, e.g. in rabbit [21,76], in minipig [59], and in sheep [61], and the formation of cysts below the defects, e.g. in sheep [61] and in goat [107]. Moreover, histological sections in animal studies showed that bone spontaneously grew up to the level of the healthy subchondral bone-cartilage interface [21,59,108]. Bone formation at the side of the defect and concomitantly bone resorption at its base were observed in minipig [59] and goat [107], but not in sheep [108], where bone formed both at the side and at the base of the defect. This difference suggests possible variations in healing pattern depending on the investigated species. However, significant variations in the *in vivo* healing of empty osteochondral defects were observed also amongst subjects equally treated within the same study [21]. Previous computational simulations describing tissue formation in empty osteochondral defects by means of mechanobiological rules were able to reproduce some features of the healing pattern described in clinics and *in vivo*, specifically concerning the formation of fibrous tissue at the articular interface [59,60], bone deposition on the sides and bone resorption at the base of the defect [59], and the spontaneous growth of bone up to the interface with healthy cartilage [59].

In the here presented model, a knee joint featuring an osteochondral defect in the femoral condyle was simplified as an axisymmetric geometry, as previously suggested [60]. MSCs differentiation and cellular mitosis and apoptosis were dependent on a mechanical stimulus computed from strain and fluid velocity in the defect. This formulation of mechanical stimulus has been originally suggested to describe peri-implant tissue formation in bone [10] and since then has been applied to several settings in the musculoskeletal system, e.g. fracture healing in bone [74] and osteochondral defect healing [60]. Although the mechanical stimulus was originally applied to describe only MSCs differentiation [10,60], its use to describe both MSCs differentiation and cellular mitosis and apoptosis has already been suggested in the context of bone healing [74]. By implementing this mechanobiological rule, several of the previously described characteristics of the *in vivo* healing of empty osteochondral defects were reproduced by the here proposed model. In fact, fibrous tissue was predicted to form at the articular interface (Figure 19B and F), while bone deposition and bone resorption happened at

the side and base of the defect, respectively (Figure 19B and D). Moreover, the lateral bone formation was predicted to reach the subchondral bone-cartilage interface of the surrounding healthy tissues (Figure 19B and D) and the area of bone resorption at the central-proximal base of the defect could be compared to the formation of a cyst (Figure 19B and C). Given the consistent similarities in osteochondral defect healing between the here presented model and the *in vivo* observations, the model was deemed appropriate to investigate the influence of scaffold implantation on the healing process.

In vivo tests in sheep [61] and rabbit [62] already aimed at determining the influence of scaffold mechanical properties on the healing of osteochondral defects. However, in both studies, scaffolds that varied in stiffness varied in architecture as well, thereby hampering a clear identification of the influence of the scaffold-dependent mechanical cues on the healing outcome [61]. Computational models have previously been used to study the optimal elastic modulus and permeability of scaffolds to foster the healing of chondral [64] and osteochondral [63] defects. Despite the differences in the investigated defect, i.e. chondral [64] and osteochondral [63], and in the type of model, i.e. 3D patient-specific [64] and axisymmetric [63], both studies concluded that ideal scaffolds should have gradients of properties, and specifically a decreasing elastic modulus and an increasing permeability from the articular surface to the base of the defect. In the case of osteochondral defects, it was suggested that the scaffold elastic modulus should increase again in the bone region [63]. However, in both the cited models, the scaffold was simulated as a uniform material completely filling the defect. Such a scaffold model can well represent hydrogels, but many of the investigated TE scaffolds for osteochondral regeneration have distinct architectural features [20] that are non-negligible in their influence on the mechanical environment. Thus, scaffolds with simple but distinct architectures were implemented here and the influence of both the mechanical and architectural properties of the scaffolds on the healing process was evaluated.

First, a scaffold composed of three vertical struts, which are the axisymmetric representation of three concentric rings, was applied in the defect (Figure 6C). This architecture was chosen because it was expected that the transmission of loads between the articular surface and the proximal base of the defect by means of the vertical struts would avoid the previously observed bone resorption in that region. A systematic variation of elastic modulus of the scaffold material (0.1, 10, and 1000 MPa, corresponding to low, intermediate, and high stiffness scaffold, respectively) was performed to study the influence of scaffold mechanical properties on the healing process. All the values of elastic modulus of scaffold material chosen for the investigation had a parallel in the stiffness of biological tissues and/or of biomaterials used for scaffolds. In fact, the low stiffness scaffold was in the range of granulation tissue (Table 4) and of macroporous scaffolds from synthetic polymers [62]. Macroporous scaffolds from both synthetic [62] and natural [33] polymers can even

have a lower elastic modulus, reaching values in the low kPa range. The intermediate stiffness scaffold had elastic modulus matching the one of cartilage (Table 4). Moreover, biodegradable polymeric scaffolds with elastic modulus of 10s or 100s of MPa have been suggested for the regeneration of osteochondral defects [61,85]. Finally, the high stiffness scaffold had an elastic modulus in the low GPa range, similarly to cancellous bone [42]. The prediction of tissue formation performed in presence of the low stiffness scaffold revealed that this scaffold was too soft to alter the mechanical environment within the defect, thereby resulting in an equivalent healing outcome to the empty defect (Figure 20B). On the contrary, the intermediate stiffness scaffold suppressed bone formation at the base of the defect and further fostered the formation of fibrous tissue at the articular surface and in the middle of the defect (Figure 20D). Interestingly, the high stiffness scaffold supported the formation of cartilage in the defect and the growth of a continuous, albeit thin, layer of bone at its proximal base (Figure 20F). The observations performed with the model found a comparison in literature. In fact, polylactide-co-glycolide (PLGA) scaffolds having an elastic modulus lower than 0.3 MPa were found to result in the growth of fibrous tissue at the articular surface three weeks after implantation in osteochondral defects in rabbit [62]. Moreover, PLGA scaffolds with different elastic modulus of 150 and 95 MPa were tested in osteochondral defects in sheep and more subchondral bone was found in presence of the stiffer scaffold, although no differences in cartilage formation were observed [61].

Subsequently, a scaffold composed of three vertical struts and having biphasic mechanical properties was tested (Figure 6D). The biphasic scaffold mimicked the mechanical properties of the mature tissues whose formation it was meant to support. In fact, the proximal and distal halves of the scaffold, corresponding to the regions of desired bone and cartilage formation, respectively, had elastic moduli of 1000 and 10 MPa, respectively. Scaffolds with gradients of properties have already been proposed in osteochondral TE both in experimental [20,109] and in computational [63,64] studies. Particularly, scaffolds with biphasic properties are developed with the aim of improving both cartilage and bone healing by means of the specific characteristics of each phase [109]. When the biphasic scaffold was implemented in the here studied model, the mechanical properties of its struts helped in developing a strain distribution (Figure 21A) that was analogous to the one observed in the empty osteochondral defect (Figure 19A), with low and high strain in proximal and distal parts of the defect, respectively. Consequently, the biphasic scaffold stimulated a suboptimal mechanics-dependent healing outcome (Figure 21B) that was equivalent to the one of the empty osteochondral defect (Figure 19B), with fibrous tissue at the articular surface and bone resorption at the proximal base of the defect. Therefore, the results of the simulation suggest that the mimicry of the mechanical properties of mature tissues may not be a suitable approach to support the mechanics-dependent tissue formation. However, these observation cannot be supported by comparison with experimental data, as biphasic scaffolds are typically produced by the combination of at least two different

materials [20,109]. Thus, the two phases of the scaffolds stimulate the tissues not only by different mechanical, but also chemical and architectural cues, preventing a clear identification of the mechanics-dependent influence on tissue formation. Consequently, the observations performed by means of the here presented computational model remain to be verified.

Finally, a grid-like scaffold having both vertical and horizontal struts and a high elastic modulus of 1000 MPa was implemented in the defect (Figure 6E). The introduction of the horizontal struts aimed at generating a scaffold with improved mechanical stability by reducing the radial displacement that the knee model underwent as a consequence of the applied compressive load. It was expected that such a reduction in radial displacement would foster the formation of bone. Certainly, the octahedral shear strain within horizontal struts was very low (Figure 21C) and supported the formation of bone (Figure 21D). The grid-like scaffold resulted in the best healing outcome amongst the investigated scaffolds, with cartilage forming in the defect and a quite thick layer of subchondral bone growing at the proximal base of the defect (Figure 21D). Due to the ectopic deposition of bone within the distal strut, the reduced thickness of the subchondral bone layer compared to the healthy tissues, and the lateral formation of fibrous tissue (Figure 21D), the healing outcome supported by the grid-like scaffold was not the ideal one, which would result in the full re-establishment of the pre-injury tissue distributions instead. Nonetheless, these results indicate that mechanical cues to support tissue formation can be defined by both scaffold mechanical and architectural properties and that the optimization of both these aspects may be a strategy to develop improved treatments for osteochondral defects.

Altogether, the computational model here developed to study the mechanics-dependent tissue formation in osteochondral defects indicates that scaffolds having mechanical properties in the range of soft biological tissues (<10 MPa) might not be suitable to foster the mechanics-dependent regeneration of osteochondral defects. On the contrary, scaffolds with stiffness comparable to cancellous bone (low GPa range) and an architecture stable both against compressive and lateral displacements might support a better osteochondral defect healing. These results will be used to produce hybrid scaffolds with specifically optimized properties for the healing of osteochondral defects.

5 Conclusions and recommendation for future work

In conclusion, the work here presented shows the development of a novel multiscale hybrid scaffold with potential therapeutic applications for osteochondral and critical size bone defects depending on its mechanical properties. The hybrid scaffold is composed of a collagen scaffold with aligned architecture and of a PCL support structure with tuneable mechanical and architectural properties.

Each component of the multiscale hybrid scaffold fulfils a precise role. The collagen scaffold is bioactive, in that it induces *in vivo* bone formation by endochondral ossification by means of its aligned architecture. The PCL support structure provides mechanical stability to avoid scaffold deformation and displacement due to external tissue forces and shrinkage due to ECM deposition. The low collagen stiffness at cellular level and the higher support structure stiffness at tissue level determine the multiscale nature of the hybrid scaffold.

The chosen materials and production technique enable the fabrication of a fully resorbable hybrid scaffold, whose mechanical properties at tissue level depend on the precise control of the architecture of the support structure. It is hypothesized that scaffold-dependent mechanical cues can be employed to steer the endochondral ossification process towards either bone or cartilage formation. Stiff and compliant multiscale hybrid scaffolds were developed here to prove or disprove this hypothesis by *in vivo* tests, which are currently performed in a concomitant project at the Julius Wolff Institute.

The here developed computational model of osteochondral defect healing already suggests that scaffold mechanical and architectural properties could be used to influence tissue regeneration. The computational model was used to define target mechanical and architectural properties of scaffolds for the optimal osteochondral defect healing. The results of the simulations suggest that scaffolds with stiffness comparable to cancellous bone and an architecture stable against both compressive and lateral displacements have the potential of supporting osteochondral regeneration, contrary to scaffolds with stiffness in the range of soft biological tissues. Based on these observations, the stiff hybrid scaffold developed in this work might be a promising candidate to support the mechanics-dependent healing of osteochondral defects, as its architecture was optimized to have a reduced lateral displacement when subjected to an axial compressive load. However, the stiffness of the stiff hybrid scaffold would probably need to be increased to reach the stiffness range of cancellous bone, e.g. by an additional optimization of the support structure architecture. Further experimental tests are required to evaluate this concept.

The here presented work has some limitations.

First, the morphological and mechanical properties of the stiff and compliant support structures here developed were optimized for the specific *in vivo* model, i.e. a large

bone defect in rats. In fact, the size of the support structure was adapted in such a way as to be optimally placed on the cortical bone in the defect, while completely exposing the aligned collagen to the bone marrow cavities. Moreover, the fatigue resistance of the support structures was tested by applying the specific loads measured in large bone defects in rats. In a clinical setting, such a precise fitting of architectural and mechanical properties would be hard to achieve. Therefore, the validity of the hybrid scaffold approach will need to be tested in less optimized conditions.

Second, the computational model employed to define the target mechanical and architectural properties of the hybrid scaffolds for osteochondral defect regeneration implemented strong simplifications. In fact, the finite element model of the knee had a simplified axisymmetric geometry compared to the 3D morphology of an actual knee joint. Even the loading scenario had a strongly reduced complexity compared to the *in vivo* one in terms of both type and magnitude of the applied load, here reduced to a pressure with lower magnitude compared to the peak forces experimentally measured in knees. Cellular behavior was subjected to simplifications as well. In fact, MSCs migration was simulated as a passive diffusion process as opposed to an active migration behavior, which would have been also influenced by the properties of the scaffolds in terms of stiffness, surface topology, and porosity. Moreover, the assumption that cells would produce their corresponding tissue proportionally to their number does not represent the features of tissues with low cellularity, such as cartilage. Finally, the model did not allow the simulation of the active tissue remodeling of the tissues surrounding the osteochondral defect.

Future work should focus on the *in vivo* evaluation of the scaffold-dependent tissue formation in large bone defects in a pre-clinical animal model (e.g. in rat), specifically observing whether stiff and compliant hybrid scaffolds induce the growth of different amounts of cartilage and bone. This knowledge could, then, be used to design clinical devices with optimized mechanical properties to support the healing of wounds in the bone or cartilage tissues.

Moreover, the results of the here proposed computational model can be used to develop a prototype of a hybrid scaffold with optimized mechanical and architectural properties specifically targeted to the healing of osteochondral defects. Of course, such prototype will need to first undergo testing in *in vitro* conditions.

The computational model of osteochondral defect healing with scaffolds can also be used to evaluate the consequences of scaffold degradation on the healing process. Finally, some of the simplifications of the computational model could be addressed to bring the model closer to the *in vivo* scenario, e.g. loading, active cellular migration, and 3D environment.

6 Acknowledgments

My deepest gratitude goes to Doctor Ansgar Petersen and Professor Sara Checa for their constant guidance and support throughout the doctoral project.

I thank Professor Georg N. Duda and Professor Manfred Zehn for their supervision.

A big thank goes also to all the members of the ECHO team, who created a friendly and efficient working environment. Specifically, I thank Christoph Gayer, who produced the support structures, and Hans Leemhuis, who produced the hybrid scaffolds and the collagen scaffolds.

I thank Alessandro Torchio and Doctor Monica Boffito, who performed the measurement of the molecular weight, as well as Professor Gianluca Ciardelli for his support.

All the members of the “Cellular Biomechanics and Biomaterials” and “Computational Mechanobiology” groups at the Julius Wolff Institute generated a stimulating atmosphere at work and were supportive and helpful. I express my gratitude in particular to Aaron Herrera, Edoardo Borgiani, Erik Brauer, and Sophie Görlitz, who helped me moving the first steps in the new research topic and were always available to scientific discussions or simply to answer questions.

I thank all the people that manage the laboratories and take care of the technical issues for their availability and support in solving the problems that I presented them along the way. I especially thank Simone Cho for performing the measurements of cellular number and metabolic activity during the cytocompatibility tests.

I’m grateful to the admin teams of the Julius Wolff Institute and the Berlin-Brandenburg School for Regenerative Therapies, who were always extremely efficient and helpful.

Last but not least, a huge thank to my family and (old and new) friends, who always supported me.

References

[1] R. Florencio-Silva, G. Rodriguez da Silva Sasso, E. Sasso-Cerri, M.J. Simoes, P.S. Cerri, Biology of Bone Tissue: Structure, Function, and Factors That Influence Bone Cells, Biomed Res. Int. (2015). https://doi.org/10.1016/S0923-2532(05)80182-6.

[2] S.L. Dallas, M. Prideaux, L.F. Bonewald, The osteocyte: An endocrine cell . . . and more, Endocr. Rev. 34 (2013) 658–690. https://doi.org/10.1210/er.2012-1026.

[3] E.J. Sheehy, D.J. Kelly, F.J. O'Brien, Biomaterial-based endochondral bone regeneration: a shift from traditional tissue engineering paradigms to developmentally inspired strategies, Mater. Today Bio. 3 (2019) 100009. https://doi.org/10.1016/j.mtbio.2019.100009.

[4] E. Kheir, D. Shaw, Hyaline articular cartilage, Orthop. Trauma. 23 (2009) 450–455. https://doi.org/10.1016/j.mporth.2009.01.003.

[5] T.A. Einhorn, The cell and molecular biology of fracture healing, Clin. Orthop. Relat. Res. (1998) 7–21. https://doi.org/10.1097/00003086-199810001-00003.

[6] L.E. Claes, K. Eckert-Huebner, P. Augat, The effect of mechanical stability on local vascularization and tissue differentiation in callus healing, J. Orthop. Res. 20 (2002) 1099–1105. https://doi.org/10.1016/S0736-0266(02)00044-X.

[7] E.F. Morgan, K.T. Salisbury Palomares, R.E. Gleason, D.L. Bellin, K.B. Chien, G.U. Unnikrishnan, P.L. Leong, Correlations between local strains and tissue phenotypes in an experimental model of skeletal healing, J. Biomech. 43 (2010) 2418–2424. https://doi.org/10.1016/j.jbiomech.2010.04.019.

[8] R.M. Delaine-Smith, G.C. Reilly, Mesenchymal stem cell responses to mechanical stimuli., Muscles. Ligaments Tendons J. 2 (2012) 169–80. http://www.ncbi.nlm.nih.gov/pmc/articles/PMC3666521/%5Cnhttp://www.ncbi.nlm.nih.gov/pubmed/3666521%5Cnhttp://www.pubmedcentral.nih.gov/articlerender.fcgi?artid=3666521&tool=pmcentrez&rendertype=abstract.

[9] E. Michalopoulos, R.L. Knight, S. Korossis, J.N. Kearney, J.P. Fisher, E. Ingham, Development of Methods for Studying the Differentiation of Human Mesenchymal Stem Cells Under Cyclic Compressive Strain, Tissue Eng. Part C Methods. 18 (2012) 252–262. https://doi.org/10.1089/ten.tec.2011.0347.

[10] P.J. Prendergast, R. Huiskes, K. Søballe, Biophysical stimuli on cells during tissue differentiation at implant interfaces, J. Biomech. 30 (1997) 539–548. https://doi.org/10.1016/S0021-9290(96)00140-6.

[11] L.E. Claes, C.A. Heigele, Magnitudes of local stress and strain along bony surfaces predict the course and type of fracture healing, J. Biomech. 32 (1999) 255–266. https://doi.org/10.1016/S0021-9290(98)00153-5.

[12] V. Glatt, C.H. Evans, K. Tetsworth, A concert between biology and biomechanics: The influence of the mechanical environment on bone healing, Front. Physiol. 7 (2017) 1–18. https://doi.org/10.3389/fphys.2016.00678.

[13] E.M. Thompson, A. Matsiko, E. Farrell, D.J. Kelly, F.J. O'Brien, Recapitulating

endochondral ossification: a promising route to in vivo bone regeneration, J. Tissue Eng. Regen. Med. 9 (2015) 889–902. https://doi.org/10.1002/term.1918.

[14] E.B. Hunziker, Mechanism of longitudinal bone growth and its regulation by growth plate chondrocytes, Microsc. Res. Tech. 28 (1994) 505–519. https://doi.org/10.1002/jemt.1070280606.

[15] D.W. Sanders, M. Bhandari, G. Guyatt, D. Heels-Ansdell, E.H. Schemitsch, M. Swiontkowski, P. Tornetta, S. Walter, Critical-Sized Defect in the Tibia: Is it Critical? Results From the SPRINT Trial, J. Orthop. Trauma. 28 (2014) 632–635. https://doi.org/10.1097/BOT.0000000000000194.

[16] E.H. Schemitsch, Size Matters: Defining Critical in Bone Defect Size!, J. Orthop. Trauma. 31 (2017) S20–S22. https://doi.org/10.1097/BOT.0000000000000978.

[17] A. Nauth, M.D. McKee, T.A. Einhorn, J.T. Watson, R. Li, E.H. Schemitsch, Managing bone defects, J. Orthop. Trauma. 25 (2011) 462–466. https://doi.org/10.1097/BOT.0b013e318224caf0.

[18] S. Bose, M. Roy, A. Bandyopadhyay, Recent advances in bone tissue engineering scaffolds, Trends Biotechnol. 30 (2012) 546–554. https://doi.org/10.1016/j.tibtech.2012.07.005.

[19] E.B. Hunziker, K. Lippuner, M.J.B. Keel, N. Shintani, An educational review of cartilage repair: Precepts & practice - myths & misconceptions - progress & prospects, Osteoarthr. Cartil. 23 (2015) 334–350. https://doi.org/10.1016/j.joca.2014.12.011.

[20] S.P. Nukavarapu, D.L. Dorcemus, Osteochondral tissue engineering: Current strategies and challenges, Biotechnol. Adv. 31 (2013) 706–721. https://doi.org/10.1016/j.biotechadv.2012.11.004.

[21] T. Furukawa, D.R. Eyre, S. Koide, M.J. Glimcher, Biochemical studies on repair cartilage resurfacing experimental defects in the rabbit knee, J. Bone Jt. Surg. 62-A (1980) 1–11.

[22] R. Langer, J.P. Vacanti, Tissue Engineering, Science (80-.). 260 (1993) 920–926. https://doi.org/10.1126/science.8493529.

[23] D. Sengupta, S.D. Waldman, S. Li, From in vitro to in situ tissue engineering, Ann. Biomed. Eng. 42 (2014) 1537–1545. https://doi.org/10.1007/s10439-014-1022-8.

[24] M.. Murdock, S.F. Badylak, Biomaterials-based in situ tissue engineering, Curr. Opin. Biomed. Eng. (2017). https://doi.org/10.1016/j.cobme.2017.01.001.Biomaterials-based.

[25] G.F. Muschler, C. Nakamoto, L.G. Griffith, Engineering principles of clinical cell-based tissue engineering, J. Bone Jt. Surg. - Ser. A. 86 (2004) 1541–1558. https://doi.org/10.2106/00004623-200407000-00029.

[26] T.H. Qazi, D.J. Mooney, M. Pumberger, S. Geißler, G.N. Duda, Biomaterials based strategies for skeletal muscle tissue engineering: Existing technologies and future trends, Biomaterials. 53 (2015) 502–521. https://doi.org/10.1016/j.biomaterials.2015.02.110.

[27] L.L. Hench, J.M. Polak, Third-generation biomedical materials., Science. 295 (2002) 1014–1017. https://doi.org/10.1126/science.1067404.

[28] K.M. Galler, A. Eidt, G. Schmalz, Cell-free approaches for dental pulp tissue engineering, J. Endod. 40 (2014) S41–S45. https://doi.org/10.1016/j.joen.2014.01.014.

[29] T.B. Wissing, V. Bonito, C.V.C. Bouten, A.I.P.M. Smits, Biomaterial-driven in situ cardiovascular tissue engineering—a multi-disciplinary perspective, Npj Regen. Med. 2 (2017) 1–19. https://doi.org/10.1038/s41536-017-0023-2.

[30] E.M. Bueno, J. Glowacki, Cell-free and cell-based approaches for bone regeneration, Nat. Rev. Rheumatol. 5 (2009) 685–697. https://doi.org/10.1038/nrrheum.2009.228.

[31] W.S. Toh, M. Spector, E.H. Lee, T. Cao, Biomaterial-mediated delivery of microenvironmental cues for repair and regeneration of articular cartilage, Mol. Pharm. 8 (2011) 994–1001. https://doi.org/10.1021/mp100437a.

[32] I.K. Ko, S.J. Lee, A. Atala, J.J. Yoo, In situ tissue regeneration through host stem cell recruitment, Exp. Mol. Med. 45 (2013). https://doi.org/10.1038/emm.2013.118.

[33] A. Petersen, A. Princ, G. Korus, A. Ellinghaus, H. Leemhuis, A. Herrera, A. Klaumünzer, S. Schreivogel, A. Woloszyk, K. Schmidt-Bleek, S. Geissler, I. Heschel, G.N. Duda, A biomaterial with a channel-like pore architecture induces endochondral healing of bone defects, Nat. Commun. (2018). https://doi.org/10.1038/s41467-018-06504-7.

[34] P. Lenas, M. Moos, F.P. Luyten, Developmental engineering: A new paradigm for the design and manufacturing of cell-based products. Part I: From three-dimensional cell growth to biomimetics of in Vivo development, Tissue Eng. - Part B Rev. 15 (2009) 381–394. https://doi.org/10.1089/ten.teb.2008.0575.

[35] E. Brauer, E. Lippens, O. Klein, G. Nebrich, S. Schreivogel, G. Korus, G.N. Duda, A. Petersen, Collagen Fibrils Mechanically Contribute to Tissue Contraction in an In Vitro Wound Healing Scenario, Adv. Sci. 6 (2019). https://doi.org/10.1002/advs.201801780.

[36] S. Abdulghani, G.R. Mitchell, Biomaterials for in situ tissue regeneration: A review, Biomolecules. 9 (2019). https://doi.org/10.3390/biom9110750.

[37] D. Zhang, X. Wu, J. Chen, K. Lin, The development of collagen based composite scaffolds for bone regeneration, Bioact. Mater. 3 (2018) 129–138. https://doi.org/10.1016/j.bioactmat.2017.08.004.

[38] D.W. Weisgerber, K. Erning, C.L. Flanagan, S.J. Hollister, B.A.C. Harley, Evaluation of multi-scale mineralized collagen-polycaprolactone composites for bone tissue engineering, J. Mech. Behav. Biomed. Mater. 61 (2016) 318–327. https://doi.org/10.1016/j.jmbbm.2016.03.032.

[39] F. Fahimipour, E. Dashtimoghadam, M. Rasoulianboroujeni, M. Yazdimamaghani, K. Khoshroo, M. Tahriri, A. Yadegari, J.A. Gonzalez, D. Vashaee, D.C. Lobner, T.S. Jafarzadeh Kashi, L. Tayebi, Collagenous matrix supported by a 3D-printed

scaffold for osteogenic differentiation of dental pulp cells, Dent. Mater. (2017) 1–12. https://doi.org/10.1016/j.dental.2017.10.001.

[40] J. Wang, D. Wu, Z. Zhang, J. Li, Y. Shen, Z. Wang, Y. Li, Z.Y. Zhang, J. Sun, Biomimetically Ornamented Rapid Prototyping Fabrication of an Apatite-Collagen-Polycaprolactone Composite Construct with Nano-Micro-Macro Hierarchical Structure for Large Bone Defect Treatment, ACS Appl. Mater. Interfaces. 7 (2015) 26244–26256. https://doi.org/10.1021/acsami.5b08534.

[41] D.F. Williams, On the mechanisms of biocompatibility, Biomaterials. 29 (2008) 2941–2953. https://doi.org/10.1016/j.biomaterials.2008.04.023.

[42] S. Bose, M. Roy, A. Bandyopadhyay, Recent advances in bone tissue engineering scaffolds, Trends Biotechnol. 30 (2012) 546–554. https://doi.org/10.1016/j.tibtech.2012.07.005.

[43] J. Rouwkema, N.C. Rivron, C.A. van Blitterswijk, Vascularization in tissue engineering, Trends Biotechnol. 26 (2008) 434–441. https://doi.org/10.1016/j.tibtech.2008.04.009.

[44] R.D. Goodridge, C.J. Tuck, R.J.M. Hague, Laser sintering of polyamides and other polymers, Prog. Mater. Sci. 57 (2012) 229–267. https://doi.org/10.1016/j.pmatsci.2011.04.001.

[45] H.N. Chia, B.M. Wu, Recent advances in 3D printing of biomaterials, J. Biol. Eng. 9 (2015) 4. https://doi.org/10.1186/s13036-015-0001-4.

[46] A. Mazzoli, Selective laser sintering in biomedical engineering, Med. Biol. Eng. Comput. 51 (2013) 245–256. https://doi.org/10.1007/s11517-012-1001-x.

[47] D.L. Bourell, T.J. Watt, D.K. Leigh, B. Fulcher, Performance limitations in polymer laser sintering, Phys. Procedia. 56 (2014) 147–156. https://doi.org/10.1016/j.phpro.2014.08.157.

[48] Oerlikon Management AG, AM Polymer, (2020). https://www.oerlikon.com/am/en/technologies/am-polymer/#31831 (accessed August 14, 2020).

[49] C.C. Chu, Materials for absorbable and nonabsorbable surgical sutures, Woodhead Publishing Limited, 2013. https://doi.org/10.1533/9780857095602.2.275.

[50] S.F.S. Shirazi, S. Gharehkhani, M. Mehrali, H. Yarmand, H.S.C. Metselaar, N. Adib Kadri, N.A.A. Osman, A review on powder-based additive manufacturing for tissue engineering: selective laser sintering and inkjet 3D printing, Sci. Technol. Adv. Mater. 16 (2015) 033502. https://doi.org/10.1088/1468-6996/16/3/033502.

[51] M.A. Woodruff, D.W. Hutmacher, The return of a forgotten polymer - Polycaprolactone in the 21st century, Prog. Polym. Sci. 35 (2010) 1217–1256. https://doi.org/10.1016/j.progpolymsci.2010.04.002.

[52] J.M. Williams, A. Adewunmi, R.M. Schek, C.L. Flanagan, P.H. Krebsbach, S.E. Feinberg, S.J. Hollister, S. Das, Bone tissue engineering using polycaprolactone scaffolds fabricated via selective laser sintering, Biomaterials. 26 (2005) 4817–

4827. https://doi.org/10.1016/j.biomaterials.2004.11.057.

[53] D.A. Zopf, A.G. Mitsak, C.L. Flanagan, M. Wheeler, G.E. Green, S.J. Hollister, Computer aided-designed, 3-dimensionally printed porous tissue bioscaffolds for craniofacial soft tissue reconstruction, Otolaryngol. - Head Neck Surg. (United States). 152 (2015) 57–62. https://doi.org/10.1177/0194599814552065.

[54] K.H. Tan, C.K. Chua, K.F. Leong, C.M. Cheah, W.S. Gui, W.S. Tan, F.E. Wiria, Selective laser sintering of biocompatible polymers for applications in tissue engineering, Biomed. Mater. Eng. 15 (2005) 113–124.

[55] S. Lohfeld, M.A. Tyndyk, S. Cahill, N. Flaherty, V. Barron, P.E. McHugh, A method to fabricate small features on scaffolds for tissue engineering via selective laser sintering, J. Biomed. Sci. Eng. 03 (2010) 138–147. https://doi.org/10.4236/jbise.2010.32019.

[56] K.F. Leong, C.K. Chua, W.S. Gui, Verani, Building porous biopolymeric microstructures for controlled drug delivery devices using selective laser sintering, Int. J. Adv. Manuf. Technol. 31 (2006) 483–489. https://doi.org/10.1007/s00170-005-0217-4.

[57] B. Partee, S.J. Hollister, S. Das, Selective Laser Sintering Process Optimization for Layered Manufacturing of CAPA[sup ®] 6501 Polycaprolactone Bone Tissue Engineering Scaffolds, J. Manuf. Sci. Eng. 128 (2006) 531. https://doi.org/10.1115/1.2162589.

[58] M.S. Ghiasi, J. Chen, A. Vaziri, E.K. Rodriguez, A. Nazarian, Bone fracture healing in mechanobiological modeling: A review of principles and methods, Bone Reports. 6 (2017) 87–100. https://doi.org/10.1016/j.bonr.2017.03.002.

[59] G.N. Duda, Z.M. Maldonado, P. Klein, M.O.W. Heller, J. Burns, H.J. Bail, On the influence of mechanical conditions in osteochondral defect healing, J. Biomech. 38 (2005) 843–851. https://doi.org/10.1016/j.jbiomech.2004.04.034.

[60] D.J. Kelly, P.J. Prendergast, Mechano-regulation of stem cell differentiation and tissue regeneration in osteochondral defects, J. Biomech. 38 (2005) 1413–1422. https://doi.org/10.1016/j.jbiomech.2004.06.026.

[61] K. Schlichting, H. Schell, R.U. Kleemann, A. Schill, A. Weiler, G.N. Duda, D.R. Epari, Influence of scaffold stiffness on subchondral bone and subsequent cartilage regeneration in an ovine model of osteochondral defect healing, Am. J. Sports Med. 36 (2008) 2379–2391. https://doi.org/10.1177/0363546508322899.

[62] R. Ikeda, H. Fujioka, I. Nagura, T. Kokubu, N. Toyokawa, A. Inui, T. Makino, H. Kaneko, M. Doita, M. Kurosaka, The effect of porosity and mechanical property of a synthetic polymer scaffold on repair of osteochondral defects, Int. Orthop. 33 (2009) 821–828. https://doi.org/10.1007/s00264-008-0532-0.

[63] D.J. Kelly, P.J. Prendergast, Prediction of the optimal mechanical properties for a scaffold used in osteochondral defect repair., Tissue Eng. 12 (2006) 2509–2519. https://doi.org/10.1089/ten.2006.12.ft-202.

[64] Y.G. Koh, J.A. Lee, Y.S. Kim, H.Y. Lee, H.J. Kim, K.T. Kang, Optimal mechanical properties of a scaffold for cartilage regeneration using finite element analysis, J.

Tissue Eng. 10 (2019). https://doi.org/10.1177/2041731419832133.

[65] Creative Commons Attribution 4.0 International (CC BY 4.0), (n.d.). https://creativecommons.org/licenses/by/4.0/ (accessed January 12, 2021).

[66] H. Schoof, J. Apel, I. Heschel, G. Rau, Control of pore structure and size in freeze-dried collagen sponges, J. Biomed. Mater. Res. 58 (2001) 352–357. https://doi.org/10.1002/jbm.1028.

[67] M. Boffito, C. Pontremoli, S. Fiorilli, R. Laurano, G. Ciardelli, C. Vitale-Brovarone, Injectable thermosensitive formulation based on polyurethane hydrogel/mesoporous glasses for sustained co-delivery of functional ions and drugs, Pharmaceutics. 11 (2019). https://doi.org/10.3390/pharmaceutics11100501.

[68] A. Hassan, N.A. Rahman, R. Yahya, Moisture absorption effect on thermal, dynamic mechanical and mechanical properties of injection-molded short glass-fiber/polyamide 6,6 composites, Fibers Polym. 13 (2012) 899–906. https://doi.org/10.1007/s12221-012-0899-9.

[69] A. Petersen, P. Joly, C. Bergmann, G. Korus, G.N. Duda, The Impact of Substrate Stiffness and Mechanical Loading on Fibroblast-Induced Scaffold Remodeling, Tissue Eng. Part A. 18 (2012) 1804–1817. https://doi.org/10.1089/ten.tea.2011.0514.

[70] J. Schindelin, I. Arganda-Carreras, E. Frise, V. Kaynig, M. Longair, T. Pietzsch, S. Preibisch, C. Rueden, S. Saalfeld, B. Schmid, J.Y. Tinevez, D.J. White, V. Hartenstein, K. Eliceiri, P. Tomancak, A. Cardona, Fiji: An open-source platform for biological-image analysis, Nat. Methods. 9 (2012) 676–682. https://doi.org/10.1038/nmeth.2019.

[71] A. Herrera, J. Hellwig, H. Leemhuis, R. von Klitzing, I. Heschel, G.N. Duda, A. Petersen, From macroscopic mechanics to cell-effective stiffness within highly aligned macroporous collagen scaffolds, Mater. Sci. Eng. C. 103 (2019) 109760. https://doi.org/10.1016/j.msec.2019.109760.

[72] X. Chen, O. Nadiarynkh, S. Plotnikov, P.J. Campagnola, Second harmonic generation microscopy for quantitative analysis of collagen fibrillar structure, Nat. Protoc. 7 (2012) 654–669. https://doi.org/10.1038/nprot.2012.009.

[73] E. Fonck, G.G. Feigl, J. Fasel, D. Sage, M. Unser, D.A. Rüfenacht, N. Stergiopulos, Effect of aging on elastin functionality in human cerebral arteries, Stroke. 40 (2009) 2552–2556. https://doi.org/10.1161/STROKEAHA.108.528091.

[74] S. Checa, P.J. Prendergast, G.N. Duda, Inter-species investigation of the mechano-regulation of bone healing: Comparison of secondary bone healing in sheep and rat, J. Biomech. 44 (2011) 1237–1245. https://doi.org/10.1016/j.jbiomech.2011.02.074.

[75] M. Tortorici, A. Petersen, K. Ehrhart, G.N. Duda, S. Checa, Scaffold-Dependent Mechanical and Architectural Cues Guide Osteochondral Defect Healing in silico, Front. Bioeng. Biotechnol. 9 (2021). https://doi.org/https://doi.org/10.3389/fbioe.2021.642217.

[76] F. Shapiro, S. Koide, M.J. Glimcher, Cell Origin and Differentiation in the Repair of Full-Thickness Defects of Articular Cartilage, J. Bone Jt. Surg. (1993) 532–553.

[77] M. Tortorici, C. Gayer, A. Torchio, S. Cho, J.H. Schleifenbaum, A. Petersen, Inner strut morphology is the key parameter in producing highly porous and mechanically stable poly (ε -caprolactone) scaffolds via selective laser sintering, Mater. Sci. Eng. C. 123 (2021) 111986. https://doi.org/10.1016/j.msec.2021.111986.

[78] L.G. Bracaglia, B.T. Smith, E. Watson, N. Arumugasaamy, A.G. Mikos, J.P. Fisher, 3D printing for the design and fabrication of polymer-based gradient scaffolds, Acta Biomater. 56 (2017) 3–13. https://doi.org/10.1016/j.actbio.2017.03.030.

[79] D.T. Reilly, A.H. Burstein, V.H. Frankel, The elastic modulus for bone, J. Biomech. 7 (1974). https://doi.org/10.1016/0021-9290(74)90018-9.

[80] P.L. Mente, J.L. Lewis, Elastic modulus of calcified cartilage is an order of magnitude less than that of subchondral bone, J. Orthop. Res. 12 (1994) 637–647. https://doi.org/10.1002/jor.1100120506.

[81] S. Treppo, H. Koepp, E.C. Quan, A.A. Cole, K.E. Kuettner, A.J. Grodzinsky, Comparison of biomechanical and biochemical properties of cartilage from human knee and ankle pairs, J. Orthop. Res. 18 (2000) 739–748. https://doi.org/10.1002/jor.1100180510.

[82] F.H. Silver, G. Bradica, A. Tria, Elastic energy storage in human articular cartilage: Estimation of the elastic modulus for type II collagen and changes associated with osteoarthritis, Matrix Biol. 21 (2002) 129–137. https://doi.org/10.1016/S0945-053X(01)00195-0.

[83] S. Eshraghi, S. Das, Micromechanical finite-element modeling and experimental characterization of the compressive mechanical properties of polycaprolactone-hydroxyapatite composite scaffolds prepared by selective laser sintering for bone tissue engineering, Acta Biomater. 8 (2012) 3138–3143. https://doi.org/10.1016/j.actbio.2012.04.022.

[84] S. Eshraghi, S. Das, Mechanical & Microstructural Properties of PCL Scaffolds with 1-D, 2-D & 3-D Orthogonally Oriented Porous Architectures Produced by Selective Laser Sintering, Acta Biomater. 6 (2011) 2467–2476. https://doi.org/10.1016/j.actbio.2010.02.002.Mechanical.

[85] A. Di Luca, A. Longoni, G. Criscenti, I. Lorenzo-Moldero, M. Klein-Gunnewiek, J. Vancso, C. Van Blitterswijk, C. Mota, L. Moroni, Surface energy and stiffness discrete gradients in additive manufactured scaffolds for osteochondral regeneration, Biofabrication. 8 (2016). https://doi.org/10.1088/1758-5090/8/1/015014.

[86] A. D Olubamiji, Z. Izadifar, J.L. Si, D.M.L. Cooper, F. Eames, D.X.B. Chen, Modulating mechanical behaviour of 3D-printed cartilage-mimetic PCL scaffolds : influence of molecular weight and pore geometry, Biofabrication. (2016).

[87] J.Y. Rho, R.B. Ashman, C.H. Turner, Young's modulus of trabecular and cortical bone material: Ultrasonic and microtensile measurements, J. Biomech. 26 (1993) 111–119. https://doi.org/10.1016/0021-9290(93)90042-D.

[88] R. Nunes, J. Martin, J. Johnson, Influence of molecular weight and molecular weight distribution on mechanical properties of polymers, Polym. Eng. Sci. 22 (1982) 205–228. https://doi.org/10.1002/pen.760220402.

[89] C.T. Bellehumeur, M.K. Bisaria, J. Vlachopoulos, An experimental study and model assessment of polymer sintering, Polym. Eng. Sci. 36 (1996) 2198–2207. https://doi.org/10.1002/pen.10617.

[90] C. Gayer, J. Ritter, M. Bullemer, S. Grom, L. Jauer, W. Meiners, A. Pfister, F. Reinauer, M. Vučak, K. Wissenbach, H. Fischer, R. Poprawe, J.H. Schleifenbaum, Development of a solvent-free polylactide/calcium carbonate composite for selective laser sintering of bone tissue engineering scaffolds, Mater. Sci. Eng. C. 101 (2019) 660–673. https://doi.org/10.1016/j.msec.2019.03.101.

[91] F. Tuba, L. Oláh, P. Nagy, Towards the understanding of the molecular weight dependence of essential work of fracture in semi-crystalline polymers: A study on poly(ε-caprolactone), Express Polym. Lett. 8 (2014) 869–879. https://doi.org/10.3144/expresspolymlett.2014.88.

[92] J.K. Prescott, R.A. Barnum, On powder flowability, Pharm. Technol. 24 (2000) 60-84+236.

[93] B. Trathnigg, Size-Exclusion Chromatography of Polymers, in: R.A. Meyers (Ed.), Encycl. Anal. Chem., John Wiley & Sons, Ltd, Chichester, UK, 2006: pp. 8008–8034. https://doi.org/10.1002/9780470027318.a2032.

[94] L.A. Bosworth, A. Gibb, S. Downes, Gamma irradiation of electrospun poly(ε-caprolactone) fibers affects material properties but not cell response, J. Polym. Sci. Part B Polym. Phys. 50 (2012) 870–876. https://doi.org/10.1002/polb.23072.

[95] R. Augustine, A. Saha, V.P. Jayachandran, S. Thomas, N. Kalarikkal, Dose-dependent effects of gamma irradiation on the materials properties and cell proliferation of electrospun polycaprolactone tissue engineering scaffolds, Int. J. Polym. Mater. Polym. Biomater. 64 (2015) 526–533. https://doi.org/10.1080/00914037.2014.977900.

[96] E. Cottam, D.W.L. Hukins, K. Lee, C. Hewitt, M.J. Jenkins, Effect of sterilisation by gamma irradiation on the ability of polycaprolactone (PCL) to act as a scaffold material, Med. Eng. Phys. 31 (2009) 221–226. https://doi.org/10.1016/j.medengphy.2008.07.005.

[97] H. Sun, L. Mei, C. Song, X. Cui, P. Wang, The in vivo degradation, absorption and excretion of PCL-based implant, Biomaterials. 27 (2006) 1735–1740. https://doi.org/10.1016/j.biomaterials.2005.09.019.

[98] S.C. Woodward, P.S. Brewer, F. Moatamed, A. Schindler, C.G. Pitt, The intracellular degradation of poly(ε-caprolactone), J. Biomed. Mater. Res. 19 (1985) 437–444. https://doi.org/10.1002/jbm.820190408.

[99] B.E. Franco, J. Ma, B. Loveall, G.A. Tapia, K. Karayagiz, J. Liu, A. Elwany, R. Arroyave, I. Karaman, A Sensory Material Approach for Reducing Variability in Additively Manufactured Metal Parts, Sci. Rep. 7 (2017) 1–12. https://doi.org/10.1038/s41598-017-03499-x.

[100] N. Sudarmadji, J.Y. Tan, K.F. Leong, C.K. Chua, Y.T. Loh, Investigation of the mechanical properties and porosity relationships in selective laser-sintered polyhedral for functionally graded scaffolds, Acta Biomater. 7 (2011) 530–537. https://doi.org/10.1016/j.actbio.2010.09.024.

[101] V.J. Challis, A.P. Roberts, J.F. Grotowski, L.C. Zhang, T.B. Sercombe, Prototypes for bone implant scaffolds designed via topology optimization and manufactured by solid freeform fabrication, Adv. Eng. Mater. 12 (2010) 1106–1110. https://doi.org/10.1002/adem.201000154.

[102] H. Kang, C.Y. Lin, S.J. Hollister, Topology optimization of three dimensional tissue engineering scaffold architectures for prescribed bulk modulus and diffusivity, Struct. Multidiscip. Optim. 42 (2010) 633–644. https://doi.org/10.1007/s00158-010-0508-8.

[103] J.C. Middleton, A.J. Tipton, Synthetic biodegradable polymers as orthopedic devices., Biomaterials. 21 (2000) 2335–2346. https://doi.org/10.1016/S0142-9612(00)00101-0.

[104] E. Solheim, J. Hegna, E. Inderhaug, Long-Term Survival after Microfracture and Mosaicplasty for Knee Articular Cartilage Repair: A Comparative Study Between Two Treatments Cohorts, Cartilage. (2018). https://doi.org/10.1177/1947603518783482.

[105] E. Solheim, J. Hegna, T. Strand, T. Harlem, E. Inderhaug, Randomized Study of Long-term (15-17 Years) Outcome After Microfracture Versus Mosaicplasty in Knee Articular Cartilage Defects, Am. J. Sports Med. 46 (2018) 826–831. https://doi.org/10.1177/0363546517745281.

[106] V. Valderrabano, A. Leumann, H. Rasch, T. Egelhof, B. Hintermann, G. Pagenstert, Knee-to-Ankle Mosaicplasty for the Treatment of Osteochondral Lesions of the Ankle Joint, Am. J. Sports Med. 37 (2009) 105S-111S. https://doi.org/10.1177/0363546509351481.

[107] D.W. Jackson, P.A. Lalor, H.M. Aberman, T.M. Simon, Spontaneous repair of full-thickness defects of articular cartilage in a goat model, J Bone Jt. Surg. 23-A (2001) 53–64.

[108] H. Lydon, A. Getgood, F.M.D. Henson, Healing of Osteochondral Defects via Endochondral Ossification in an Ovine Model, Cartilage. 10 (2019) 94–101. https://doi.org/10.1177/1947603517713818.

[109] R. Longley, A.M. Ferreira, P. Gentile, Recent approaches to the manufacturing of biomimetic multi-phasic scaffolds for osteochondral regeneration, Int. J. Mol. Sci. 19 (2018). https://doi.org/10.3390/ijms19061755.

Appendices

A. Immunofluorescent staining protocols

A.1. Reagents and buffers

Table A.1-1: Reagents and buffers.

Reagent	Company	Catalog number
Normal donkey serum (NDS)	Jackson ImmunoResearch Europe Ltd, Ely, UK	017-000-121
Antibody diluent with Background-Reducing Components (Ant-dil)	DAKO, Agilent Technologies, Inc., USA	S3022
Anti-fibronectin antibody made in rabbit	Abcam plc, Cambridge, UK	ab23750
Alexa FluorTM 555 donkey anti-rabbit (Alexa Fluor 555 dαr)	Thermo Fisher, MA, USA	A31572
Alexa FluorTM 488 phalloidin (Ph-488)	Thermo Fisher, MA, USA	A12379
4',6-Diamidino-2-Phenylindole, Dihydrochloride (DAPI)	Thermo Fisher, MA, USA	D1306
AMPUWA water	Fresenius Kabi AG, Bad Homburg, Germany	7151-5
Triton X-100 (Triton)	Sigma-Aldrich GmbH, Munich, Germany	T8787
Bovine serum albumin (BSA)	Sigma-Aldrich GmbH, Munich, Germany	A7906
Trizma hydrochloride	Sigma-Aldrich GmbH, Munich, Germany	T3253
Trizma base	Sigma-Aldrich GmbH, Munich, Germany	T6066
Sodium chloride (NaCl)	Merck & Co., Inc. NJ, USA	106.392
Tris-buffered saline (TBS): 42 mM of Trizma hydrochloride, 7.4 mM Trizma base and 150 mM NaCl in AMPUWA water		

A.2. Fibronectin

Table A.2-1. Anti-fibronectin staining. RT: room temperature.

Step	Composition	Time	Temperature
Permeabilization	0.025 % Triton / TBS (pH 8.2)	3x 10 min	RT
Blocking I	1 % BSA / TBS (pH 8.2)	10 min	RT
Blocking II	2 % NDS in 1 % BSA / TBS (pH 8.2)	30 min	RT
Primary antibody	0.5 % anti-fibronectin antibody in diluent	Over night	+ 4 °C
Washing	0.025 % Triton / TBS (pH 8.2)	3x 5 min	RT
Secondary antibody	2 % NDS + 0.25 % Alexa Fluor 555 dαr in 1% BSA / TBS (pH 8.2)	2 h	RT
Washing	0.025 % Triton / TBS (pH 8.2)	3x 5 min	RT
Washing	PBS	5 min	RT

A.3. F-actin – Nuclei

Table A.3-1. Anti-F-actin, nuclei staining. RT: room temperature.

Step	Composition	Time	Temperature
Washing	0.025 % Triton / TBS (pH 8.2)	3x 10 min	RT
F-actin staining	0.25 % Ph-488 in 1% BSA/TBS	1 h	RT
Washing	0.025 % Triton / TBS (pH 8.2)	3x 5 min	RT
Washing	AMPUWA	5 min	RT
Nuclei staining	0.07 % DAPI / AMPUWA	15 min	RT
Washing	AMPUWA	3x 10 min	RT